

3D Imaging Methods for Manufacturing, with Emphasis on the Laser Speckle Technique

by

Joseph H. Karlin

S.B., Massachusetts Institute of Technology
(1994)

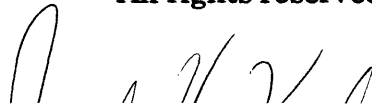
Submitted to the Department of Mechanical Engineering
in Partial Fulfillment of the Requirements for the
Degree of

MASTER OF SCIENCE
in Mechanical Engineering
at the

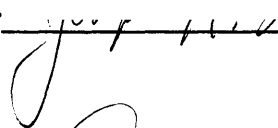
Massachusetts Institute of Technology

June 1995

© 1995 Massachusetts Institute of Technology
All rights reserved




Signature of Author



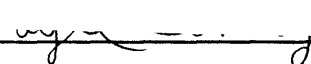
Department of Mechanical Engineering
May 12, 1995

Certified by



David E. Hardt
Professor of Mechanical Engineering
Thesis Supervisor

Certified by



Lyle G. Shirley
MIT Lincoln Laboratory Research Staff
Thesis Supervisor

Accepted by



MASSACHUSETTS INSTITUTE
OF TECHNOLOGY
Ain A. Sonin
Chairman, Department Graduate Committee

AUG 31 1995

LIBRARIES

Carter Eng

3D Imaging Methods for Manufacturing, with Emphasis on the Laser Speckle Technique

by

Joseph H. Karlin

Submitted to the Department of Mechanical Engineering on May 12, 1995 in partial fulfillment of the requirements for the Degree of Master of Science in Mechanical Engineering

Abstract

The purpose of this thesis is to analyze the current state of the three-dimensional imaging industry, exploring in depth the particular technique of laser speckle wavelength decorrelation. Also studied are the effects of different surface finishes, ambient conditions, and data filtering techniques on the accuracy of the laser speckle technique.

A six inch square stamped sheet metal part is used to compare the laser speckle technique to the CMM, an industry standard. The accuracy of the laser speckle device is determined by creating an error map between the sampled speckle data and a mathematical model of the part surface generated from the CMM measurement. The same part is used for eight laser speckle measurements, and the results are compared to determine the effects of each condition on accuracy. In addition, a New Focus tunable external cavity diode laser is examined as a possible replacement for the Titanium Sapphire ring laser currently used in the speckle system.

The results show that the laser speckle wavelength decorrelation technique is accurate in range to 1082 μm (0.0426 in) when measuring a sample sheet metal part of 19 mm (0.75 in) range extent. The theoretical range resolution of the technique is only limited by the tuning range of the laser and the computing power available for data processing. The range resolution is better than 1 μm (0.00004 in) when measuring objects of range extent on the order of 1 mm (0.04 in). In addition, accuracy is degraded by the presence of air turbulence and too much light reflected back to the CCD array. However, proper image processing can extract the image even under non-ideal ambient conditions and surface finishes.

In the short term, the laser speckle technique is not practical for quick and accurate three-dimensional imaging use. Currently, the best technique for quick and accurate surface mapping of sheet metal parts is a triangulation based laser scanning technique currently available from several companies. However, with a few more years of research and development, the laser speckle wavelength decorrelation technique could easily offer the best combination of speed and accuracy in the metrology industry.

Thesis Supervisor: David E. Hardt

Title: Professor of Mechanical Engineering

Dedication

This thesis is dedicated to my grandmother, Sooky Karlin, who is not with us now, but if she was, I know she would be very proud of this work and my other accomplishments in the past nine years.

Acknowledgments

First, I would like to thank my parents and my sister for providing continual love and support to me throughout my life.

Next, I would like to thank Professor David E. Hardt for supervising my research. He helped me a great deal to keep focused in my research and provided an expert point of view when I was trying to decide where to go with this project.

I would like to give special thanks to the MIT Lincoln Laboratory Advanced Concepts Committee, who supported my research.

Also, I would like to thank the members of the Laser Speckle Laboratory of Group 35 of the MIT Lincoln Laboratory. Dr. Lyle Shirley supervised my work at Lincoln and provided much needed guidance and support for my work with Laser Speckle. John Vivilecchia taught me the basics of performing a laser speckle measurement. Emory Ariel was helpful when I was designing a mount for the sheet metal part, and he was a great help with the alignment of the Ti:S laser through the optics. Harold Payson and Michael Mermelstein were a great help in answering various questions about the systems in the Speckle Lab. Bob Hall of the Lincoln Laboratory Library, a master of keywords for journal articles, assisted me during several literature searches. And a special thanks goes to Greg Hallerman, who put up with endless hours of helping me run my Laser Speckle experiments and having discussions about everything from data processing to life in general.

In addition, I would like to thank the crew at the Laboratory for Manufacturing and Productivity. Dan Walczyk was a great help getting me started with my research at MIT and making me feel at home in the Lab in the basement of Building 35. Dan was also very helpful in teaching me how to stamp the sheet metal part which I used for my experiments. Jerry Wentworth was extremely helpful in teaching me how to use the Brown & Sharpe CMM at MIT and putting me in touch with the right people to get the right CMM software.

Finally, I would like to thank Leslie Regan, Joan Kravit, and Susan Melillo of the Graduate Mechanical Engineering Office for helping me with all the paperwork necessary to survive in Graduate School at MIT.

About the Author

Joseph Howard Karlin was born in Philadelphia, Pennsylvania on April 27, 1972. He became involved in research at an early age, entering research projects in the local, state, and national levels of several middle and high school science competition organizations. Joe was recognized for his high school biochemistry research by the Westinghouse Science Talent Search, which named him as a Finalist in 1990.

Joe spent his undergraduate years at MIT, where he graduated with a S.B. Degree in Mechanical Engineering in February, 1994. Then he began work on his S.M. Degree in Mechanical Engineering, also at MIT, and he graduated in June 1995 upon completion of this work. He is scheduled to begin work in Automobile Product Design at the Ford Motor Company in June 1995.

Joe is a brother of the Beta Chapter of Theta Chi Fraternity, and he was elected to membership in Tau Beta Pi, the Engineering Honor Society, and Pi Tau Sigma, the Mechanical Engineering Honor Society. Also, he is a member of the American Society of Mechanical Engineers.

Joe spends his spare time playing the piano and composing music, but none of his songs have yet been recorded. He is also an avid reader of fiction, and he enjoys biking and jogging around the Charles River in Boston.



Table of Contents

1 Introduction	13
1.1 Motivation	13
1.2 Objectives	15
1.3 Outline of Thesis.....	16
2 Mechanical Contact: Coordinate Measuring Machine	18
2.1 Early Manual CMMs.....	18
2.2 Continuous Contact Coordinate Measuring Machine	20
2.3 Touch Trigger Probe Coordinate Measuring Machine	23
2.4 Disadvantages of a CMM.....	26
2.5 Brown & Sharpe MicroVal PFX CMM	27
2.6 Summary.....	30
3 Survey of Three-Dimensional Imaging Techniques	32
3.1 Passive Triangulation	34
3.1.1 Stereo Disparity.....	35
3.2 Active Triangulation.....	37
3.2.1 Point Laser Triangulation.....	37
3.2.2 Scanning Point Laser Triangulation.....	41
3.2.3 Structured Light: Line, Grid.....	45
3.2.4 Moiré Interferometry	47
3.3 Passive Non-Triangulation	51
3.3.1 Range from Focus.....	51
3.3.2 Other Passive Non-Triangulation Techniques.....	54
3.4 Active Non-Triangulation.....	54
3.4.1 Fresnel Diffraction.....	54
3.4.2 Pulse Laser Radar.....	58
3.4.3 Amplitude Modulation Continuous Wavelength (AM CW)	59
3.4.4 Frequency Modulation Continuous Wavelength (FM CW)	61
3.4.5 Holographic Interferometry	63
3.4.6 Laser Speckle Wavelength Decorrelation	67

4 How Laser Speckle Works	68
4.1 What is Laser Speckle?	68
4.2 Finding Range Data from Laser Speckle	68
4.3 System Design.....	72
4.3.1 Laser Speckle System Design	72
4.3.2 Using the New Focus Laser	75
4.4 Image Processing.....	76
4.4.1 Perform a Three-Dimensional Fourier Transform.....	76
4.4.2 Extract Target Image from a Three-Dimensional Array.....	78
4.4.3 Data Filtering	79
5 Experimental Design	81
5.1 The Sheet Metal Part.....	81
5.2 Design of a Repeatable Mounting Fixture.....	82
5.3 CMM Measurements	83
5.4 Laser Speckle Measurements.....	84
5.4.1 Power Distribution Across the Collimated Laser Beam.....	84
5.4.2 Laser Speckle Experimental Trials	84
5.4.3 Determination of Optimal Reference Mirror.....	85
5.5 New Focus Laser Calibration and Characterization.....	87
6 Results and Discussion	89
6.1 Presentation of CMM Data.....	89
6.2 Power Distribution Across the Collimated Laser Beam.....	90
6.3 Presentation of Laser Speckle Data Sets.....	90
6.4 Comparison of CMM Data to Laser Speckle Data.....	112
7 Conclusions and Recommendations	124
7.1 Review of Results: CMM vs. Laser Speckle.....	124
7.2 Laser Speckle: Where is it Headed?	125
7.3 Metrology Solution for Flexible Sheet Metal Forming	126
Bibliography	131
Appendix A: Mounting Fixture and Clamping Piece	135
Appendix B: New Focus Laser Calibration Data	136

List of Figures

Figure 1.1: Flexible Sheet Metal Forming Press at MIT.....	14
Figure 1.2: Face Impression Made By Flexible Sheet Metal Press.....	15
Figure 2.1: Basic Milling Machine / CMM Design.....	19
Figure 2.2: Manual CMM Workpiece Table Axis Controller	20
Figure 2.3: MIT Continuous Contact CMM	21
Figure 2.4: Renishaw Scanning Probe, Adapted From [4].....	23
Figure 2.5: Renishaw Touch Trigger Probe, Adapted From [11].....	24
Figure 2.6: Brown & Sharpe MicroVal PFx CMM.....	28
Figure 3.1: 3D Imaging Terms, Adapted From [17].....	33
Figure 3.2: Triangulation Range Sensing, Adapted From [18]	35
Figure 3.3: Point Triangulation Range Sensor, Adapted From [19]	38
Figure 3.4: Camera Centered Point Triangulation.....	42
Figure 3.5: Autosynchronized Scanning, Adapted From [37].....	43
Figure 3.6: Line Scanning, Adapted From [40].....	46
Figure 3.7: Moiré Fringe Pattern	47
Figure 3.8: Projection Moiré Configuration, Adapted From [17]	49
Figure 3.9: Thin Lens Relationships, Adapted From [17].....	52
Figure 3.10: Fresnel Diffraction System, Adapted From [55].....	57
Figure 3.11: AM CW Radar Principles, Adapted From [17].....	60
Figure 3.12: FM CW Linear Ramp Principles, Adapted From [17].....	62
Figure 3.13: Example of a Holographic Setup, Adapted From [68].....	64
Figure 4.1: Speckle Pattern from Triconic, Adapted From [2]	69
Figure 4.2: Step Target Speckle Intensity Variation, Adapted From [2].....	70
Figure 4.3: Laser Speckle System Diagram, Adapted From [2].....	73
Figure 4.4: Laser Speckle System Setup	73
Figure 4.5: The New Focus External Cavity Tunable Diode Laser.....	76
Figure 4.6: Three-Dimensional Laser Speckle Array.....	78
Figure 4.7: Extracting an Image.....	79
Figure 5.1: The Sheet Metal Part Used for This Work.....	82
Figure 5.2: The Die Which Made the Sheet Metal Part	82

Figure 5.3: Mounting Setup for the Sheet Metal Part.....	83
Figure 5.4: Coated Sheet Metal Part with Reference Mirror	86
Figure 5.5: Two Dimensional FFT of Coated Part, $R = 0.25 \text{ m}$	87
Figure 5.6: Burleigh Wavemeter.....	88
Figure 6.1: CMM Measurement of Sheet Metal Part.....	89
Figure 6.2: Power Distribution of Ti:sapphire Beam	90
Figure 6.3: Diffuse White Paint, 128 Frames	93
Figure 6.4: Diffuse White Paint, 256 Frames	95
Figure 6.5: Light Coat of Diffuse White Paint, 128 Frames	97
Figure 6.6: No Coating, 128 Frames.....	101
Figure 6.7: Coated with Machining Oil, 128 Frames	103
Figure 6.8: Half Coated with Diffuse White Paint, 128 Frames	106
Figure 6.9: Diffuse White Paint, Oscillating Fan, 128 Frames.....	109
Figure 6.10: Diffuse White Paint, Air Circulation On, 128 Frames.....	112
Figure 6.11: Comparison: Y-Z Slice Through Part	117
Figure 6.12: Comparison: X-Z Slice Through Part	121
Figure 6.13: Whole Target Error Mapping.....	123

1

Introduction

1.1 Motivation

Rapid prototyping can be very useful to product designers of many types of products. Many times, marketing or artistic design people will create a wood or plastic mock-up of a new product. The product designer is handed this conceptual model and told to create something that looks like it. How much easier her job would be if a real time high accuracy three-dimensional imaging system were available. One could scan the object and have a mathematical model of it inside a CAD system in seconds. It would then be a much more simple task to create machining code for the part and to create prototypes or dyes for manufacturing the part.

Quality control is very important in manufacturing systems. Keeping manufactured parts in tolerance is vital to making a successful product. Currently, one can check critical dimensions of a part in real time, or one can take a few minutes to get an accurate three-dimensional map of the part. A real time high accuracy three-dimensional imaging system would make possible much more careful tolerancing of parts in a short period of time, which would be very valuable in a process such as manufacturing of car door panels.

Advanced manufacturing systems would also greatly benefit from a real time high accuracy three-dimensional imaging system. A flexible sheet metal

forming system developed at MIT (Hardt et. al. [1], see Figure 1.1) uses a closed loop system to converge on an accurate part after several iterations of measuring the part, calculating an error map, making a new die, and forming a new part. In this way, an accurate part can be made in a few iterations without fully modeling the springback in the system. A real time high accuracy three-dimensional imaging system would make a closed loop system of this type very useful in sheet metal manufacturing applications.

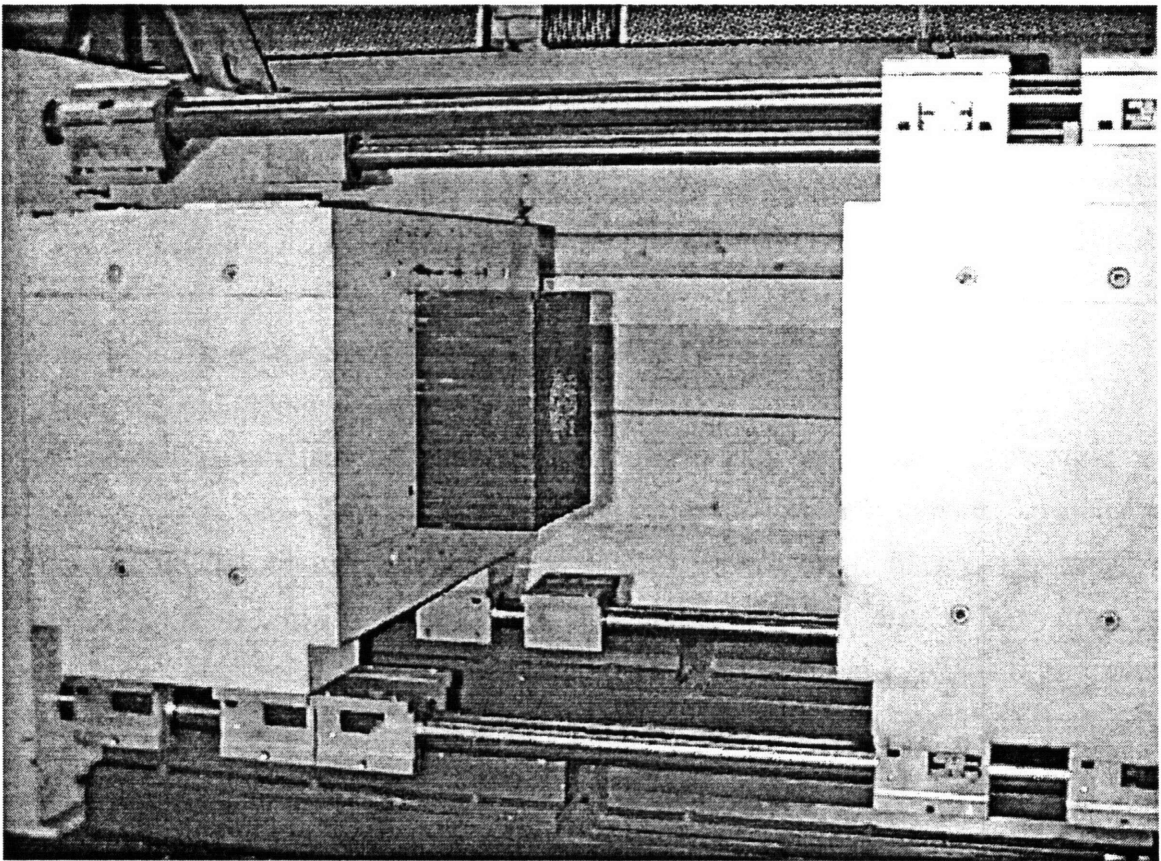


Figure 1.1: Flexible Sheet Metal Forming Press at MIT

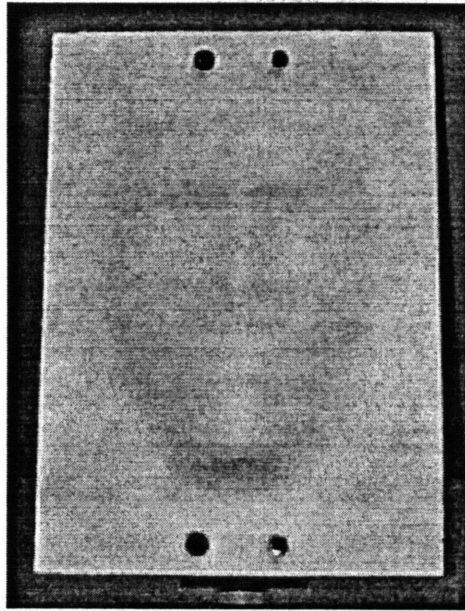


Figure 1.2: Face Impression Made By Flexible Sheet Metal Press

Three-dimensional imaging systems have come a long way in the last several years. Improvements in electronics and computing power have made today's systems faster and more portable than those available just a few years ago. However, there still remains a need for more quick and accurate systems than those we currently have. The sheet metal industry, for example, could sorely use a real time, high density, sub-micron accuracy imaging system. Laser Speckle could be just this system in a few years.

1.2 Objectives

The purpose of this thesis is to explore the current techniques available for three-dimensional imaging, investigating in detail the laser speckle wavelength decorrelation technique being researched at MIT Lincoln Laboratory (Shirley et. al. [2]).

The first principal objective is a comprehensive literature review of the current state of the three-dimensional imaging market. There are several different underlying technologies which have been used to measure objects, and each one has different strengths and weaknesses to be explored. Also, there are many companies which currently market three-dimensional imaging

products which use these technologies. By exploring the capabilities of these technologies and products, areas of research need can be determined. The literature review will concentrate on techniques which can be applied to the sheet metal market, in particular concerning flexible sheet metal forming applications, since this is the scope of my research.

The second principal objective is an investigation of the laser speckle wavelength decorrelation technique. This is a promising new technique for three-dimensional imaging which could potentially fill a gap in the range of capabilities provided by those techniques already in commercial use. In order to compare the technique to others, it is necessary to obtain specifications through theoretical and experimental analysis. To do this, a stamped steel sheet metal part is measured on both the laser speckle system and a coordinate measuring machine (CMM), which is used as a standard. Several different variations of ambient conditions and surface finishes are used to determine the strengths and weaknesses of the speckle technique.

Once these objectives are met, possible niches for laser speckle can be explored, as well as possible three-dimensional imaging solutions for rapid prototyping and advanced manufacturing systems.

1.3 Outline of Thesis

The thesis is organized as follows. Chapters 2, 3, and 4 present the background information necessary to perform the laser speckle experiments. Chapter 2 presents information on coordinate measuring machines, the current three-dimensional metrology industry standard, which is used as the metric to which to compare the speckle technique. This includes detailed information concerning how a CMM works and the advantages and disadvantages of the system used. Chapter 3 contains a detailed comprehensive literature review of current methods of three-dimensional imaging, breaking the information down into sections based on the fundamental technologies on which the techniques are based. Chapter 4 presents information on the laser speckle wavelength decorrelation system being researched at MIT Lincoln Laboratory. This chapter includes

information on the optics theory behind the speckle technique, as well as a presentation of the system design. The equipment used in the system is discussed, and the software used for data collection is also presented. Furthermore, information regarding the data processing and image filtering techniques used to obtain images is discussed.

Chapters 5, 6, and 7 present the experiments, results, and conclusions concerning my research. Chapter 5 contains a detailed discussion concerning the sheet metal part used for the experiment and the various conditions under which it was measured on the speckle system and the CMM. Also presented is information about the New Focus laser which may be used in a prototype laser speckle system. In addition, the mathematical modeling and error mapping techniques used for determining the accuracy of the laser speckle system, using the CMM as a standard, are presented. Chapter 6 presents the data obtained from the CMM and laser speckle experiments. Also, the accuracy of the laser speckle method in various ambient conditions and with various surface finishes is determined. Chapter 7 presents conclusions which can be drawn from this research. The laser speckle wavelength decorrelation technique is evaluated along with the other three-dimensional imaging techniques currently available for measuring sheet metal. In addition, a market niche for laser speckle is proposed, and future research areas are discussed.

2

Mechanical Contact: Coordinate Measuring Machine

2.1 Early Manual CMMs

The coordinate measuring machine, or CMM, is currently the most popular three-dimensional measurement device. It is widely used in many industries and is generally known as the metrology industry standard.

A CMM is any type of device which has a probe that can move in three or more degrees of freedom relative to a part and also provides position feedback which allows the probe tip to be located in three-dimensional space. The earliest CMMs were similar to manual milling machines. In typical manual milling machines, there is a workpiece table which can translate in two dimensions (x,y), and there is a spindle which accommodates the cutting tool which can translate in one dimension (z). This basic milling machine / CMM design is illustrated below in Figure 2.1

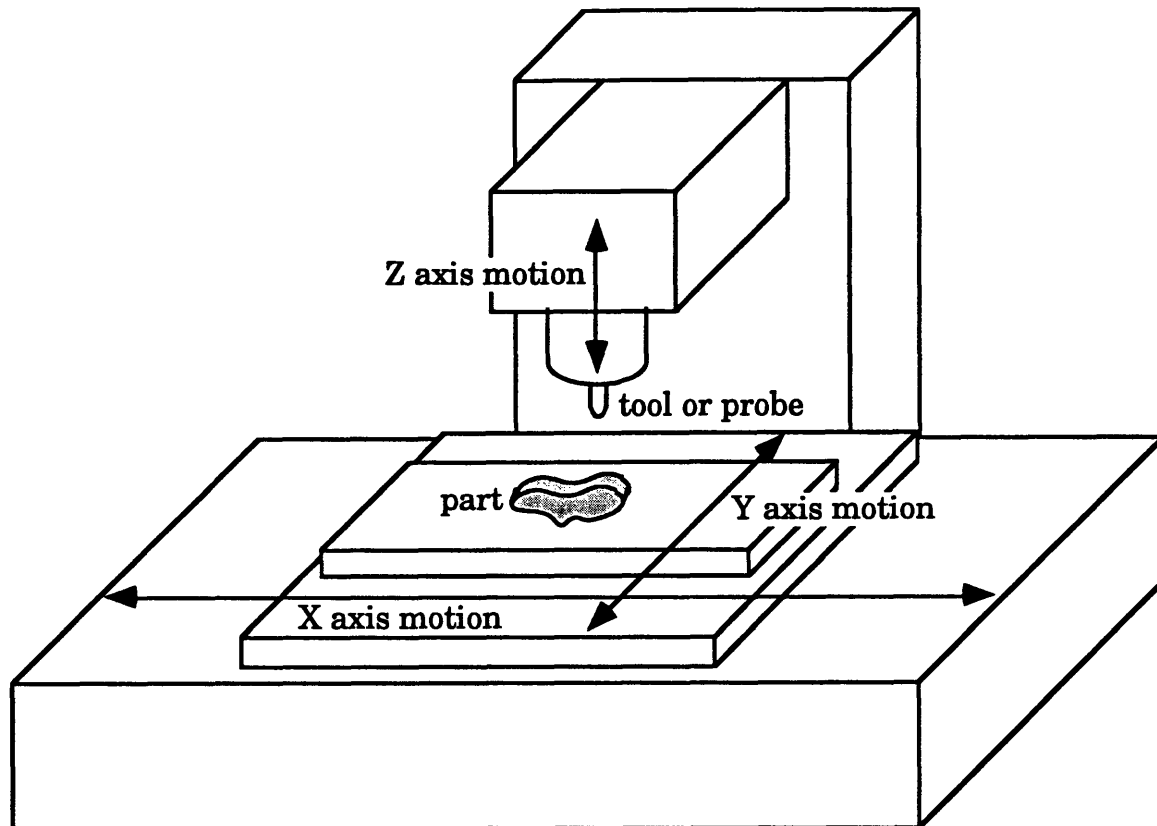


Figure 2.1: Basic Milling Machine / CMM Design

The machinist manually moves the workpiece table via two wheels which translate rotary motion into horizontal motion of the table. The wheels are attached to a ruled cylinder, usually calibrated to 0.001", which is lined up with a stationary cylinder with an arrow or other mark to read the current position. One can obtain relative position information by reading the ruled scale. This axis controller is shown in Figure 2.2 below. The spindle is usually translated either by a lever or a wheel, also manually controlled and ruled in some manner to provide position feedback. To use this machine as a CMM, one simply needs to retrofit a probe to the cutting tool mounting hole. The part is placed on the workpiece table, and the user touches the probe to the part, reading the position of the three axes each time. This similarity in the three-dimensional position feedback needs of CMMs and milling machines allow many milling machines to also serve as CMMs in shops that do not have the money or space for both machines.

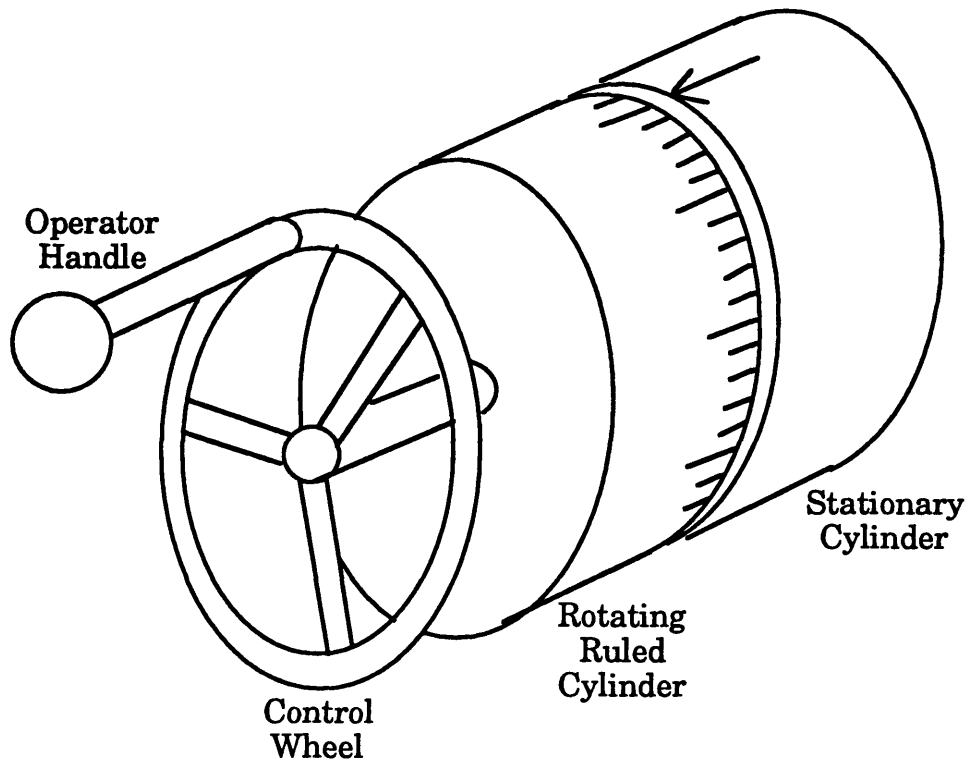


Figure 2.2: Manual CMM Workpiece Table Axis Controller

2.2 Continuous Contact Coordinate Measuring Machine

With the advent of the computer, CMMs became a much more powerful tool. Instead of reading a ruling or digital readout and recording data points by hand, the user could now record three-dimensional position data electronically. This necessitated the use of linear or rotary analog or digital position sensors to determine the position of the probe. The use of a computer and sensors also freed the CMM manufacturers from a simple Cartesian axis design. Any three or more degree of freedom system of linkages could be used to position the probe, and a simple computer program could be used to translate the information provided by the sensors into Cartesian coordinate data.

Although the technology was available to set the probe in continuous motion along one axis prior to the invention of the computer, it did not make sense to do this if one needed to record data manually. Now, it was possible to

record a steady stream of three-dimensional data points from the sensors while moving the probe along one axis. This allowed the invention of the continuous contact CMM, which could take data points very quickly while contact was maintained between the probe and the part.

Maintaining continuous contact between the probe and the part is crucial in this type of CMM. It is also crucial, however, to automate the motion of the probe up and down (z axis) while scanning along an axis (x or y axis) such that the probe or part is not damaged by excessive force between the two. One way of doing this is to design a probe which can sense the forces between itself and the part and react with appropriate vertical motion. This was done at MIT by Ousterhout [3], and it is pictured below in Figure 2.3.

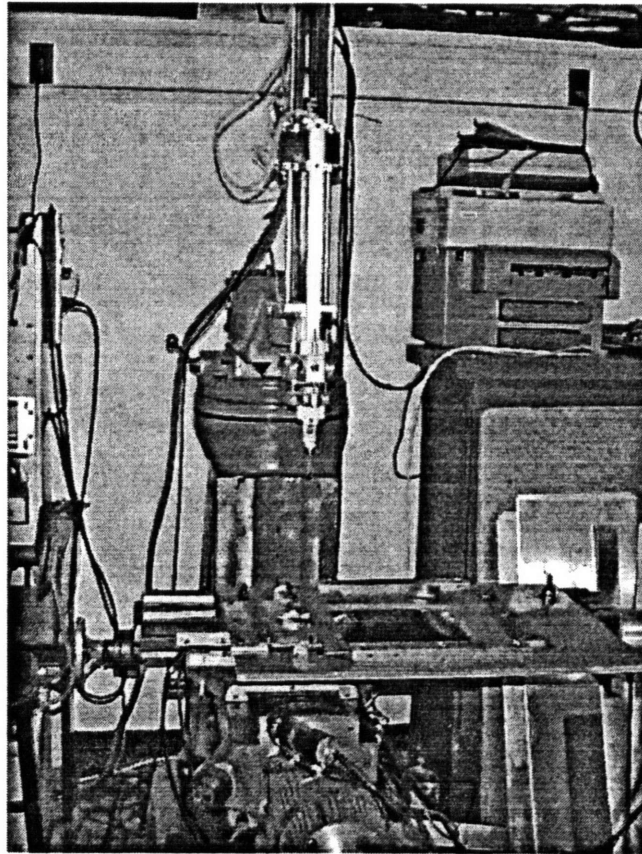


Figure 2.3: MIT Continuous Contact CMM

The probe design incorporates two strain gauges to determine the deflection of the probe in the x and y axes (along the workpiece table) and an

LVDT to sense deflection in the z axis (up and down). The probe is free to translate in the z axis a few centimeters before the z axis is moved by motor control. As the CMM moves along one axis, the z axis is moved up and down according to an algorithm based on the input provided by the strain gauges and LVDT, with the goal of remaining in contact with the part. During the scan, a computer takes a steady stream of x,y,z data points according to a user set time interval. In this early design, however, the probe leaves large (1 mm) grooves in the part as it measures.

More current continuous contact machines have largely solved the problem of leaving deep grooves in the surface of the part. A recent probe design by Renishaw [4] (see Figure 2.4 below) incorporates three motor controlled degrees of freedom inside the probe which allows the angle of contact between the stylus tip and the part surface to remain normal throughout the scan. In a manner similar to the MIT scanning CMM design, the Renishaw probe incorporates a strain gauge system for sensing forces transverse to the probe's local z axis. In addition to a single linear transducer to determine motion of the probe tip along the local z axis, the Renishaw design also uses two angular transducers to determine the angular displacement of the probe tip in two degrees of freedom relative to the CMM's z axis. A computer takes the sensor feedback and moves the three local probe motors and the CMM's z axis motor to keep the probe in continuous normal contact with the part surface. The use of modern sensors and electronics in the probe allows the forces between the probe and the part to be kept at a near constant level which can be adjusted by the user to prevent significant damage to a part.

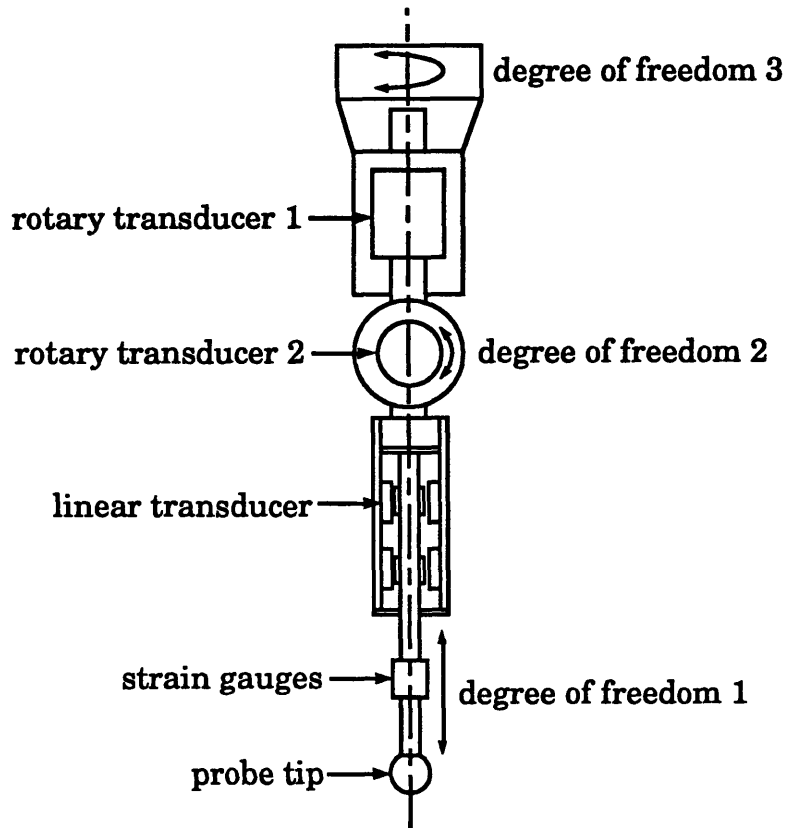


Figure 2.4: Renishaw Scanning Probe, Adapted From [4]

The continuous contact scanning method is also used in stylus instruments, frequently called profilometers, which are used for measuring surface roughness or geometries with extremely small range extents (less than $1\mu\text{m}$). Since this kind of range extent is not typical of sheet metal design applications, I will not go into depth concerning the details of this type of product. However, if you need more information, several papers [5-10] have been written detailing this application.

2.3 Touch Trigger Probe Coordinate Measuring Machine

The next invention to revolutionize the CMM was the touch trigger probe. Instead of having a computer read the axis position sensors at a constant rate while the probe maintains contact with the part, the computer is signaled by the probe to take a position reading when it touches the part surface at discrete points. This allows for sampling of parts at precise three-dimensional

points, unrestricted by the need to remain constrained to two axis motion while taking data points. With a touch trigger probe, one can easily check for the location or size of holes or other features, manually or via computer commands. Also, there is less danger of scraping grooves in a surface because the axial stiffness of the probe can be very little yet still allow for very accurate measurements. The triggering can be done in a number of ways, but the basic probe design is similar. One example of a touch trigger probe by Renishaw [11] is shown below in Figure 2.5.

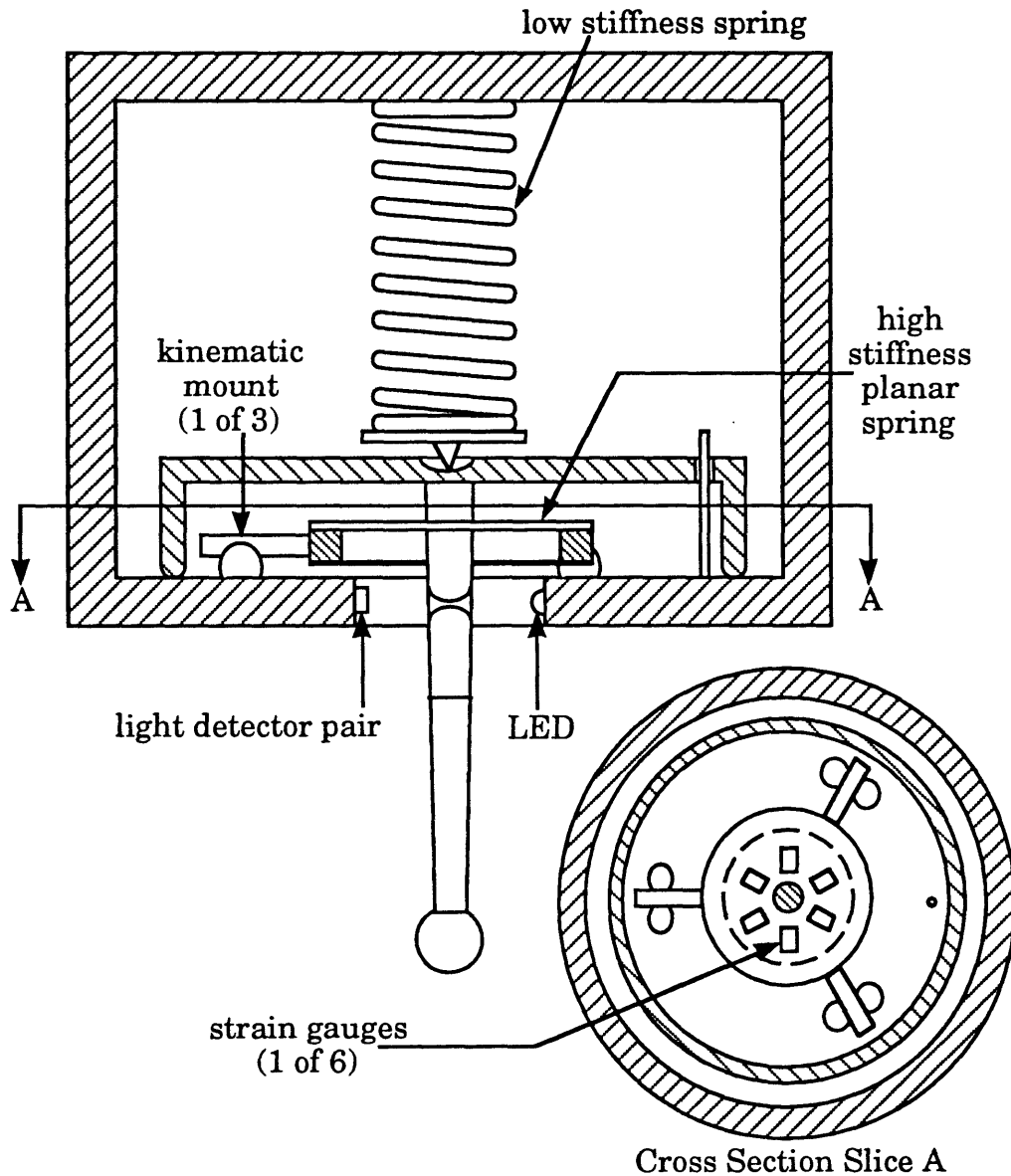


Figure 2.5: Renishaw Touch Trigger Probe, Adapted From [11]

The Renishaw touch trigger probe shown above incorporates two springs to allow motion of the probe axially and horizontally. When the probe contacts the part, axial motion of the probe results. This motion blocks some of the beam going from the LED to the light detector pair. This sudden change in voltage between the two detectors causes a trigger signal to be sent, indicating to the computer that the part has been contacted. At this instant, all sensor data is read, including both the linear encoders or other sensors for determining global x,y,z position and the strain gauges or other sensors for measuring the local deflection of the probe. Part contact triggering can also be done several other ways. Another common triggering scheme is that of mounting strain gauges in a position such that any sudden motion of the probe is detected. Also, one could use piezoelectric elements which can detect either strain or a shock wave generated by the contact between the part and the probe. In addition, a triggering circuit could be set up which is broken when the probe is unseated from its kinematic rest position, signaling contact with the part. One of the most creative methods of detecting contact was done by Renishaw [12], where the workpiece table is vibrated at high frequency (isolated from the probe, of course) and the contact is sensed by a piezoelectric crystal when the vibrations travel through the probe. This scheme prevents the probe from triggering from shock waves created by something other than the probe contact in a noisy manufacturing environment.

In addition to the triggering mechanism, it is necessary to correct for the finite probe tip radius. The probe tip will introduce an error at each data point of the magnitude of the radius of ball at the end of the probe. To obtain the direction of the error, one must determine the angle of contact between the probe and the part surface, from which the actual position of the part surface can be inferred. This can most easily be done via an arrangement of strain gauges placed to detect deflection of the probe in its local x,y plane.

After the probe is retracted from the part surface, the probe is forced by springs to be kinematically seated at its original rest position, thus allowing for very repeatable measurements. In the probe of Figure 2.5, Renishaw chose to use a stiffer planar spring to allow probe motion in the local x,y plane and a less

stiff spring to allow axial motion. The reason for this arrangement was that in many touch trigger probes, there is frequently hysteresis in the rest position of the stylus after the probe is retracted, when the spring forces are unable to completely overcome the frictional forces to return the stylus precisely to its rest position. The very light axial spring force reduces the friction inside the probe, while the strong planar spring forces the probe back to its precise kinematic rest position. This design helps make the probe more repeatable.

2.4 Disadvantages of a CMM

Although coordinate measuring machines have come a long way from their earliest versions, there are still some significant disadvantages to using them in certain applications. The first of these is the speed of measurement. Certain CMM systems are faster than others, but measuring large parts with a dense sampling grid gets very time consuming because the CMM has to physically touch the entire part. For example, if you want to measure a part that measures 100 mm by 100 mm, and you want to sample the part in a 1 mm grid, each point taking 1 second, it will take you 10,000 seconds, or almost 3 hours to measure the part.

Also, there is the problem of elastic and plastic deformation of the surface of a part. Modern CMM's have solved the problem of scraping and dimpling hard surfaces, but softer surfaces can still be a problem. If you want to measure really sensitive surfaces such as foil, you can use a really sensitive probe to avoid plastic deformation, but you are going to have to compromise on time of measurement. The approach speed has to be very slow to be gentle on a sensitive surface. In addition, doing continuous contact scanning can be problematic when measuring surfaces with a high coefficient of friction against the probe tip, such as rubber, because of stick-slip behavior of the probe tip. However, even if you try to measure rubber or another easily elastically deformable material with a touch trigger probe, there can still be problems because of the elastic deformation which can occur, which can lead to faulty measurements.

Another limitation is that the size of the machine must be larger than the size of the part. If you want to measure a car door, you need a CMM that can move its probe to any part on the door. Since the cost of the machine exponentially scales with the size of the machine, measuring large parts can be both time consuming and expensive. Also, the fact that you have to touch each point on the part surface causes problems when there are recessed sections of the part with steep walls. You need your probe to be as long as the bottom of these sections in order to reach the part.

Finally, CMM probes have a finite diameter ball on the tip of the probe. This means that one can only measure surface features which have a spatial frequency larger than the diameter of the ball. Therefore, small holes and slots may not be picked up unless you use a small enough probe tip.

2.5 Brown & Sharpe MicroVal PFx CMM

Since the coordinate measuring machine is widely used and is currently the industry standard three-dimensional metrology device, it was a natural choice to use as the metric against which to measure the performance, accuracy, and other specifications of the laser speckle wavelength decorrelation system. For this research, a Brown & Sharpe MicroVal PFx CMM was used. The primary reason for the selection of this manufacturer's CMM was that MIT happens to have one, and that it was available for my use. Brown & Sharpe has loaned the MIT Laboratory for Manufacturing and Productivity the MicroVal PFx for use in student research. The MicroVal PFx is pictured below in Figure 2.6.

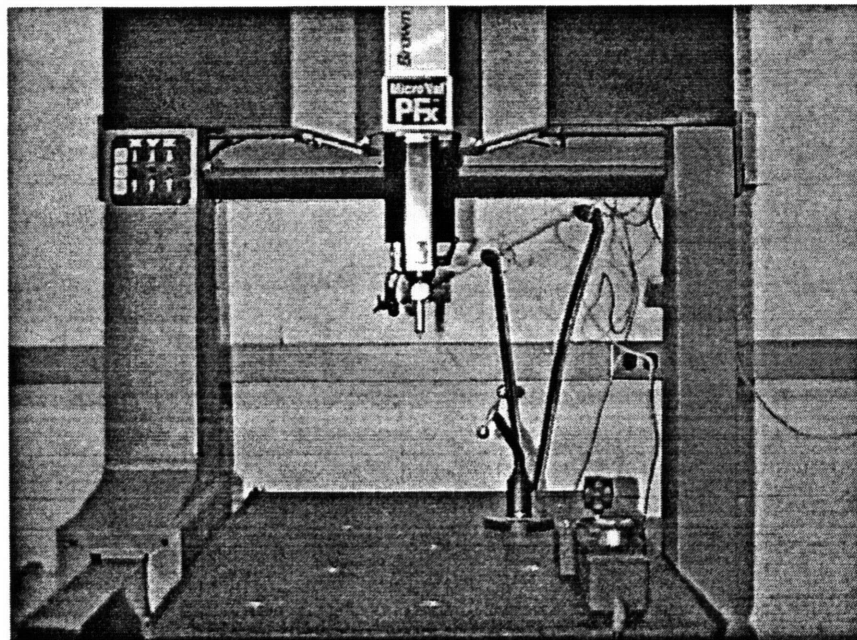
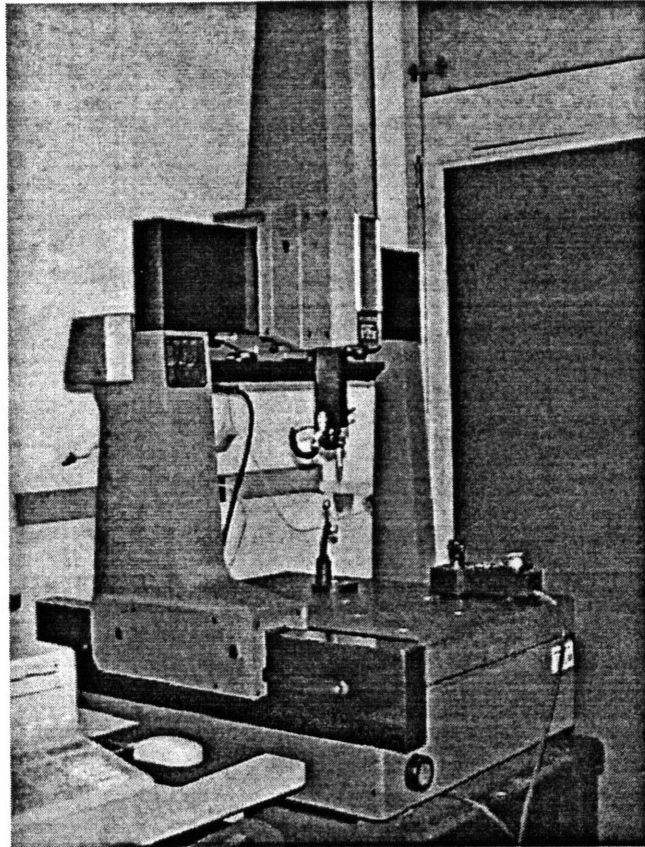


Figure 2.6: Brown & Sharpe MicroVal PFx CMM

The MicroVal PFx system includes an IBM compatible 486 PC. Brown & Sharpe provided a computer program, Micromeasure IV, to be the interface between the user and the CMM. The program had a somewhat convenient icon based graphical user interface, but the system took a significant amount of learning time before I was proficient at measuring a part. One can either use the computer to control the motion of the CMM, or one can manually control it via the attached joystick controller or by holding onto the grip just above the probe assembly and moving it by hand.

The MicroVal PFx uses air bearings to allow for quick, low friction motion. It moves with three degrees of freedom, able to translate in the x , y , and z axes. The CMM uses a bridge type design to prevent errors introduced from bending in a cantilever arm. A direct drive design is used for actuation of the stages, where the motor is directly coupled to the drive shaft, translating rotary motion to linear motion by six roller bearings.

Position information for the x , y , and z axes are read via linear incremental optical encoders. The encoder consists of two glass scales, an LED source, and a photodiode receiver. The glass scales are coated with lines of a highly reflective material, with non-reflective gaps between them. One glass scale runs the full length of the bearing, and it is mounted to the bearing. The second glass scale, called the reticle, is much smaller, and is slid along the bearing next to the first scale. As the reticle is moved over the stationary scale, light from an LED is aimed through the reticle, off of the scale, back through the reticle, and into a photodiode. During the linear motion, the light reaches the photodiode in a square wave manner. Position information (the number of counts), is sent to the computer. The reticle has an additional grating which is physically offset $1/4$ of a division (90°) from the first grating. This grating has its own LED and photodiode, and this signal either precedes or follows the other signal depending upon the direction of travel [13]. This type of encoder is called a quadrature encoder [14].

Brown & Sharpe gives the following specifications for their MicroVal PFx CMM:

- volumetric accuracy: $10 \mu\text{m}$

• linear accuracy	5 μm
• resolution	1 μm
• repeatability	3 μm
• range XYZ	457 x 508 x 406 mm
• weight (complete system)	727 kg
• cost	\$100,000.00

2.6 Summary

Today, CMMs are available in all shapes and sizes. A host of companies manufacture them, for prices ranging from a few thousand dollars for a small manual CMM to several hundred thousand dollars for large computer controlled ones. They are in use in every manufacturing sector from designing small consumer products to designing automobiles and airplanes. As one can guess, the accuracy and resolution of these devices vary according to the scale, axis motion schemes, sensors chosen, and probe used. Some manufacturers of CMMs include the following:

- Brown & Sharpe, North Kingstown, RI
- Brunson Instrument Company, Kansas City, MO
- Carl Zeiss
- DEA, Livonia, MI
- Forward Poli, Chesterfield, MI
- Helmel, Niagara Falls, NY
- International Metrology Systems, Ontario, Canada
- LK Inc., Brighton, MI
- L.S. Starrett, Mount Airy, NC
- MicroVu, Windsor, CA
- Mitutoyo, Tokyo, Japan
- Renishaw, Gloucestershire, UK
- Romer, Inc., Carlsbad, CA
- Sheffield

- Simco Industries, Inc., Roseville, MI
- TSK America, Farmington Hills, MI

The accuracy of a CMM is fundamentally limited by a few things. The first of these is the sensors used to determine the position of the probe tip in three-dimensional space. Most CMMs use linear encoders to determine the position of the global x , y , and z axes, and most CMMs use Renishaw Probes, which use strain gauges to determine the relative orientation of the surface when the probe contacts it. Also, the accuracy of a CMM is limited by the straightness of the rails and the squareness of the axes to each other. The larger the CMM, the longer the axis rails, and therefore the more error the rail straightness and squareness can introduce into the system. Naturally, cheaper machines use cheaper sensors and axis rail materials, so accuracy varies from manufacturer to manufacturer. However, a linear accuracy, resolution, and repeatability of $1\mu\text{m}$ is not uncommon among the above listed CMM manufacturers. As technology allows manufacturers to create longer, straighter axis rails, more finely grated optical encoders, and more accurate strain gauges, CMMs can become increasingly more accurate, as long as consumers are willing to pay the price for it. However, as CMMs incorporate these new technologies, things which are neglected now such as air currents and workpiece table vibration may become much more important to the accuracy of the machine.

3

Survey of Three-Dimensional Imaging Techniques

Although there are scores of three-dimensional imaging products currently commercially available, they rely on the same basic set of fundamental technology categories. The first way to differentiate between the technologies is to determine whether or not there is mechanical contact between the measurement device and the part to be measured. The coordinate measuring machine, the most popular mechanical contact three-dimensional measuring device, was discussed in detail in the previous chapter. Of non-contact devices, one can make a distinction between passive and active methods of measuring. A passive method is one which does not introduce special lighting onto the part in order to measure it, while an active method may project a pattern of light onto the part or probe the part with beams or planes of laser light. Another basic difference between non-contact devices is whether or not geometric triangulation is used to obtain range information.

In the following sections, each of the fundamental non-contact three-dimensional imaging technologies will be discussed in detail. They will be

presented in four sections, classified according to whether they are active or passive and whether or not they use triangulation to obtain range information. Several [15-25] have published three-dimensional imaging technique surveys from different perspectives. In this survey, I concentrate on uses which can be applied to sheet metal manufacturing.

Some of the terms which are used to describe the capabilities of three-dimensional imaging techniques are shown below in Figure 3.1. The standoff distance of a sensor is the minimum distance from the sensor at which objects can be imaged to within the cited accuracy. The depth of field is the maximum possible range extent of a target which can be measured accurately. The field of view is the maximum possible cross range extent of a target, perpendicular to the ranging axis of the sensor, which can be measured accurately. The range resolution of a sensor is the minimum discernible range difference between parts of a target.

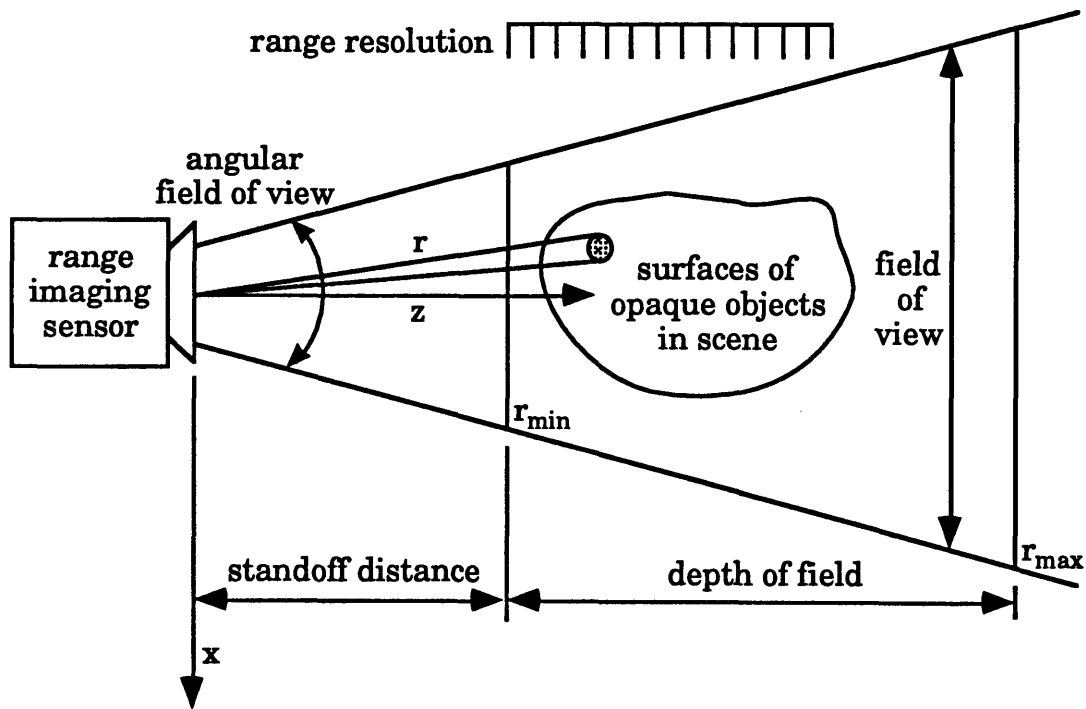


Figure 3.1: 3D Imaging Terms, Adapted From [17]

3.1 Passive Triangulation

Triangulation is based on elementary geometry, as shown below in Figure 3.2. The law of sines states that if the length B (the baseline) of one side and two interior angles $\angle AB$ and $\angle BC$ of the triangle ABC are known, then the lengths A and C and the remaining angle $\angle AC$ must satisfy the following relation:

$$\frac{\sin(\angle AB)}{C} = \frac{\sin(\angle BC)}{A} = \frac{\sin(\angle CA)}{B} \quad (3.1)$$

Therefore, if one knows the length of the baseline of a triangle and the angles at the baseline vertices, then the range from either of the two vertices to the third one can be easily computed as the corresponding triangle side via the law of sines (Equation 3.1). Thus, triangulation-based imaging systems measure angles and baseline distances as accurately as possible in order to do accurate ranging. Also, all triangulation systems can have a problem if occlusion prevents measurement of the second angle because a point is only visible along side A or C in the triangle ABC .

As shown below in Figure 3.2, the epipolar plane is the plane in which the triangle lies. Passive triangulation methods rely on the basic geometric relationship of Equation 3.1, making use of ambient light conditions.

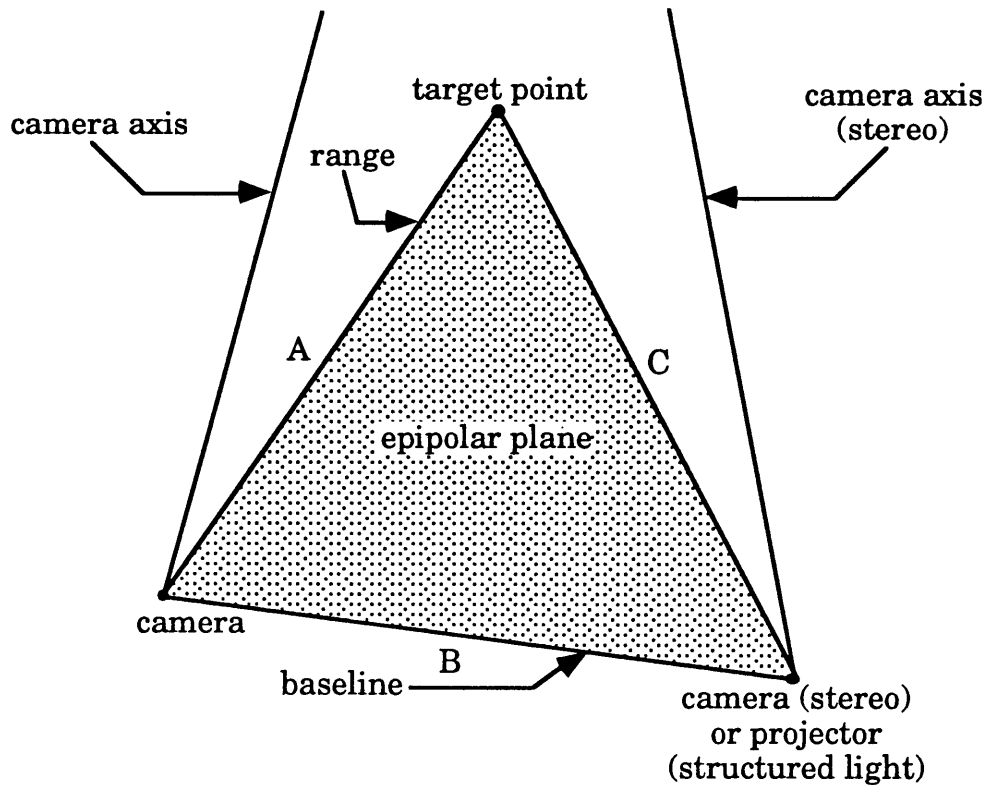


Figure 3.2: Triangulation Range Sensing, Adapted From [18]

3.1.1 Stereo Disparity

Stereo Disparity is the most well known non-contact three-dimensional imaging technique, since it is used in human vision from up to 200 feet. Stereo disparity techniques use an image sensor (usually a CCD array, a two dimensional array of detectors which accumulate a photon-induced charge when light falls on them) at each of two triangle vertices, as shown in Figure 3.2 above. A stereo pair of images can be obtained either from two separate cameras or from a single camera which is moved from one vertex to the other.

The range from either camera to the target can be easily calculated as long as one can match up each point on the target in one camera with a point on the target in the other. This is called the correspondence or registration problem, and it has plagued researchers in stereo disparity for many years. If correspondence is to be determined from the image data, there must be sufficient visual information at the matching points to establish a unique pairing relationship.

There are two main problems concerning correspondence. The first arises when parts of an image are so uniform in intensity and color that matching is made impossible, and the second arises when the image of part of the scene appears in only one view of the stereo pair because of occlusion effects or because of the limited field of view captured by the cameras. For simple objects with sharp edges, stereo vision can work well. However, the more complicated objects are, the more complex stereo matching algorithms must be in order to match features in one camera view to features in the other. Also, as the complexity of the matching algorithm increases, so does the time it takes to obtain three-dimensional data.

There have been many attempts to solve this problem, such as the Marr-Poggio-Grimson algorithm [26] and several others [24, 27-28]. However, problems with occlusion, shadowing, optical illusions, out-of-focus smearing, and specular reflections abound. One way to simplify the problem is to project structured light onto the target, but this is an active triangulation technique, and it will be discussed in the appropriate section.

The accuracy of a stereo disparity system is heavily dependent on the ability of the correspondence algorithm used to match features in the two cameras. This is the biggest disadvantage with the use of stereo disparity systems. As computer systems get more powerful and algorithms become more efficient, the accuracy of such a system can improve.

If the correspondence problem is solved for relatively simple target shapes, then the accuracy of the system would be determined by the resolution of the cameras, which is related to the number of pixels in the CCD array used. If one uses a 512 by 512 pixel CCD camera, then the cross range resolution is limited to the horizontal or vertical field of view divided by 512. The range resolution is dependent on the distance between the cameras. An increased camera separation results in increased range resolution for a given size CCD array, but too much separation may result in occlusion, which will cause the range information in the section of the target not visible in both cameras to be lost. This tradeoff must be optimized for each measurement taken.

Because of the disadvantages of the stereo disparity method discussed above, the technique is not widely used for range finding in manufacturing. It is mostly used in areas where range accuracy on the level of microns is not necessary, such as robot guidance and bin picking.

3.2 Active Triangulation

3.2.1 Point Laser Triangulation

Point laser triangulation is the most widely used non-contact three-dimensional measurement technique in the manufacturing industry. This technique involves the projection of a laser beam onto a target, and a detector (usually a linear CCD array) is used to image the point. The range to a point on the target is then calculated using a simple geometric equation.

A simple design for a point laser triangulation range sensor is shown below in Figure 3.3. This design incorporates a light source and a detector, separated by a fixed baseline distance, which must be accurately calibrated. The light source is aligned along the z axis with the center of its lens positioned at $(0,0,0)$. At a baseline distance b from the light source along the x axis is the detector lens, which is tilted at a fixed angle relative to the x axis baseline. A spot of light from the laser beam is projected onto the detector at the pixel u , which is measured in pixels from the u axis intersection with the w axis, which goes through the center of the detector lens parallel to the z axis. Thus, one can calculate that $uz = bf_z$ via similar triangles where f_z is the z component of the focal length of the detector lens, measured in pixels. The range value z of the target point can be calculated from the measured value u as shown in the following relation:

$$z = \frac{bf_z}{u} \quad (3.2)$$

In this technique, a change in the range of the part, Δz , is reflected in a shift in the beam image on the CCD array by Δu pixels.

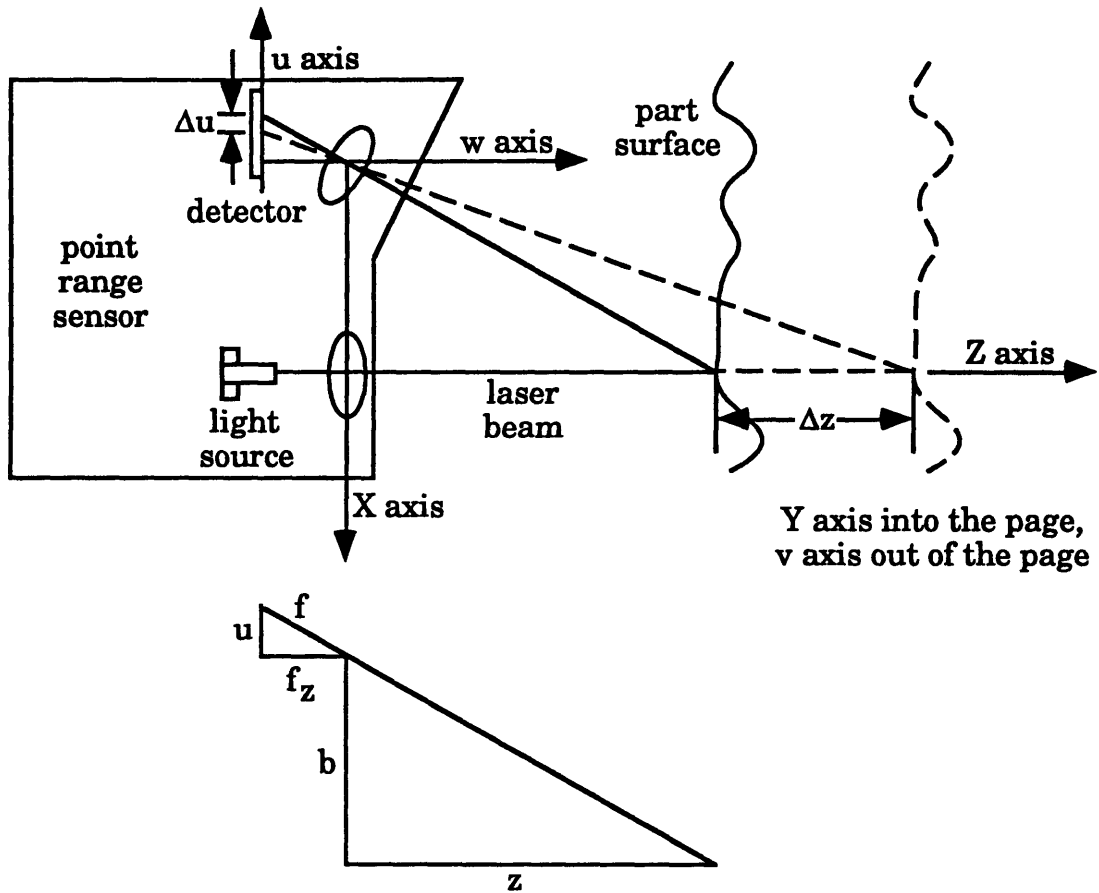


Figure 3.3: Point Triangulation Range Sensor, Adapted From [19]

By itself, this technique is a single dimensional one, and it is used as such in many industries, especially by automobile companies for measuring tolerances at single points. However, a point triangulation sensor becomes a three-dimensional device when it is retrofitted to a CMM in place of a scanning contact probe or touch trigger probe; it uses the CMM to scan it in a similar manner to a contact probe. This is one of the principal reasons for its current popularity. A point triangulation sensor allows for much greater scanning speeds than mechanical contact techniques, but it can be used with a CMM for a fraction of the cost of purchasing a whole new system.

The accuracy of a point triangulation sensor can be no better than the equipment it is used with. If it is used as a CMM attachment, the error of the CMM is added to the error of the sensor to obtain the error of the measurements taken with the system. Concerning the sensor itself, it is a

common belief that a large baseline distance separating the laser and the detector is necessary to allow for accurate determination of range. However, for any fixed baseline distance and detector lens focal length, the range resolution of a triangulation system of this type is limited only by the ability of the system to accurately measure the horizontal position of the point where the laser hits the CCD array, and the range accuracy is only limited by the accuracy of the knowledge of the baseline length, the focal length of the detector lens, and the ability to properly focus the image on the detector. Therefore, the components should be mounted sturdily and kinematically, and the chassis of the device should be made of a material with low thermal expansion properties.

A detector with the smallest pixel size will allow for the greatest resolution, which is directly related to the resolution of range measurement. Also, a greater baseline distance will allow for more range resolution for a particular detector array. The reason for the influence of baseline distance in range resolution is that a greater angle between the detector-lens axis and the beam axis will cause a change in range to translate to a greater number of pixels to be traversed by the beam in the detector. However, a greater baseline will allow less range measurement for a given detector-array size and laser power, and the longer the baseline becomes, the chance increases for occlusion to cause the beam to be blocked from reaching the detector.

Linear arrays of photodiodes may have more than 4000 elements. The number of positions that can be resolved by position sensitive photodiodes is in the same range. However, the space bandwidth product of photodiode arrays can be much larger than the number of pixels. Using proper choice of spot shape and evaluation of its center of mass via a computer algorithm, it is possible to resolve about 50 positions per pixel. Therefore, a limited number of detector elements is usually not the factor limiting the resolution of the technique. The limitation arises from speckle noise, which can vary the localization of the laser spot image as a function of the arbitrary microstructure of the spot. Many have researched the effect of speckle noise on the microstructure of a laser beam. One useful paper is [29]. It is evident

that a beam with the smallest spot size (diameter at the point where the beam strikes the target) should be used for highest range accuracy. The smaller the spot size, the better the center of the beam can be detected without as many problems from speckle noise.

A problem with all laser-triangulation techniques is that of specular reflection. Attempting to measure a surface which is too reflective may result in no range measurement if there is no scattering of light at the surface and the reflected light never reaches the camera. Also, errors in measured range values can occur if the reflected light is subsequently reflected by other surfaces before part of it reaches the camera.

Point triangulation sensors come in all shapes and sizes. Digital theodolites are used for large scale measurements of targets such as airplanes. These are made by Zeiss [30], Cubic Precision [31], and Brunson [32]. Cubic Precision makes the AIMS III which they claim has a range accuracy of 25 μm . Brunson makes the BETS (Brunson Electronic Triangulation System). They also claim a range accuracy of 25 μm . The BETS system uses as many as ten theodolites working simultaneously to measure large parts. The main problem with theodolites is that measuring more than a few points is very time consuming. The reason for this is that theodolites only measure in one dimension and the other two are determined by careful positioning of the theodolites and knowledge of those positions.

Smaller scale point triangulation sensors which can be retrofitted to CMMs are made by Perceptron [33], Measurement Technologies [34], and Medar [35]. Perceptron makes the DataCam sensor, and they claim a range accuracy of 50 μm at a rate of 15,000 points per second, for a price of \$6500 per sensor. Measurement Technologies makes the Percimeter II, and they claim a range accuracy of 0.2 μm with a total range of 3 mm and a range accuracy of 40 μm with a total range of 200 mm. The Percimeter II can measure 600 points per second.

Medar makes the MDR Range Sensor. They claim a range accuracy of 50 μm at a rate of 2,000 points per second. It uses an infrared laser diode, of frequency 780 nm, as its light source.

3.2.2 Scanning Point Laser Triangulation

Although point laser triangulation can take data points quickly, in order to increase data acquisition speed further, one needs a CMM to move the sensor back and forth very quickly. It is easy to see the practical speed limits of this technique. However, using similar geometric relations and more complex sensor design, it is possible to vastly increase measuring speed either by having the sensor control scanning along one axis and the CMM control motion along the other, or by having the sensor control scanning along both axes.

One design for a scanning point triangulation range sensor which controls scanning along one axis is shown below in Figure 3.4. A two dimensional CCD array is aligned along the z axis with the center of its lens positioned at $(0,0,0)$. At a baseline distance b from the detector along the x axis is a light projector sending out a beam of light at a variable projection angle θ relative to the x axis baseline. A two dimensional point x,z is projected into the digitized image at the pixel u . Thus, one can calculate that $uz = xf$ via similar triangles where f is the focal length of the detector lens, measured in pixels. The two dimensional x,z coordinates of the target point can be calculated from the measured values u,θ as shown in the following relations [17]:

$$x = \frac{b}{f \cot \theta - u} \cdot u \quad (3.3)$$

$$z = \frac{b}{f \cot \theta - u} \cdot f \quad (3.4)$$

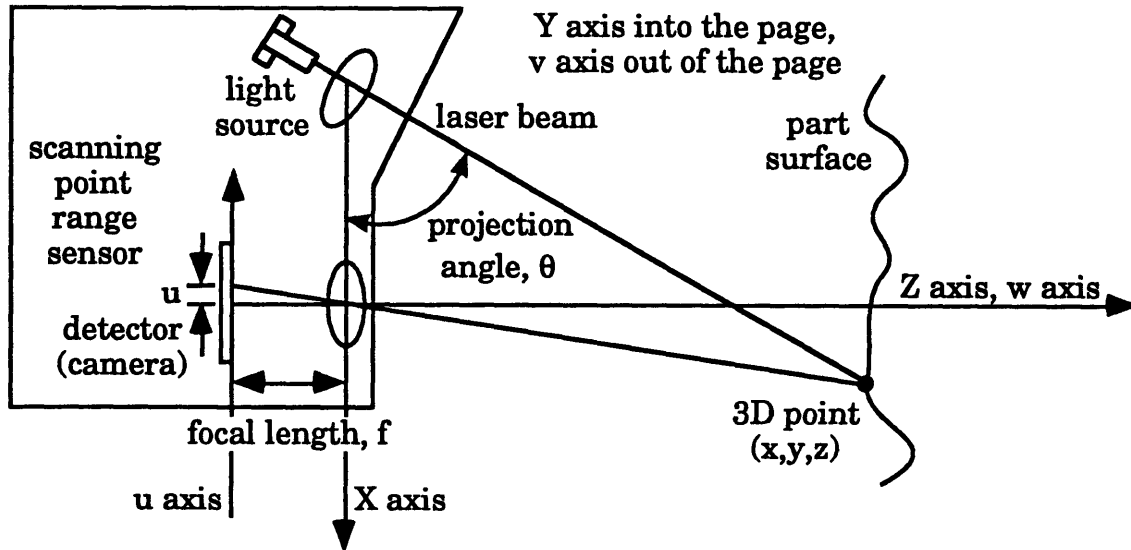


Figure 3.4: Camera Centered Point Triangulation

Synchronized scanning, a concept patented by Marc Rioux [36], increases the potential data acquisition speed by scanning a laser beam in two directions. In this technique, the linear position detector and the light projector are both scanned. The projection angle is coupled with the horizontal position measurement, allowing high range resolution with a small baseline by making more efficient use of the finite resolution provided by a linear detector. The only difference between synchronized scanning geometry and conventional scanning geometry is the addition of a detector scanner which moves synchronously with a projection scanner and has the effect of canceling its angular movement. This results in bringing the position of the spot on the sensor closer to the reference point. Therefore, a change in the position of the light spot along the z axis produces an equivalent angular shift for both geometries, but a change along the x axis produces a much smaller angular shift when using synchronized scanning geometry. By combining the two separate scanning mechanisms described above, a perfect synchronization can be obtained. This is done by using polygonal or pyramidal mirrors or a plane mirror coated on both sides. An example of this technique is shown below in Figure 3.5.

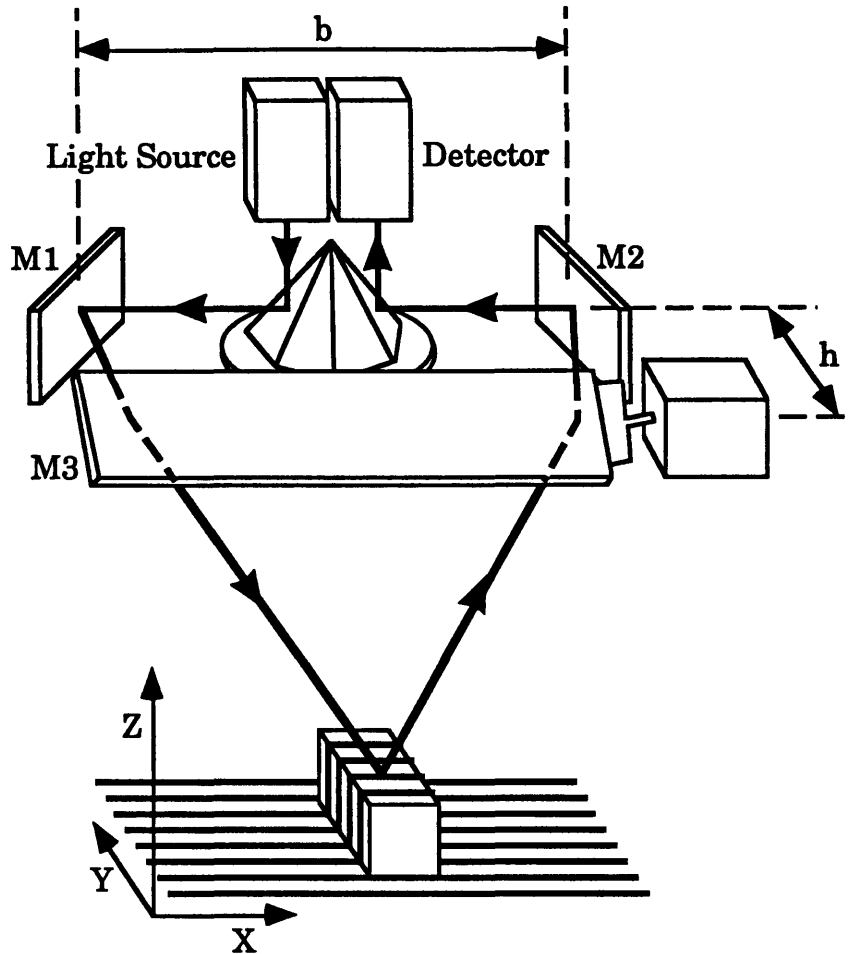


Figure 3.5: Autosynchronized Scanning, Adapted From [37]

With synchronization, the position sensor is mainly used to measure range, while in conventional geometries a large part of the position sensor area is also used to measure x coordinates. This is unnecessary because the position of the scanner mirror can be precisely obtained. If a sensor is designed that incorporates synchronization and uses the same position sensor that is used in conventional geometries, the focal length of the lens used to collect the light can be increased, providing an increased range resolution without reduction in the field of view.

In Figure 3.5, a laser diode and a linear CCD array are positioned next to each other and near a multifaceted pyramidal mirror. The beam leaves the source, hits the mirror facet currently rotated at angle θ to normal, reflects off a fixed mirror M1, reflects off a slowly scanning mirror M3, and impinges on a

target surface. The illuminated bright spot is viewed by the detector via the opposite side of the multifaceted mirror, a fixed mirror M2 separated by a fixed baseline distance b from the other fixed mirror, and the slowly scanning mirror M3. The horizontal position p of the bright spot at the detector is given by the following relation:

$$u(p) = w \cdot \frac{p + w \tan \theta}{w - p \tan \theta}, \quad w = \frac{r_0 f}{r_0 - f} \quad (3.5)$$

where $u(p)$ is the effective horizontal position if synchronized scanning was not used, w is the distance from the center of the focusing optics to the position detector surface, f is the focal length of the detector's lens, and r_0 is the average range to object surface points, determined by the angular positioning of mirrors M1 and M2. A vertical mirror M3 slowly scans, typically two orders of magnitude slower than the pyramidal mirror. M3 is rotated by an angle ϕ whose rotational axis is located a distance h from the baseline between the fixed mirrors. The three-dimensional coordinates of points on the target are determined by the values θ , ϕ , and p , the pyramidal scanning mirror angle, the vertical mirror M3 scanning angle, and the linear position detector value, respectively, via the following relations:

$$x = \frac{bu(p)}{u(p) + wa(\theta)} \quad (3.6)$$

$$y = \left(\frac{bw}{u(p) + wa(\theta)} - h \right) \sin(2\phi) \quad (3.7)$$

$$z = \left(\frac{bw}{u(p) + wa(\theta)} - h \right) \cos(2\phi) \quad (3.8)$$

where the angular function of horizontal scanning pyramid mirror is given by:

$$a(\theta) = \frac{b + 2r_0 \tan \theta}{b \tan \theta - 2r_0} \quad (3.9)$$

To the best of my knowledge, autosynchronized scanning provides the best combination of speed and accuracy currently commercially available. The speed of measurement is only limited by the ability to rotate the mirrors quickly yet still accurately and the ability of the computing system with which the device is used.

Scanning laser triangulation systems are commercially available from Hymarc [38] and Medar [39]. Hymarc makes the Hyscan 3-D Laser Digitizer. They claim a range accuracy of 25 μm for a depth of field of 40 mm, at a rate of 10,000 points per second, and at a cost of about \$90,000. The Hyscan sensor scans in two directions, using the autosynchronized scanning method described above. In fact, Hymarc works with Marc Rioux, who patented the concept of synchronized scanning. Medar makes the MDC contour sensor, and they claim a range accuracy of 25 μm . The MDC scans a laser beam in one direction (y) only. It can therefore be used to measure contours, or it can be retrofitted to a CMM which would move the sensor in the other horizontal direction (x).

3.2.3 Structured Light: Line, Grid

When a laser beam is passed through a cylindrical lens, a line of light is created. A scanning line triangulation system uses similar geometric relations to those presented in the previous section. However, instead of scanning a point in two directions and using a linear detector array, a line is scanned in one direction, and a two dimensional detector array is used. A typical line scanning technique is shown in Figure 3.6 below. Data collection may be faster with this method, but two dimensional CCDs are more expensive than linear CCDs, and range resolution may decrease because two dimensional CCD arrays are usually 256 by 256 or 512 by 512 pixels, where linear photodiode arrays or linear CCD arrays may have more than 4000 elements.

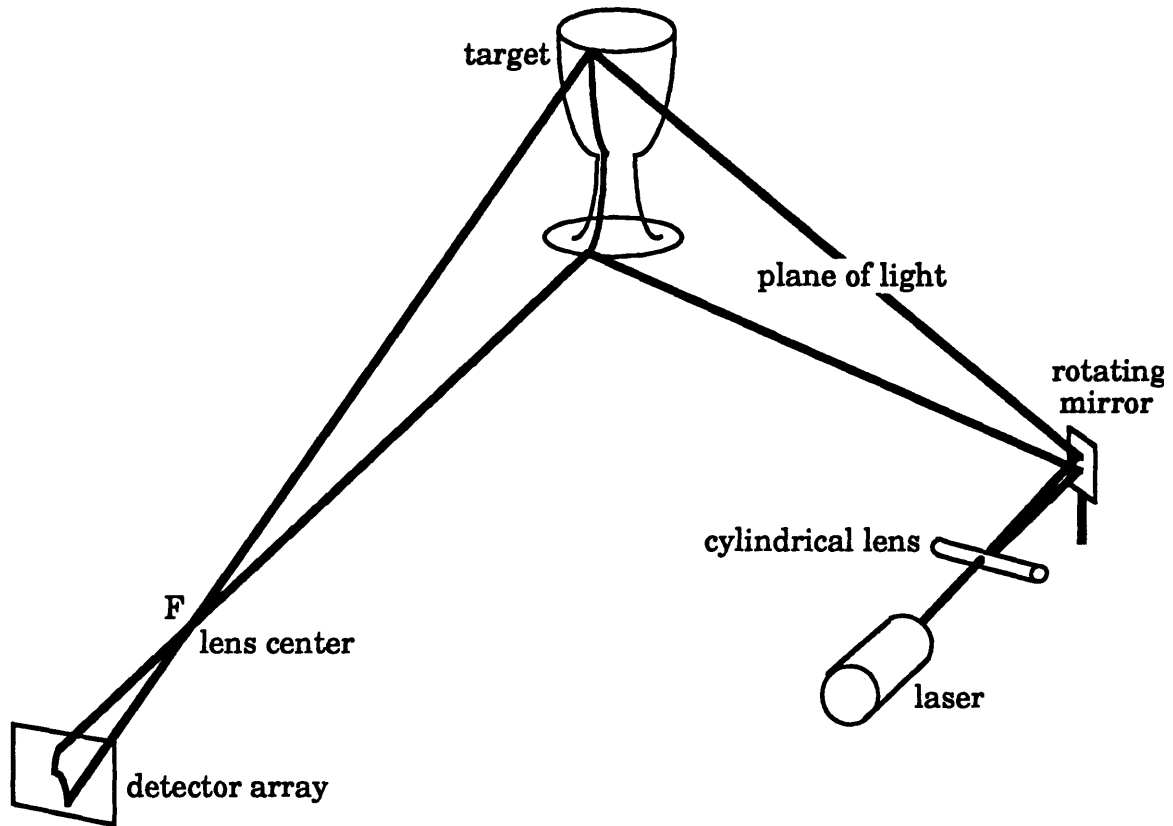


Figure 3.6: Line Scanning, Adapted From [40]

Another form of laser triangulation uses more complicated structured light. One could project multiple points, multiple lines, a grid of lines, or other geometric shapes onto a target, using a grating and one or more lenses. A two dimensional CCD array would serve as the detector, imaging the whole target at once, without scanning. The benefit of this type of technique is that there are no moving parts to break or become misaligned. However, using a two dimensional CCD with only 512 by 512 pixels will limit the range resolution. Also, the cross range resolution is limited by the spacing of lines projected onto the target.

United Scanning Technologies [41] makes the Replica system. The Replica uses a line scanning system similar to that shown in Figure 3.6 above. Intelligent Automation Systems [42] makes a structured light line sensor called the 4D-Imager, and they claim a range accuracy of 1/2000 of the field of view. They have achieved a data collection rate of 10,000 points per second, for up to 50,000 points in a single scene. Modular Vision Systems [43] makes

the MVS-30, which uses line scanning, and they claim a range accuracy of 75 μm . Phase Shift Technology [44] makes the Optiflat XAM, which is a large scale flatness measurement system. It projects a row of lines onto a part and uses a two dimensional CCD array to image the lines. The distortion of parts of the lines from linearity gives information about the range at each point. They claim a range accuracy of 20 μm with a data collection rate of 16,000 points per second.

3.2.4 Moiré Interferometry

A moiré pattern is defined as the low spatial frequency interference pattern created when two gratings with regularly spaced patterns of higher spatial frequency are superimposed on one another [17]. This phenomena is shown below in Figure 3.7, where two high frequency linear gratings are overlaid at an angle of 15° in order to create a low frequency pattern. Although this technique uses a type of interferometry, the angular separation of the light source and the detector is vital to range measurement. Thus, moiré can be considered another type of triangulation method.

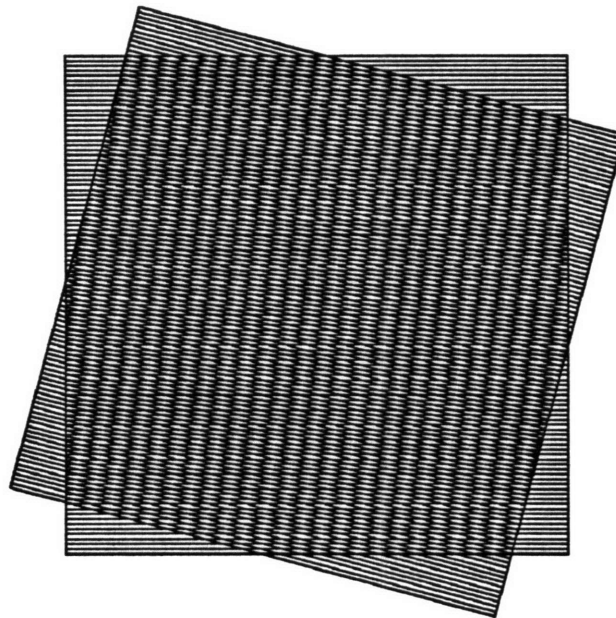


Figure 3.7: Moiré Fringe Pattern

Moiré methods usually use Ronchi gratings, line gratings of alternating opaque and transparent bars of equal width. As shown in Figure 3.7, a dark fringe is an imaginary line connecting all zones where light is blocked by interference of the opaque stripes, which are mutually translated by half a period. The bright fringes are the geometrical locus of the intersection point of the opaque stripes. The pitch of a grating, P , is specified by the number of opaque and transparent line pairs per millimeter. The period of the grating, $p = 1/P$, is the distance between the centers of two opaque lines.

A projection moiré setup is shown below in Figure 3.8. A focused light source, either a laser or white light, is projected through a master grating onto the surface of the target at an angle θ_1 relative to the z axis. The projected beam of light is spatially amplitude modulated by the pitch of the master grating. Using communication theory terms, a spatial carrier image is generated. When the projected beam falls on the target, the shape of the surface modulates the phase of the spatial carrier. By viewing the stripes of light through a viewing grating exactly matched to the master grating, interference fringes are created at the camera, located at an angle θ_2 relative to the z axis. The viewing grating demodulates the modulated carrier yielding a baseband image signal whose fringes carry information about the shape of the target. The change in height z between the centers of the interference fringes viewed by the camera is determined by the following relation:

$$\Delta z = \frac{p_0}{\tan(\theta_1) + \tan(\theta_2)} \quad (3.10)$$

where p_0 is the period of the projected fringes at the object surface.

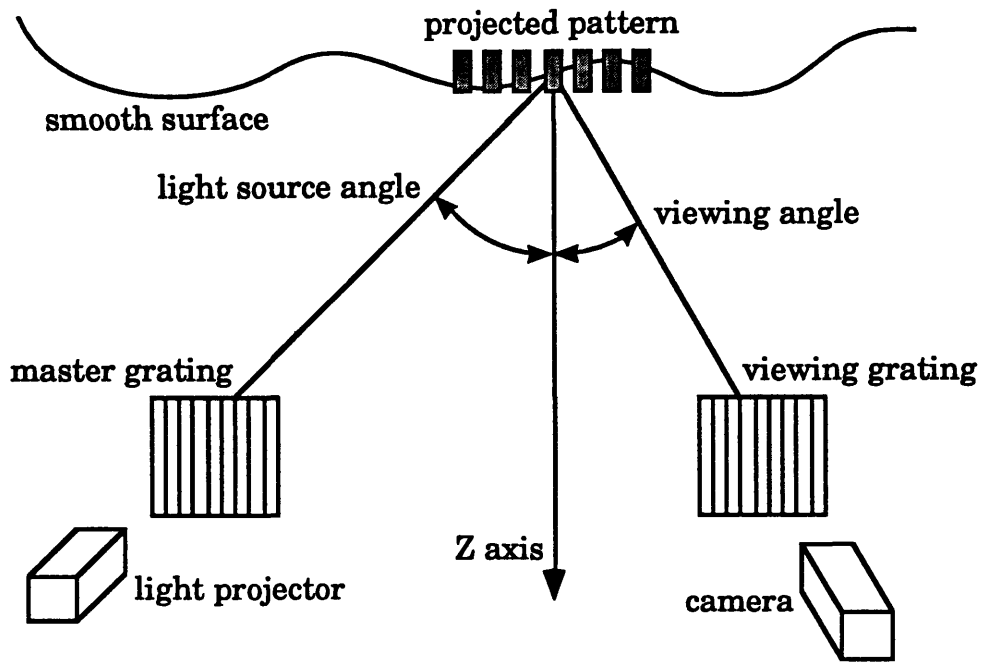


Figure 3.8: Projection Moiré Configuration, Adapted From [17]

It is relatively easy to create a projection moiré system using commercially available light projectors, cameras, and matched gratings. What presents a more difficult challenge is accurate calibration of the system and automated processing of moiré fringe images. The main purpose of fringe processing algorithms is to track the ridges or valleys of the fringes and create contours. Phase unwrapping techniques can be used to order the contours in depth.

Another technique, the shadow moiré method, can be used if the depth of field of the target surface is small. In this method, a single large grating is placed near the object surface. A light source projects light through the grating, and a camera views the target through the same grating, offset at an angle from the projector. This makes unnecessary the use of two exactly matched gratings as in projection moiré. The pitch of a shadow moiré grating should be more coarse than that of projection moiré gratings because the grating is placed much closer to the surface. The interference fringe images and the methods of fringe analysis are the same for shadow moiré as those used for projection moiré.

Another variation of the projection moiré method allows the projected grating on a target to be imaged directly by a camera without a viewing grating. The camera images are digitized and demodulated using computer software, provided that a reference image of a flat plane is also digitized. Systems of this type are generally able to achieve range resolution proportional to about 5% of a fringe spacing [17]. Electro-Optical Information Systems, Inc. [45] makes a commercially available range measurement sensor of this type, the Mini-Moiré sensor. On appropriate surfaces, their system can create a 480 by 512 pixel image in about two seconds. The system uses two array processors and has a range resolution of 1/4000 the depth of field. Gratings of two to ten line pairs per millimeter are used.

Phase shifted moiré interferometry takes multiple (N frames) phase shifted images of a target. It operates in the same manner as single image moiré methods, but the master grating is precisely shifted laterally in the projector by a small distance increment corresponding to a phase shift of $360/N$ degrees, and subsequent images are acquired. Using similar equations to those used in projection moiré, the phase (sub-fringe) information can be calculated from the variation in gray scale at each point in the image. Typically, the depth of one fringe order is broken into 8 bits. However, a limitation of this technique is that there is an ambiguity of which fringe a measurement point is on, so the phase can not be calculated beyond one cycle of the fringe. Using phase shifting allows for an order of magnitude increase in range accuracy compared to more conventional moiré methods. Halioua and Srinivasan [46] have patented this general concept for moiré. A system of this type is commercially available from Medar [47], the Cadeyes system. They achieved a data collection rate of 50,000 points per second. Over a field of view of 50 mm by 38 mm, and a depth of field of 10 mm, a depth accuracy of 3.75 μm was obtained. Another system using this technology is the Bazic series, made by View Engineering [48]. They claim a range accuracy of 2.5 μm .

The main disadvantage in moiré measurement methods is that they are generally only useful for measuring the relative range points on a smooth surface that does not exhibit large depth discontinuities. A height change of

more than one fringe creates an ambiguity problem of how many fringes separate the two surfaces on either side of the depth discontinuity. To remove this ambiguity, a small angle between the illumination and viewing axis or a very coarse grating period can produce a fringe period which is much larger than the step change of interest [49]. With modern computing capabilities, a moiré fringe pattern can be created and analyzed which never passes through a full fringe period. Using a coarse contour interval avoids the problem with fringe counting, but the range resolution of measurements becomes limited. The moiré contour interval must be made large enough such that an expected depth discontinuity is not larger than the contour interval. An alternate approach to solving ambiguity from a large step discontinuity is to use a two step measurement method. A large fringe interval can be created to accommodate the full usable range of the moiré. Then, a second, finer pattern analysis can provide better resolution to the measurement. As long as the course measurement has enough resolution to keep track of the finer fringe order, the analysis will not have problems going over step changes [50].

3.3 Passive Non-Triangulation

3.3.1 Range from Focus

Although there are a plethora of techniques which use triangulation to calculate range, there are also plenty which use other methods. Range from Focus works basically by moving a lens such that different ranges are in focus at different lens positions.

The Gauss thin lens law states that a thin lens of focal length f focuses a point light source in a scene at a distance z from the center of the lens onto a focal plane behind the lens at a distance w from the lens center via the following relation:

$$\frac{1}{w} + \frac{1}{z} = \frac{1}{f} \quad (3.11)$$

The basic thin lens focusing relationships are shown below in Figure 3.9.

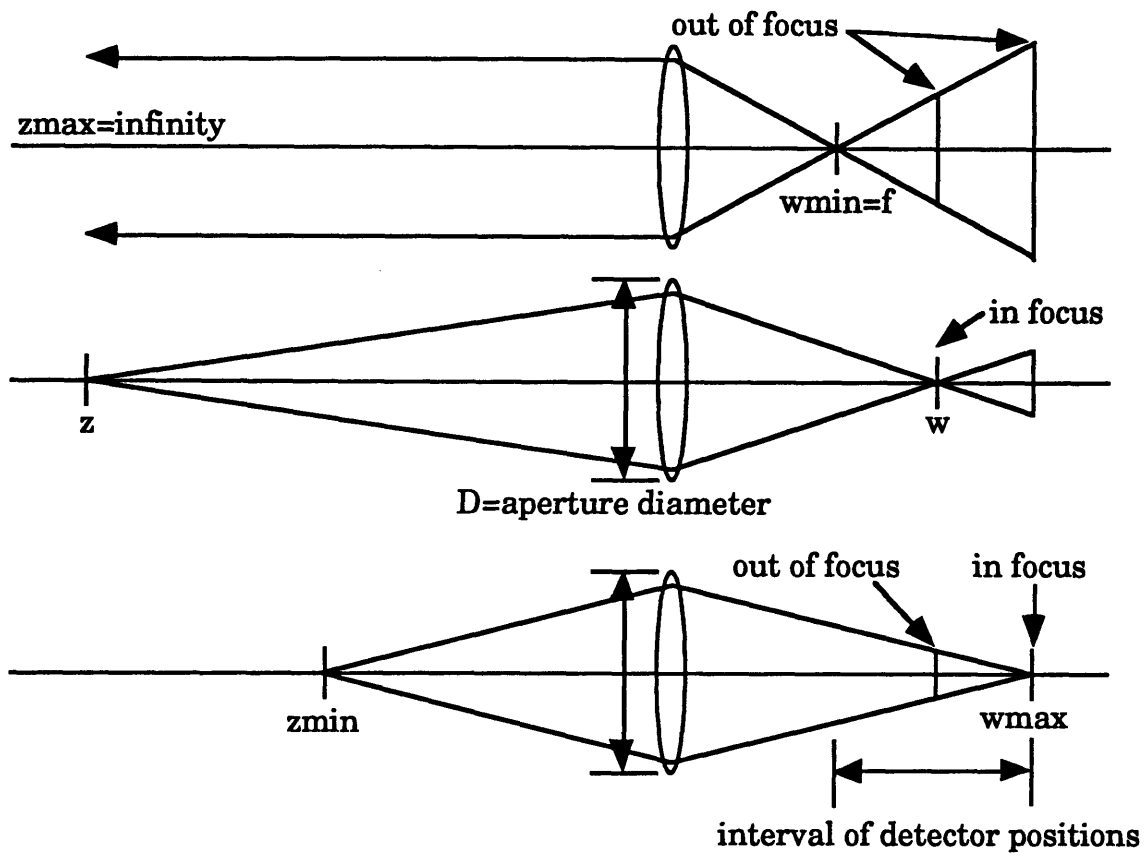


Figure 3.9: Thin Lens Relationships, Adapted From [17]

It is easy to discern that as w varies from its minimum value of f to a maximum value w_{\max} , points at ranges from infinity to the corresponding z_{\min} are in focus. Since a camera lens has a finite aperture of diameter D , and light which passes through a finite aperture experiences diffraction, images are blurred to a certain degree. The radius of the blur of a point at range z is at a minimum when the point is in focus at $w = w(z)$. The blur increases in size as w varies from $w(z)$ in either direction. If a point blur is modeled as a two-dimensional Gaussian intensity distribution of diameter σ for a fixed focal plane distance w , the range to this point is determined via the following relation:

$$z_{\pm}(\sigma) = \frac{wf}{w - f \pm \sigma F}, \quad F = \frac{f}{D} \quad (3.12)$$

where F is the f number of the lens aperture. If the blur characterized by sigma is small enough to maintain adequate focus, the depth of field L_z of the camera in which all points are in adequate focus is determined in the following relation [17]:

$$L_z = z_-(\sigma) - z_+(\sigma) = \frac{2wf\sigma F}{(w-f)^2 - \sigma^2 F^2} \quad (3.13)$$

From the above relation, it is clear that the depth of field increases with increasing f -number F . In photography, having a large depth of field in focus is desired. In a range from focus system, however, a small depth of field makes it easier to determine relative ranges in a target.

In a typical range-from-focus system, the sharpness of focus needs to be measured over a series of lens positions to determine the range of the corresponding points on the target. Large lens apertures shorten the depth of focus and enhance focus position discrimination of objects at different ranges. Jarvis [51] suggests some simple computational formulas for sharpness of focus evaluation.

The range resolution of such a system would depend on the formulas used and the number of lens positions used to image the target. However, as with stereo vision, the range in visually homogeneous regions of the image can not be determined directly.

Range from focus can be used with structured light to become an active technique. Rioux and Blais [52] designed a compact range-imaging sensor based on a range-from-focus technique. The technique features a grid of points projected onto a target. The range to each point is determined by the radius of the blur in the focal plane of the detector lens. The system was capable of measuring depths for 144 points with 1 mm resolution over a 100 mm depth of field. There are many possibilities for systems using combinations of depth from focus and structured light.

MicroVu [53] makes the Vector and Matrix Series Video CMM's, which use a focusing scheme to determine range. Ram Optical Instrumentation [54] also makes a device which uses range from focus. They make the Optical Measurement Inspection System (OMIS).

3.3.2 Other Passive Non-Triangulation Techniques

There are many passive ways to obtain range information for an object. Many have low accuracy or are qualitative. Research has been done on obtaining range from occlusion clues, texture gradient, surface orientation, and shadows. Nitzan [18] and Jarvis [24] have written reviews which include these methods of determining range. However, because of the limits on accuracy and the types of parts which can be measured, these methods are inappropriate for use in manufacturing systems and are therefore beyond the scope of this work.

3.4 Active Non-Triangulation

3.4.1 Fresnel Diffraction

Any wave experiences diffraction when it passes through a finite aperture. If an aperture is illuminated by a plane wave and the Fresnel diffraction pattern is formed on a planar surface at an unknown range from a detector, the size and shape of the diffraction pattern can be used to determine the distance from the plane to the detector. Extension of this principle allows for measurement of absolute distances and therefore the determination of the range of three-dimensional objects [55].

The Talbot effect is often referred to as the self-imaging property of a grating. It states that any amplitude distribution $a(x,y)$ which is a periodic function of x and y will also be periodic in the direction of propagation (z) [56]. A cosine grating is a simple periodic object. If such a grating is oriented with the lines in the vertical direction, the grating is periodic in the horizontal direction. When an on-axis plane wave illuminates this grating, an image of the grating will be formed at specific locations along the z axis.

Consider a cosine grating of frequency f_0 with an amplitude distribution given by the following expression (one dimensional notation is used for simplicity):

$$a(x) = c + m \cos(2\pi f_0 x) \quad (3.14)$$

where c is the bias, and m is the modulation index of the grating. When this grating is illuminated by an on-axis plane wave, the amplitude of the angular plane wave spectrum at a particular distance z from the grating is given by the following relation:

$$a(x, z) = e^{j2\pi\frac{z}{\lambda}} \left[c + m \cos(2\pi f_0 x) e^{j2\pi\frac{z}{\lambda}(\sqrt{1-(\lambda f_0)^2} - 1)} \right] \quad (3.15)$$

Notice that other than an overall phase factor, the amplitude distribution in Equation 3.15 is identical to the original cosine grating (Equation 3.14) when the following expression is true:

$$z = \frac{n\lambda}{\sqrt{1-(\lambda f_0)^2} - 1}, \quad n = \dots -2, -1, 0, 1, 2, \dots \quad (3.16)$$

The intensity of the angular plane wave spectrum at a distance z is equal to the squared magnitude of the amplitude (Equation 3.15). This intensity is given by the following relation:

$$I(x, z) = |a(x, z)|^2 = c^2 + m^2 \left[\frac{1}{2} + \frac{1}{2} \cos(4\pi f_0 x) \right] + 2mc \cos(2\pi f_0 x) \cos \left[2\pi \frac{z}{\lambda} \left(\sqrt{1-(\lambda f_0)^2} - 1 \right) \right] \quad (3.17)$$

It can be seen from the third term in Equation 3.17 that the fundamental frequency of the grating, f_0 , is modulated in depth, z , by a cosine function with a period given by:

$$Z_T = \left| \frac{\lambda}{\sqrt{1-(\lambda f_0)^2} - 1} \right| \quad (3.18)$$

The value of this term is governed by both the bias, c , and the modulation index, m , of the grating used. Note that the term vanishes when $c = 0$. This modulation of the fundamental frequency term of Equation 3.17 can be used to encode the depth information of a three-dimensional object onto a two dimensional image.

Demodulation of the grating pattern intensity which is reflected from a target to a detector produces an image of the target whose intensity varies sinusoidally with range. Range planes which satisfy Equation 3.16 are called positive Talbot planes. These planes reflect an image identical to that of the original cosine grating. Therefore, the positive Talbot planes correspond to maximum positive cosine modulation of the angular plane wave spectrum. Halfway between each positive Talbot plane, the cosine modulation becomes maximally negative, so these planes reflect an image of the original cosine grating with a phase shift of 180° and are therefore called negative Talbot planes.

When the grating period is large compared to the wavelength of light used, the Talbot period of Equation 3.18 can be approximated by the following:

$$Z_T \approx \frac{\lambda}{(\lambda f_0)^2 / 2} = \frac{2d_0^2}{\lambda}, \quad d_0 = \frac{1}{f_0} \quad (3.19)$$

The Talbot effect described above can be used to determine the range values of a three-dimensional object. In one system [57], shown below in Figure 3.10, a plane wave illuminates a grating, and a three-dimensional target is placed in one of the Talbot planes of the grating. A two dimensional detector views the illuminated object through a beam splitter. The grating superimposed on the object image is modulated both by the distance of the object from a Talbot plane and the reflectivity of the object. This means that the intensity at particular point x,y on the image reflected back to the detector will depend upon its range to the grating and its relative reflectivity with respect to the rest of the target. Therefore, the range information can be extracted by demodulating the grating signal and normalizing the result with respect to the reflectivity of the target. This demodulation is done using the contrast level at each range plane. Positive and negative Talbot planes exhibit maximum contrast between light and dark points, while planes between them have less contrast. The planes at “zero crossings” of the angular plane wave spectrum, located midway between positive and negative Talbot planes, have no contrast between points.

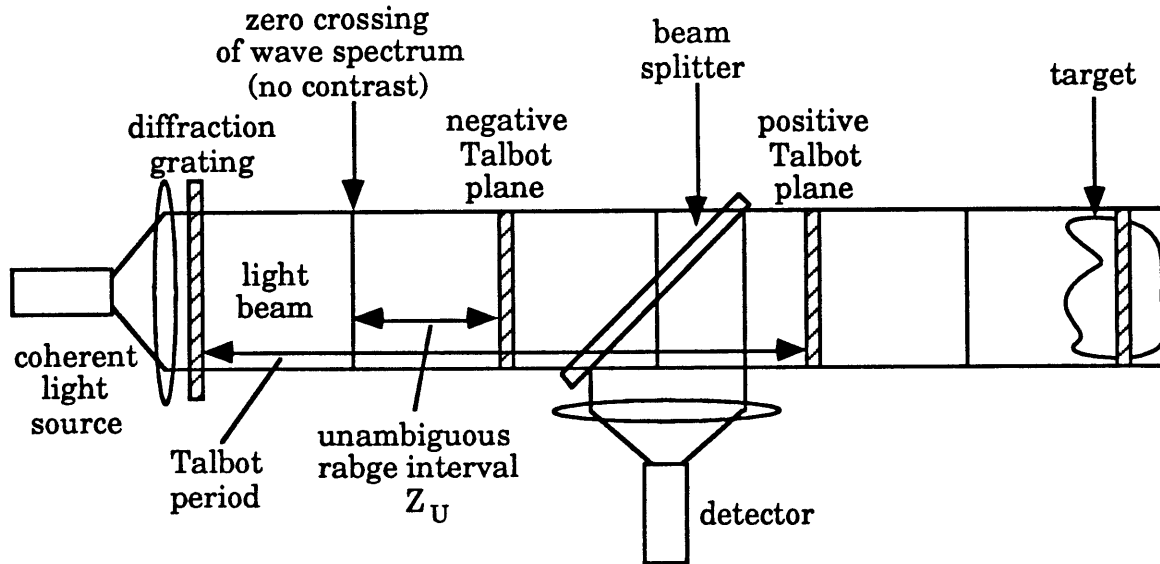


Figure 3.10: Fresnel Diffraction System, Adapted From [55]

Because of the periodic nature of the angular wave plane spectrum, the intensity pattern is repeated every Talbot plane. Since the positive and negative Talbot planes are identical except for a 180° phase shift, it is impossible to tell the difference in range between parts of a target separated by more than the distance between a positive and negative Talbot plane if a phase unwrapping technique is not used. Therefore, the depth of field is limited by an ambiguity interval equal to this distance, which corresponds to one quarter of a Talbot period. The maximum unambiguous depth of field is therefore given by the following expression:

$$Z_U = \frac{Z_T}{4} = \frac{d_0^2}{2\lambda} \quad (3.20)$$

The range accuracy of a Fresnel diffraction imaging system would be limited by the resolution of the detector to detect intensity differences. The cross range accuracy of the system would be limited by the number of pixels in the detector and the ability to interpolate between the intensity values detected. The maximum depth of field is dependent upon the spacing of the grating used and the frequency of light used. However, the depth of field can be

extended by the phase unwrapping techniques discussed in Section 3.2.4 on moiré interferometry.

Although prototype three-dimensional imaging systems using Fresnel diffraction have been developed [55,57], no sensors using this technique are commercially available.

3.4.2 Pulse Laser Radar

Laser radar systems obtain three-dimensional coordinate information by interrogating a scene with a beam of light, usually a laser pulsed or modulated in some way. The light reflects off the target, returns to a receiver system, and is detected. Range information is obtained by determining the time it took the light beam to travel to the target and return, either by direct timing or by measuring the phase of the returned signal that has been amplitude or frequency modulated. Higher accuracy can typically be obtained when using phase detection, which can be taken over many cycles. The reason for this is that direct timing of light travel requires a very high speed detector.

The most basic laser radar system is the pulse technique. This technique involves sending a pulse from a laser diode or other light source to reflect off of a target and recording the time it takes for the light to return to a detector. The start or reference pulse is recorded when the light is transmitted, and the stop pulse is recorded upon return of the reflected light. The target range can be determined via the following relation:

$$z = \frac{c}{2} \Delta t \quad (3.21)$$

where c is the speed of light and t is the time that the light pulse took to strike the target and return to the detector. This is basically a one dimensional range finding technique, but it is easy to make it a three-dimensional technique by scanning the direction of the laser beam pulses in two dimensions in a manner similar to those described in Section 3.2.2 on scanning point laser triangulation.

The principal problem which limits the range resolution and accuracy of this technique is that light travels too fast relative to the time resolution which current photodiodes are capable of measuring. Currently, the best detectors

can resolve a time difference of about 100 picoseconds. This allows for a range resolution of a few centimeters. To be used in most industrial applications, a two to three order of magnitude improvement in time measurement technology would be required. Until this happens, the pulse technique is limited to lower accuracy, large scale uses, such as measuring buildings or remote sensing of aircraft.

Lübbers et. al. [58] have developed a pulse laser radar system capable of a range resolution of 5 cm. This low accuracy has prevented widespread use of this technique in manufacturing applications.

3.4.3 Amplitude Modulation Continuous Wavelength (AM CW)

Instead of sending out a short light pulse, waiting for it to return, and measuring the time of the trip, a laser beam can be amplitude modulated by varying the drive current of a laser diode at a frequency $f_{AM} = c/\lambda_{AM}$, where c is the speed of light, and λ_{AM} is the wavelength of the laser. An electronic phase detector measures the phase difference $\Delta\phi$ (in radians) between the transmitted signal and the received signal to get the range via the following relation:

$$r = \frac{c}{4\pi f_{AM}} \Delta\phi = \frac{\lambda_{AM}}{4\pi} \Delta\phi \quad (3.22)$$

Since relative differences in phase can only be determined modulo 2π , the range to a point on a target can only be determined within a range ambiguity interval r_{ambig} , as shown below in Figure 3.11. Without the benefit of an ambiguity resolving mechanism, the depth of field of an amplitude modulation laser radar is equal to the ambiguity interval r_{ambig} , which can be calculated using the following relation:

$$r_{ambig} = \frac{c}{2f_{AM}} = \frac{\lambda_{AM}}{2} \quad (3.23)$$

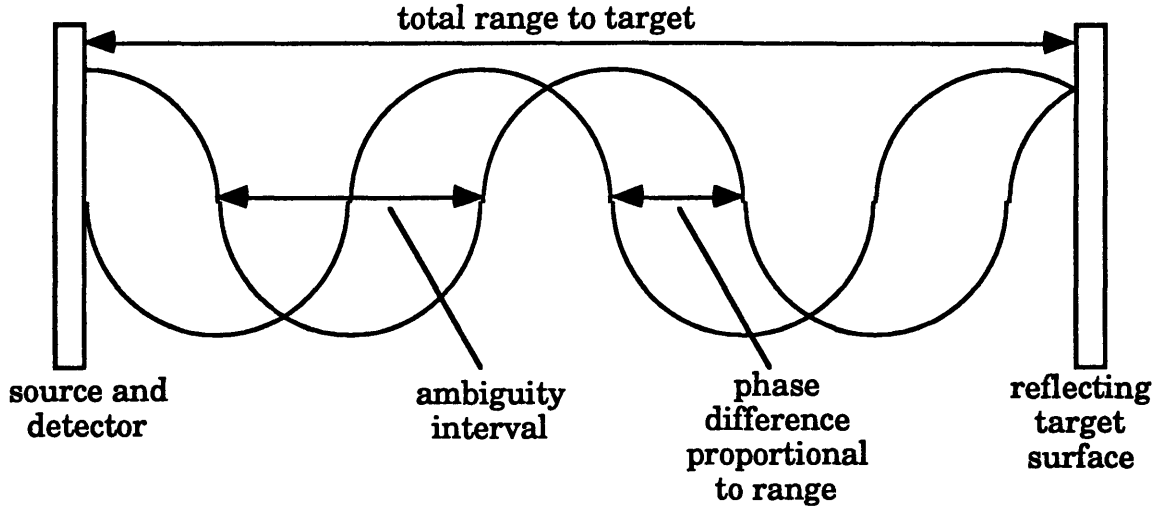


Figure 3.11: AM CW Radar Principles, Adapted From [17]

Better range resolution and smaller ambiguity intervals are achieved by using higher modulating frequencies. The RMS range accuracy σ_r depends on the properties of the phase detection circuit and the signal to noise ratio, SNR. Under ideal low signal conditions, the noise at the detector is dominated by the signal photon shot noise, and the SNR is given by the square root of the average number of photoelectrons n_e released within a pixel dwell time T , as shown in the following formula [17]:

$$SNR = \sqrt{n_e} = \sqrt{\frac{P_R T \eta}{h\nu}} \quad (3.24)$$

where η is the quantum efficiency of the photon detector, h is Plank's constant, and ν is the optical frequency. Nitzan et. al. [59] derived an approximate expression for the RMS range error (assuming 100 percent modulation index) yielding the following expression:

$$\sigma_r = \frac{r_{ambig}}{\sqrt{2\pi SNR}} \quad (3.25)$$

The ambiguity interval problem in amplitude modulated continuous wavelength radars can be resolved with software or hardware. If the imaged target is limited in surface slope relative to the sensor, it is possible to unwrap the phase ambiguity in software because the phase gradient will always exceed

the surface gradient limit at the phase wraparound pixels [17]. In hardware, a system could simultaneously use multiple modulation frequencies. One frequency would be relatively low to obtain a rough estimate of the surface shape, and the second would be higher, to allow for good range resolution. The known surface from the low frequency component would be used to unwrap the phase from the higher frequency component. This method is similar to that used in interpreting depth discontinuities in moiré interferometry, discussed earlier in this chapter.

Perceptron [60] produces a commercially available AM CW system, the Lasar System. Using two mirrors, they scan a laser beam in two dimensions in a manner similar to that described in Section 3.2.2 on scanning-point laser triangulation. The first is a multisided polygonal mirror rotating at a constant speed, which controls the scanning rate along the x axis. The second is a tilting planar mirror, which controls the scanning rate along the y axis. The device can scan a total of 1024 by 2048 pixels, which is limited by the RAM contained in the device. The data acquisition rate is 27300 points per second [61]. The device has a range accuracy of 2.5 μm at the minimum ambiguity interval of 2 m, a minimum standoff of 1 m, and an ambiguity interval of 2 to 40 m. In 1995, the device has a retail price of \$75,000.

3.4.4 Frequency Modulation Continuous Wavelength (FM CW)

The optical frequency of a laser diode can be tuned thermally by modulating the laser diode drive current or tuned mechanically by changing the length of the external cavity of an external cavity diode laser. As shown in Figure 3.12 below, if the transmitted optical frequency is repetitively swept linearly between $\nu_0 \pm \Delta\nu/2$, creating a total frequency of $\Delta\nu$ during the period $1/f_m$, (f_m is the linear sweep modulation frequency), the reflected return signal can be mixed coherently with a reference signal at the detector to create a beat frequency f_b signal that is dependent upon the range to the target r [62]. This detection process is known as frequency modulation coherent heterodyne detection. The range to the target is proportional to the beat frequency in an FM CW radar, as calculated in the following expression:

$$r = \frac{cf_b}{4f_m\Delta\nu} \quad (3.26)$$

One method for measuring the beat frequency is counting the number of zero crossings N_b of the beat signal during a ramp of the linear sweep frequency modulation. Using this method, range can be calculated via the following relation:

$$r = \frac{c}{2\Delta\nu} N_b, \quad N_b = \frac{f_b}{2f_m} \quad (3.27)$$

The range values calculated by this method are determined to within $\delta r = \pm c/4\Delta\nu$ since N_b must be an integer. The maximum range of an FM CW radar should satisfy the constraint that $r_{\max} \ll c/f_m$. Since it is difficult to insure the exact optical frequency deviation $\Delta\nu$ of a laser diode, it is possible to measure range indirectly by comparing the N_b value with a known reference count N_{ref} for an accurately known reference distance r_{ref} as follows:

$$r = \frac{r_{\text{ref}}}{N_{\text{ref}}} N_b \quad (3.28)$$

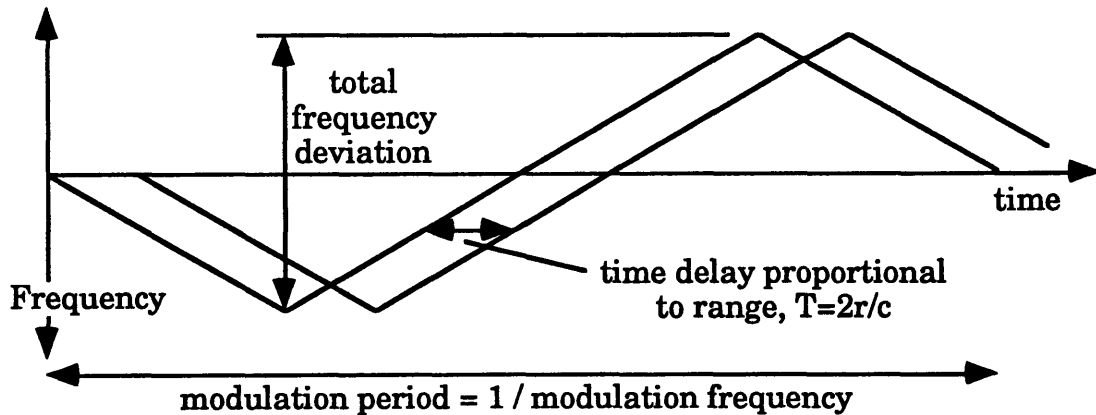


Figure 3.12: FM CW Linear Ramp Principles, Adapted From [17]

As in the case of AM CW laser radar, FM CW laser radar is a one dimensional technique. However, it is easy to make it a three-dimensional technique by scanning a laser beam in two dimensions in a manner similar to

those described in Section 3.2.2 on scanning point laser triangulation. Hersman et. al. [63] reported results for two commercially available FM CW imaging laser radar systems. One system, meant more for robot guidance, had a range accuracy of 12 mm for a one meter depth of field, taking four 256 by 256 frames per second. The other system had a range accuracy of 50 μm in 0.1 seconds over a depth of field of 2.5 m. Although this technique has several advantages, it is not yet widely commercially available.

3.4.5 Holographic Interferometry

Holography was introduced in 1961 by Leith and Upatnieks [64], and the principles of holographic interferometry were discovered in 1979 [65,66]. Holographic interferometry uses coherent light from laser sources to produce interference patterns due to the optical frequency phase differences in different optical paths. In many ways, holographic interferometry is similar to moiré interferometry. With moiré techniques, the range between moiré interference fringes is proportional to the spacing of the grating used. With holographic interferometry, the range between holographic interference fringes is proportional to the wavelength of the light being used. As with moiré techniques, holographic interferometry is limited to measuring smoothly varying surfaces. However, since the fringes in this technique are usually spaced closer together than moiré fringes, the magnitude of allowable surface height discontinuities is smaller.

Figure 3.13 below presents a typical holography setup (see [67] for other arrangements). Here, a laser beam is split in two using a beamsplitter. One of the partial waves is reflected off of a mirror, then expanded, and it finally strikes the entire target. The target scatters the light in all directions, some of it impinging onto a hologram plate. This wave is called the object wave. The other partial wave is reflected directly onto the hologram plate. This wave is called the reference wave. In Figure 3.13, the reference wave is collimated before striking the hologram plate. This is not essential, but it is necessary that the reference wave provides a uniform illumination of the hologram plate [68]. The hologram plate must be a light sensitive medium [69], most commonly a silver halide film plate with high resolution.

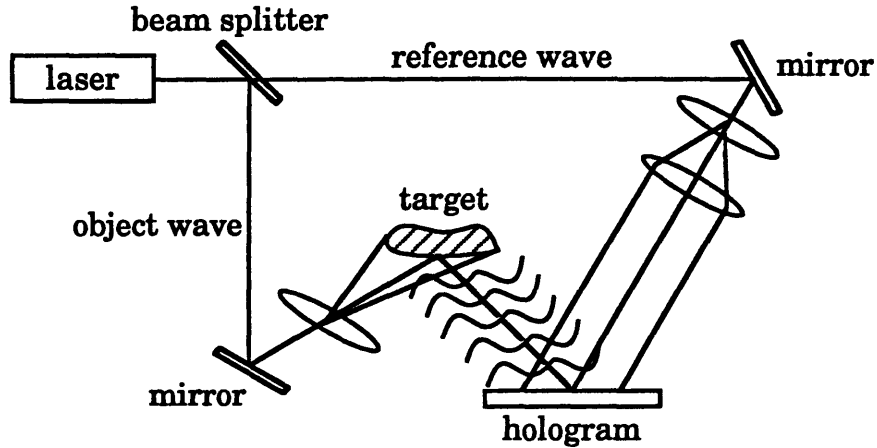


Figure 3.13: Example of a Holographic Setup, Adapted From [68]

Let the object and reference waves in the plane of the holographic plate be described by the field amplitudes u_o and u , respectively. These two waves will interfere, resulting in an intensity distribution in the hologram plane given by the following relation:

$$I = |u_o + u|^2 = I_o + I + 2\sqrt{I_o I} \cos \Delta\phi \quad (3.29)$$

where I_o and I are the intensities of u_o and u , and $\Delta\phi$ is the phase difference of the partial waves. The film plate is exposed by this intensity distribution to produce a latent image, and it is then removed from the plate holder and developed. The developed image is called a hologram, and the process which made it is called hologram recording. The hologram is then replaced into the plate holder in the same position as in the recording. We next illuminate the hologram with the reference wave which is now called the reconstruction wave. The amplitude distribution just behind the hologram is then equal to the field amplitude of the reconstruction wave multiplied by the amplitude transmittance of the hologram, which is proportional to the intensity distribution of Equation 3.29. The resultant intensity distribution differs from the recording intensity distribution only by a constant, maintaining its original phase and amplitude distribution. The consequence is that we can observe a

three-dimensional image of the original object by looking through the hologram in the direction of the original object. For a more detailed mathematical description of holography see [68].

By using the holography recording concept described above, several holographic interferometry techniques have been developed. In conventional holography, the optical frequencies of the interfering beams are equal. In real time conventional holography, a single recording of the object in a reference state is made. Then, the hologram is processed and replaced into the same position as the recording. By looking through the hologram, we can now observe the interference between the reconstructed object wave and the wave from the real object in its original position, as a pattern of fringes. By reconstructing the hologram, the wave scattered from the object in each new state will be reconstructed simultaneously with the wave from the original state and interfere, producing an pattern of interference fringes at places of deformation. In this manner, a deformation process can be observed in real time by watching the changes in the interference pattern. Interference fringes appear where the surface of the object varies from the shape of the surface when the hologram was made. If only an initial and final state are desired, however, double exposure conventional holography is used. In this method, two exposures of the object are made on the same hologram. These might be recordings before and after the object has been subject to load or some other deformation. Another variation, time average conventional holography, produces a hologram while an object is vibrated. A vibration mode map is obtained, which is useful for verifying finite element analysis [17].

Heterodyne holographic interferometers use two coherent beams of slightly different optical frequencies (less than 100 MHz difference). These two beams interfere, creating time varying holographic fringes in the image plane. Optical phase measurements which correspond to range differences can be made at each point by electronically measuring the phase of the beat frequency signal relative to a reference signal. This time varying interference fringe image must be mechanically scanned using a high speed detector in order to obtain a range image. Heterodyne holographic interferometers can

make out of plane surface measurements with nanometer resolution over a field depth of several microns, but they are generally slow. A general rule is that $\lambda/1000$ range resolution is possible using heterodyne interferometry [17].

Phase shifted holographic interferometers are usually referred to as quasi-heterodyne since the $\lambda/100$ range resolution obtained is not quite heterodyne performance, but it is much better than conventional interferometry. Phase shifted holography systems can be much cheaper, faster, and less complex than heterodyne systems at the expense of some range resolution. This method is similar to conventional holography in that the use of only one frequency is necessary, but instead of changing the state of the target, one can change the path length of the reference beam. This is usually done by introducing a piezoelectrically controlled mirror into the path of the reference beam. As the path length is changed, the interference fringes in the hologram shift. This allows one to detect range differences smaller than the fringe spacing. A two dimensional CCD array can then be used to record the interference fringe image at each position of the mirror. Using similar methods to those used in phase shifted moiré interferometry, described in Section 3.2.4, the phase information can be calculated from the variation in intensity between frames at each pixel in the CCD array. In one implementation of phase shifted holographic interferometry [70], a range resolution of $4.2 \mu\text{m}$ was achieved with a depth of field of $250 \mu\text{m}$.

Zygo [71] makes the New View 100, which uses scanning white light interferometry to determine range. This is done in a manner vary similar to conventional holography, but instead of recording a reference hologram on a plate, an electronic image is used as a reference with which the frames taken can interfere. They claim a range resolution of 0.10 nm , with a step height accuracy of 1.5% of the total range. The maximum vertical height allowed without ambiguity is $100 \mu\text{m}$. Wyko [72] makes the Wyko 400 Laser Interferometer, which works in a manner similar to the Zygo device, but it uses a laser light source of 633 nm or 1060 nm . They claim a range accuracy of $\lambda/20$. The scale of these devices, as well as that of most holographic interferometers, is too small to use to determine the shape of sheet metal

parts on a macroscopic level. This technology is better for determining small deflections in shape from pressure or stress.

3.4.6 Laser Speckle Wavelength Decorrelation

The newest type of laser radar is laser speckle wavelength decorrelation. This method of range finding is not yet available in any commercial sensors, but the technique is currently being researched [2, 73, 74]. The laser speckle technique is similar to frequency modulation continuous wavelength methods, but instead of detecting the interference between light reflected off of one point and a reference, a full field strategy is used. The entire target is illuminated with a laser beam, and a detector records the interference between light reflected off of all points on the target at once, as well as light reflected off of a reference object. This method allows measurement of a whole target at once, but much more mathematical calculation is necessary.

Since the three-dimensional imaging method I am researching most in depth uses laser speckle wavelength decorrelation, Chapter 4 is devoted entirely to explaining the theory behind this technique and discussing the details of one possible implementation.

4

How Laser Speckle Works

4.1 What is Laser Speckle?

A speckled pattern is one which is composed of small spots or specks of different colors or shadings. When light strikes an object, a speckled interference pattern is reflected back. The geometry of this pattern is determined by the microstructure of the object struck by the light. For several years, speckle has been known as a nuisance which creates variation in the intensity across a beam of light reflected off of an object. Much has been done to understand how speckle can degrade measurements using lasers, but research concerning the benefits of speckle was not pursued until relatively recently.

Some [2, 73, 74] have investigated speckle for the information which it carries, but no commercial imaging products currently use a laser speckle based technique. Shirley et. al. [2] have developed a three-dimensional imaging technique based on the information about a target carried in the speckle pattern reflected back from it.

4.2 Finding Range Data from Laser Speckle

Shirley et. al. [2] use a theory called wavelength decorrelation to obtain range information from a reflected speckle pattern. In Figure 4.1 below, the

reflected speckle pattern (a), carries information concerning the shape of the target (b). The pattern shown in Figure 4.1 (a) is the result of using a single wavelength. Since the speckle pattern is an interference phenomenon, one would expect it to change with a change in frequency. The frequency shift required for inducing one complete 360° cycle of phase of the highest frequency component of the speckle pattern is the decorrelation frequency, $\Delta\nu_D$.

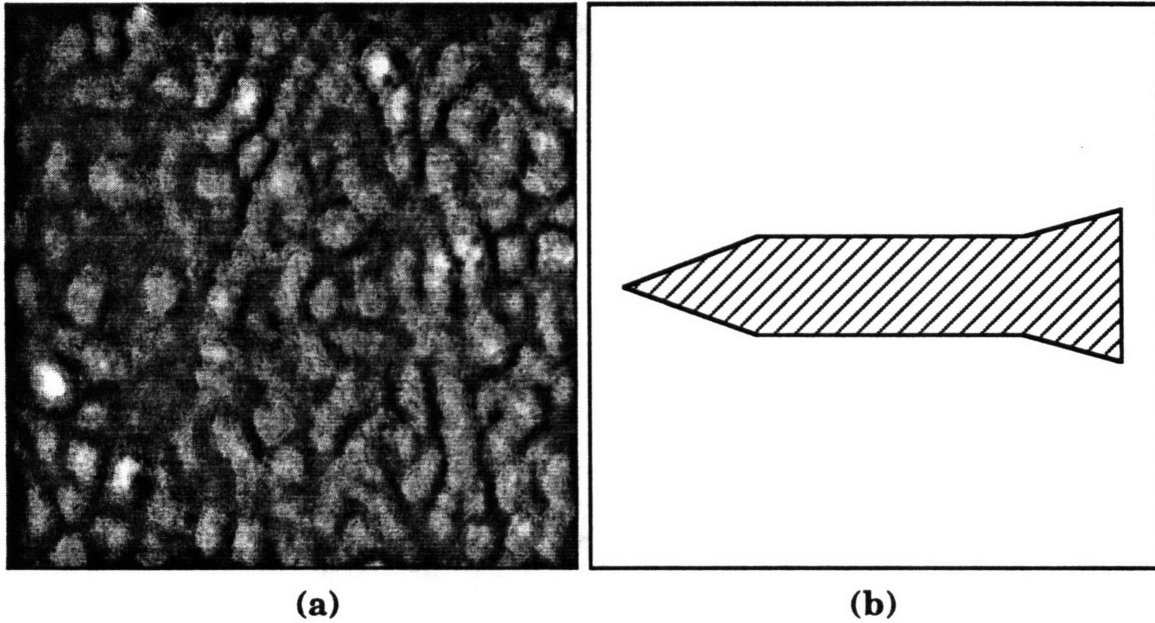


Figure 4.1: Speckle Pattern from Triconic, Adapted From [2]

It can be shown that the decorrelation frequency, $\Delta\nu_D$, is inversely proportional to the range extent L of the target. For example, let the step target in Figure 4.2 below be illuminated on axis with a tunable laser. In order to calculate the reflected beam intensity at a point on a distant detector located on axis, the contributions scattered back to the detector from all points on the surface of the steps are summed. A phase delay, ϕ , is associated with the path length from each scattering point. Let us temporarily consider only the contributions from two range values, from planes of values 0 and z . If ν is the laser frequency, λ is the laser wavelength and c is the speed of light, then the phase delay associated with the round trip path $2z$ between the two planes is expressed in the following relation [2]:

$$\phi = -\frac{(2\pi)(2z)}{\lambda} = -\frac{4\pi z\nu}{c} \quad (4.1)$$

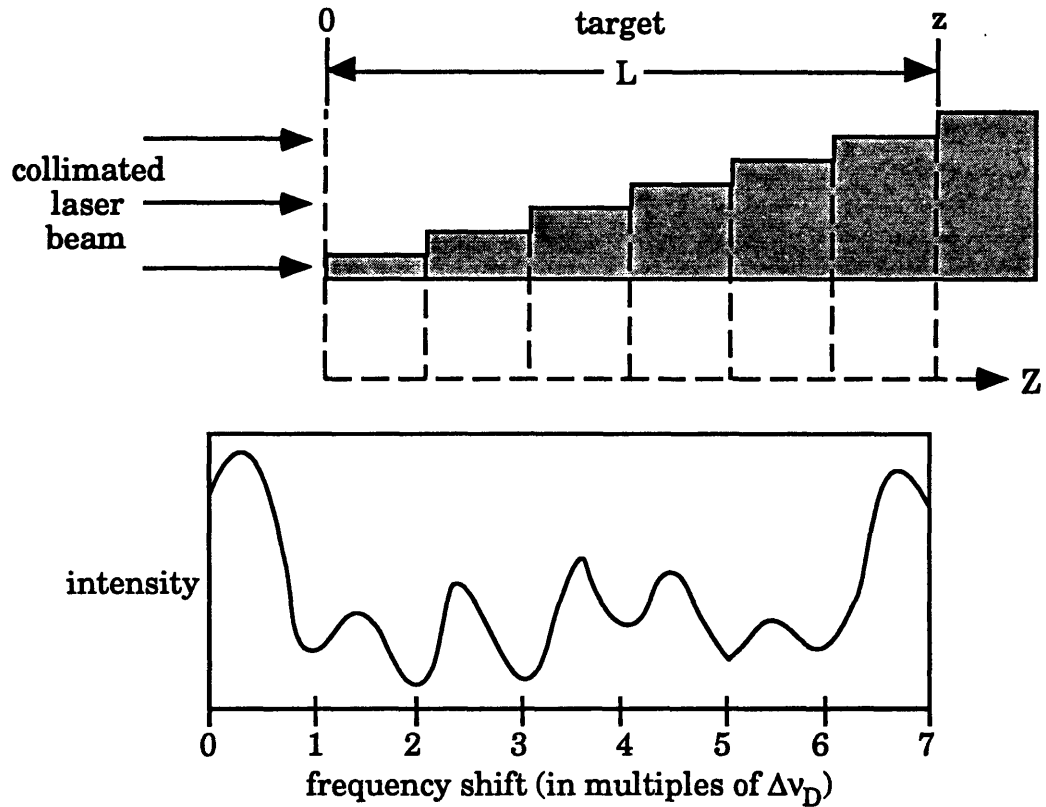


Figure 4.2: Step Target Speckle Intensity Variation, Adapted From [2]

Depending upon the value of ϕ , there is either constructive or destructive interference between these two planes at the detector for a particular laser frequency. As the frequency of the laser changes, it is this relationship which causes the intensity at different points in the backscattered beam to vary periodically. It can be easily seen from Equation 4.1 that the phase difference between the light reflected back from two points is directly proportional to the range distance between them. For a given frequency shift, a large phase shift means that the intensity at a particular point on the detector oscillates between light and dark more quickly. Therefore, the highest frequency component of the intensity oscillation of a speckle pattern is due to the interference between the parts of the target which are furthest apart in range,

the opposite ends of the part, at range values 0 and L . For an object of range extent L , the value of the decorrelation frequency, $\Delta\nu_D$, the highest frequency component of the intensity oscillation, can be determined by solving Equation 4.1 for ν , using a range extent of L and a phase shift of one complete cycle, 2π . The resulting relation is shown below in Equation 4.2:

$$\Delta\nu_D = \frac{c}{2L} \quad (4.2)$$

We can see from Equation 4.2 that the frequency shift necessary to produce a single cycle intensity oscillation for the highest frequency component is inversely related to the range extent of the object. Therefore, the speckle pattern generated from an object of large range extent will seem to “boil” at a faster rate for a given frequency shift than one of smaller range extent because higher frequency components are present in the speckle pattern of the larger range extent object.

Because the wavelength decorrelation frequency is the highest intensity oscillation present in the speckle pattern when the laser is tuned, we only need to tune the laser at a step size small enough to satisfy the Nyquist criterion to sample this maximum frequency component. Thus, the frequency tuning step size, $\Delta\nu_{step}$, must be less than half the size of the decorrelation frequency, as shown below in Equation 4.3:

$$\Delta\nu_{step} \leq \frac{\Delta\nu_D}{2} = \frac{c}{4L} \quad (4.3)$$

It can clearly be seen from the plot in Figure 4.2 that there are lower frequency components in the intensity variation than the decorrelation frequency. If only points at the opposite ends of the target were scattering light, the speckle intensity would have gone through a complete constructive and destructive interference cycle as the frequency was tuned by the decorrelation frequency, $\Delta\nu_D$. However, since there are scattering points which are closer together than the ends of the target, it can be seen from Equation 4.1 that the laser must be tuned further for the interference pattern due to

these closer points to vary through one complete cycle. This behavior is what determines the range resolution of the laser speckle technique.

In order to resolve points close together in range, we must tune the laser wavelength far enough to sample the lower frequency intensity variation components. This is done by tuning the laser in steps equal to the step size determined in Equation 4.3. We keep tuning and taking pictures of the speckle pattern imaged on the detector every $\Delta\nu_{\text{step}}$ until we have tuned far enough to sample the larger wavelength components necessary for a desired range resolution, Δz . Each time we increase the length of the frequency scan by one frequency decorrelation unit $\Delta\nu_D$, we can pick up frequency components due to points as close together as L/N , where N is the number of frequency decorrelation units tuned. The range resolution can be determined by rearranging Equation 4.2 and dividing both sides by N . If Δz is the range resolution L/N , and B is the total scan length $N\Delta\nu_D$, then the range resolution can be determined via the following expression:

$$\frac{L}{N} = \frac{c}{2N\Delta\nu_D}, \quad \Delta z = \frac{c}{2B} \quad (4.4)$$

It is evident from Equation 4.4 that the further the total distance that the laser is tuned during data acquisition, the better the range resolution becomes. Therefore, for a diffuse target, the range resolution is only theoretically limited by the tunable range of the laser and the ability to tune in equal steps. For a more detailed theoretical background and analysis of wavelength decorrelation, see Shirley et. al. [2].

4.3 System Design

4.3.1 Laser Speckle System Design

Figure 4.3 shows a diagram of the laser speckle system setup at Lincoln Laboratory which I used to perform the experiments for this work. Figure 4.4 is a photograph of the laboratory setup.

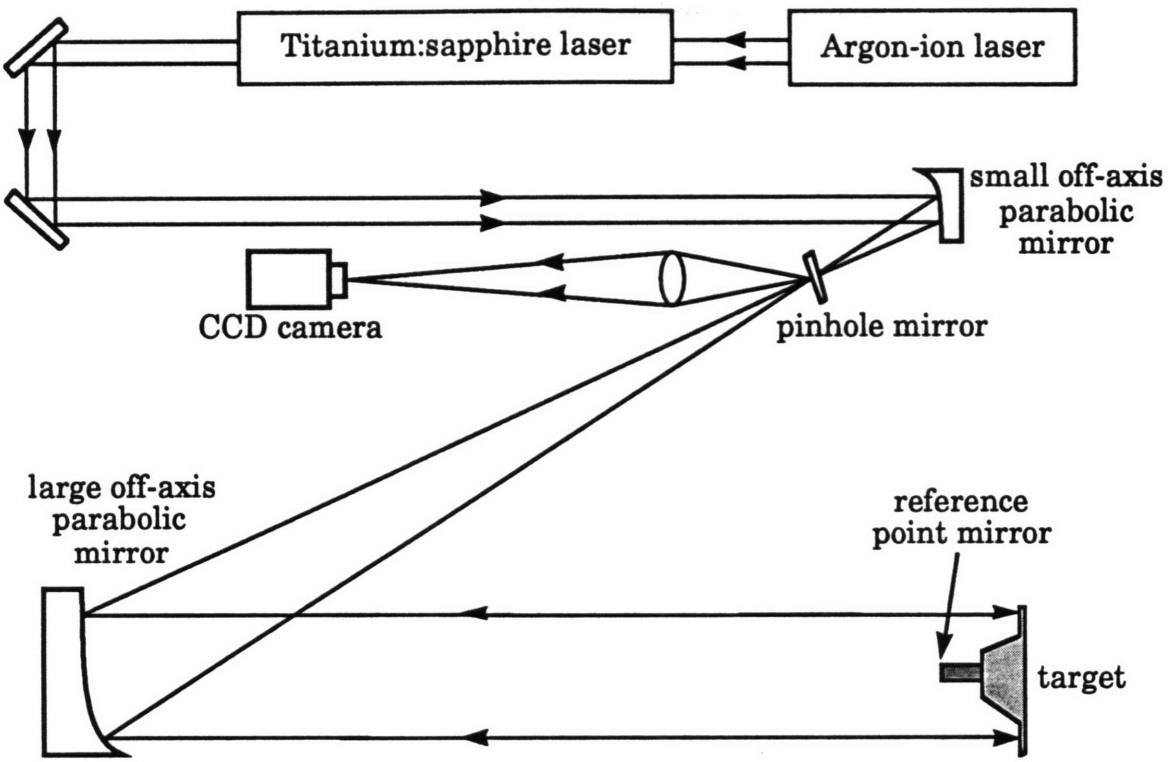


Figure 4.3: Laser Speckle System Diagram, Adapted From [2]



Figure 4.4: Laser Speckle System Setup

A Coherent, Inc. Model 899 tunable Ti:sapphire ring laser is used to provide the light source. The laser is pumped by a Coherent, Inc. Innova 200 argon-ion laser. The Ti:sapphire is an actively stabilized single-frequency ring laser. It is a continuously tunable, solid state laser operating at wavelengths in the range between 690 nm and 1100 nm. The maximum output power is 2.5 W continuous wave, and it can produce a coherence length greater than 100 m, which is adequate for this system because it is much larger than the range extent of the targets to be measured. Since the wavelength decorrelation technique is implemented by using direct detection of the speckle intensity, only the range extent of the target must be smaller than the coherence length. The distance to the target may be much larger than the coherence length, which gives the technique an advantage measuring distant targets.

The Ti:sapphire laser can be scanned continuously over a frequency range of 30 GHz. When the laser reaches the end of the 30 GHz range, the laser can be stepped by a computer to the next 30 GHz section, using an internal wavemeter for feedback. In this mode, the laser can be stepped over a range of 10 THz, yielding a maximum range resolution of 15 μm based on Equation 4.4. Computer stepping of the laser, however, is time consuming because the computer must wait for feedback from the wavemeter each step it takes towards a target frequency, and this causes a 256 frame experiment to take about an hour to run.

When the beam exits the Ti:sapphire laser, a small percentage of the beam is deflected into a power meter to measure any fluctuations in the laser power during a scan. The laser power information is used during processing to cancel the influence of power fluctuations in the intensities in the speckle patterns. The laser is then deflected off of two mirrors onto a small off-axis parabolic mirror. This mirror sends the beam through a pinhole mirror and expands it until it strikes a large off-axis parabolic mirror which serves to collimate the beam and send it towards the target, simulating a far-field condition.

After striking the target, the backscattered light is reflected back onto the large off-axis parabolic mirror onto a mirror with a small pinhole in it, through

which the original beam passed. A lens then serves to focus the speckle pattern onto the detector. A Photometrics Ltd. 512 by 512 pixel scientific grade CCD camera is used as the detector for the system. Each pixel measures 27 μm by 27 μm . Both the focusing lens and the CCD camera are mounted on a ruled track. They can be slid into appropriate positions for magnification or reduction of the speckle pattern.

A program written in the Labview programming environment was run on a Macintosh Quadra 950 computer. The program was responsible for timing the taking of pictures with the CCD, receiving the CCD images, receiving the power meter data, and signaling the IBM compatible computer which tuned the frequency of the laser.

4.3.2 Using the New Focus Laser

The large size and slow tuning of the Ti:sapphire laser makes it a poor choice for inclusion of a portable sensor using the laser speckle technique. However, an external cavity tunable diode laser may be a good solution. The New Focus, Inc. 6124 laser, pictured in Figure 4.5, is continuously tunable between 760 nm and 790 nm at a maximum power of 50 mW. Its small size (130 mm by 90 mm by 80 mm) and its light weight (a few kg) make it a possibility for use in a portable laser speckle system in place of the Ti:sapphire ring laser. The wavelength is tuned with a PM500 linear actuator, not purchased with the laser, also shown below in Figure 4.5, which is controlled via computer. For this work, a Macintosh Quadra 950 was used, and a program written in the Labview environment was used to instruct the PM500.

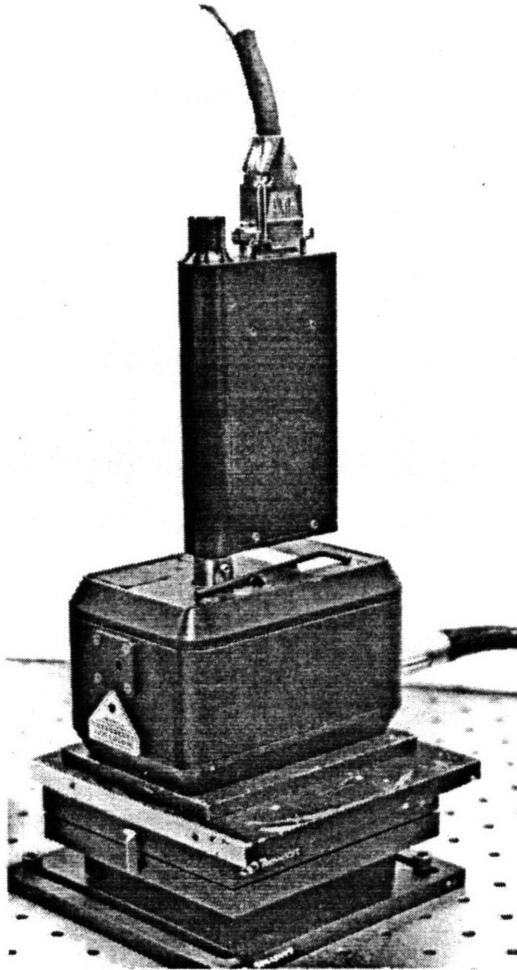


Figure 4.5: The New Focus External Cavity Tunable Diode Laser

4.4 Image Processing

4.4.1 Perform a Three-Dimensional Fourier Transform

Once the data is collected for a target, the next step is to attempt to extract three-dimensional range information. The raw data is in the form of a three-dimensional array. For this work, the x and y dimensions of this array are 256 because I used a 256 by 256 pixel area of the CCD array to take data. The z dimension is the number of frames which were captured by the CCD array. In this work, I took either 128 or 256 frames. As mentioned in Section 4.2.1, the range resolution obtained improves if the scanning bandwidth is larger, i.e. if more frames of data are taken at a fixed frequency interval apart.

The x and y coordinates of the array points correspond to x,y pixel positions on the CCD array, while the z coordinate is an integer multiple of the frequency step size. The three-dimensional array produced will look something like that depicted in Figure 4.6.

The first step in the image processing is to normalize the three-dimensional array with respect to laser power variations during the experimental run. The output from the power meter was stored in a one dimensional array; one reading was taken for each CCD picture. The power value for each CCD picture is multiplied by the intensity value in the respective two dimensional array.

As discussed in Section 4.2.1, the interferometric speckle pattern produced contains range information about the part. The amplitude of the various frequency components of the three-dimensional array hold this range information. Thus, the next step in the image processing is to take a three-dimensional Fourier transform of the three-dimensional speckle array. This will move us from the frequency domain to the spatial domain, where we can proceed to extract an image.

The image processing for this work was done by programs I wrote in PV Wave, a mathematical analysis package, on a Sun Sparcstation 2. For more detailed information concerning the theory behind the image processing steps, see [75].

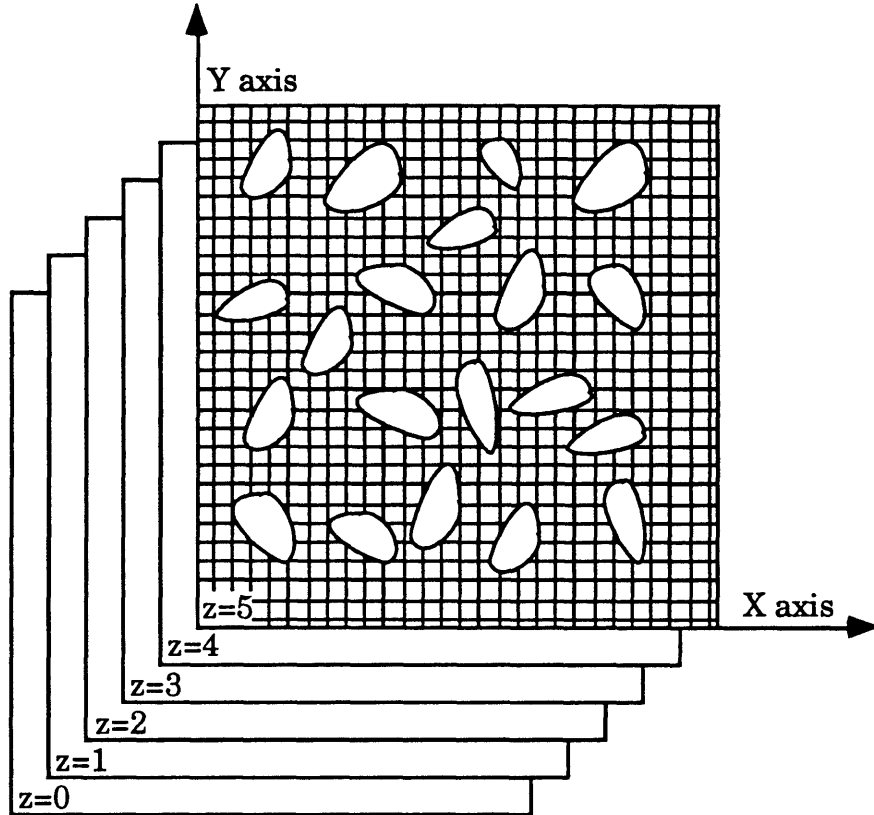


Figure 4.6: Three-Dimensional Laser Speckle Array

4.4.2 Extract Target Image from a Three-Dimensional Array

Once the three-dimensional Fourier transform is performed, a three-dimensional array similar to the one depicted below in Figure 4.7 is obtained (Figure 4.7 is a two-dimensional slice of this three-dimensional array for purposes of clarity). Because of the use of a reference mirror attached to the target, which will be discussed later in Chapter 5, the three-dimensional array contains a three-dimensional image of the target, a mirror image of that target, and the autocorrelation of the image.

The three-dimensional array is an array of intensity values. The highest intensity value for each x,y will be located in the z plane which is related to the range of the part at that point. As discussed in Section 4.2.1, the range resolution can be expressed as $c/2B$, so this number can be multiplied by the number of a particular z plane to translate the frame numbers into range values.

To find the maximum intensity plane for each x,y coordinate, I wrote a simple algorithm which scans through the z planes for each x,y , placing the number of the z plane which contains the maximum value in a two dimensional array at the same x,y coordinates. This resultant two dimensional array is then multiplied by the range resolution to convert the planes to range values. This new array contains the x,y,z data for the part, and the part can then be seen via any of several plotting programs. For more detailed information concerning the theory behind the extraction of the image, see [75].

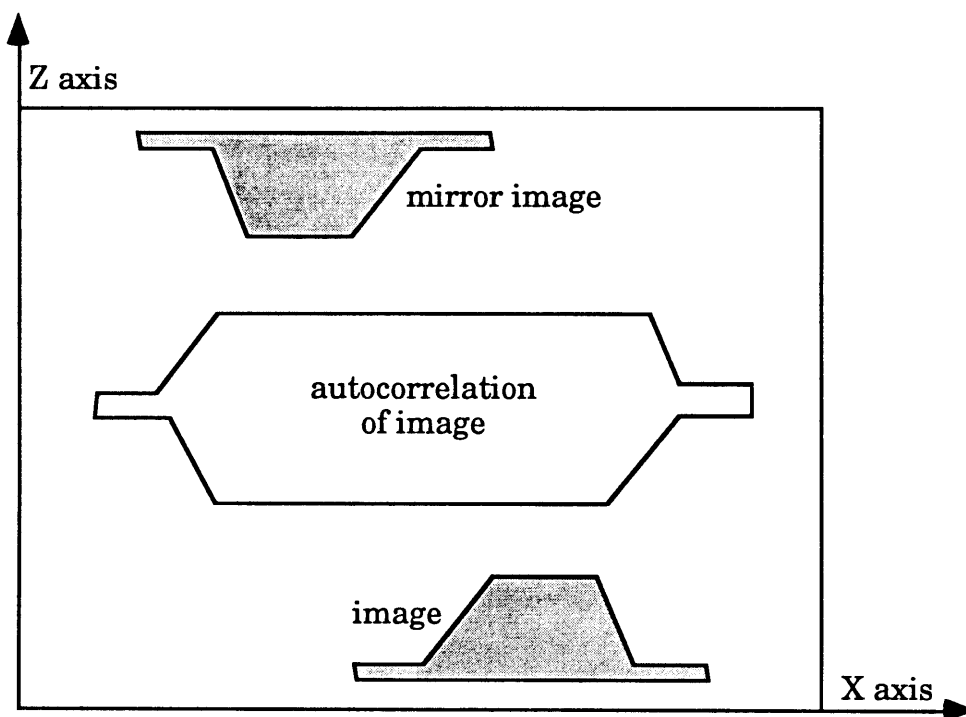


Figure 4.7: Extracting an Image

4.4.3 Data Filtering

Usually the data contains some level of noise. This can be a result of non ideal ambient conditions during the experimental run, inconsistent surface reflectivity of a target, or other reasons. After the two dimensional array containing x,y,z values for the target is extracted and plotted, there are two simple ways to filter the data.

The most basic filter is a mean filter. This algorithm calculates the mean of a square of n points centered on a point x,y , and it reassigns the value of x,y as the mean of the n points. The linear dimension n which determines the averaging region is usually referred to as the “neighborhood” over which the filter acts. The main disadvantage associated with the use of a mean filter is that the edges of a target will become rounded because the points on the upper edge will be averaged with points at the lower edge. This can be a problem if there are sharp edges in a part, but if there are no sharp edges, as in many sheet metal parts, mean filtering can be useful for smoothing out high frequency noise in an image.

Another useful filter is a median filter. This algorithm takes the median value of a square (neighborhood) of n points centered on a point x,y , and it reassigns the value of x,y as this median value. The best thing about a median filter is that part edges are preserved. Since there is no averaging, there is no smoothing over an edge. This is computationally as easy to implement as a mean filter, but it can be used on a wider range of parts. However, median filters do not preserve sharp corners. In the case of a ninety degree corner, the area over which the corner is averaged contains more points on the lower plane than the upper plane, so the corner is rounded.

There are many better and more complex image filtering techniques available, and for more detailed information concerning this, a useful image processing text is [76]. However, since this work concerns the measurement of a sheet metal part, the edges and corners of which not being extremely sharp, I will use primarily mean and median filtering methods.

5

Experimental Design

5.1 The Sheet Metal Part

Since the scope of this thesis concerns three-dimensional measurement techniques for use in manufacturing, I thought it would be most appropriate if a sheet metal part were used to test the laser speckle technique.

Considering the size of the experimental laser speckle setup, I chose to use a six inch square stamped steel sheet metal part, pictured below in Figure 5.1. This piece is a convenient one because there are several different surface slopes available in one part. Each side of the raised center section slopes down at a different angle. The steel die used to make the part is pictured below in Figure 5.2. The part was designed by Walczyk [77] for his work on flexible sheet metal forming methods.

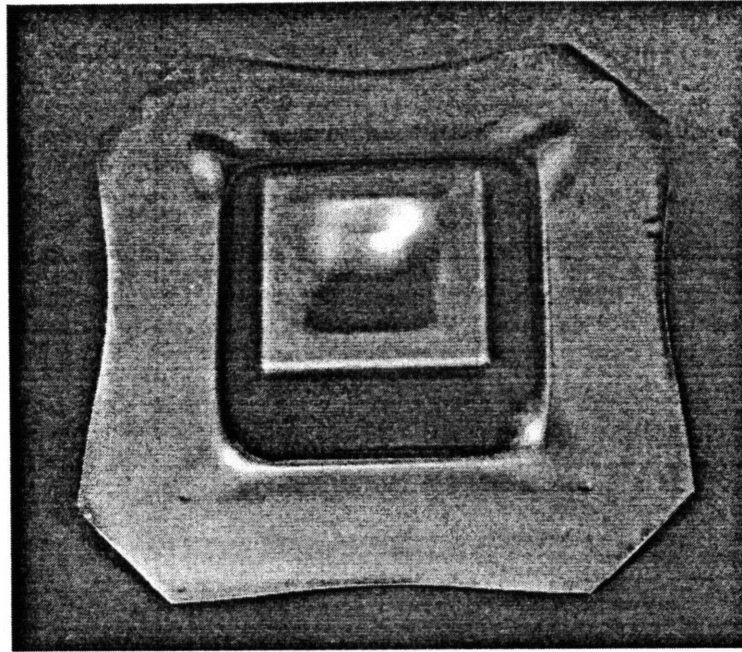


Figure 5.1: The Sheet Metal Part Used for This Work

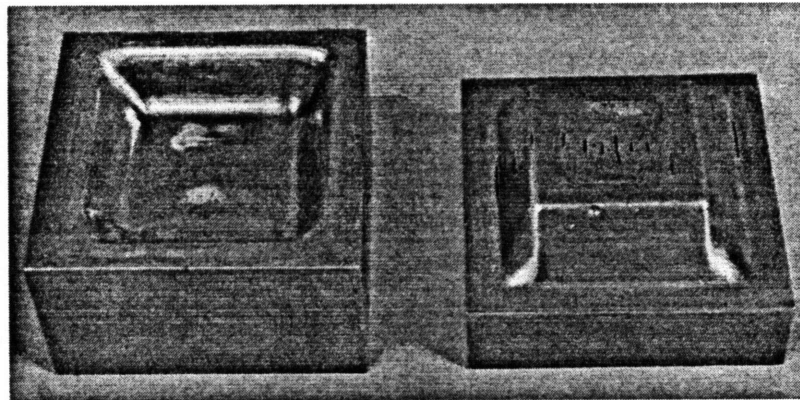


Figure 5.2: The Die Which Made the Sheet Metal Part

5.2 Design of a Repeatable Mounting Fixture

After selecting and stamping a sheet metal part to use in experiments, the next step was to design a repeatable mounting fixture. In order to more easily compare laser speckle experiments under different conditions to each other, a repeatable fixture would be important. I designed a kinematic mount which prevented part motion and was repeatable. The mounting fixture is

shown in Figure 5.3 with the sheet metal part in its kinematic position. The design drawings for the mounting fixture and the clamping piece are presented in Appendix A.

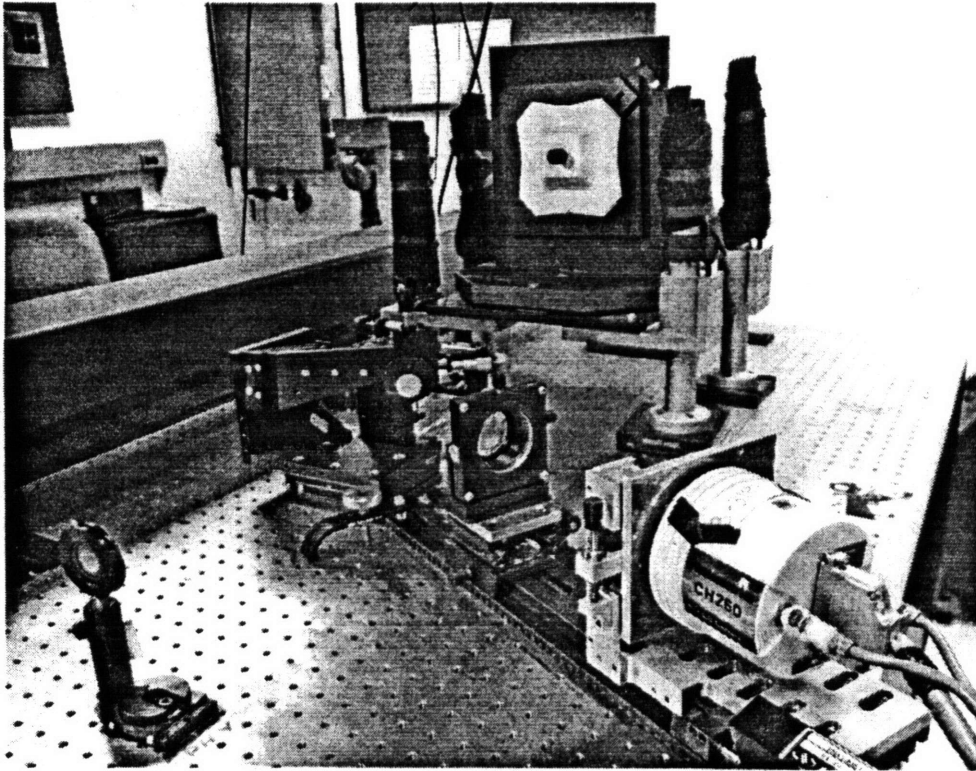


Figure 5.3: Mounting Setup for the Sheet Metal Part

5.3 CMM Measurements

The first experiment to be done was to measure the sheet metal part on the coordinate measuring machine. The measurement was performed on the Brown & Sharpe MicroVal PFX, the specifications and design of which was discussed in detail in Chapter 2. The part was painted with a thin coat of diffuse white paint which would be used later in laser speckle experiments, and a cylindrical aluminum mounting piece was epoxied to the center of the part to accommodate a reference mirror in future laser speckle experiments. The part was prepared in this way to provide the best evaluation of the laser speckle

technique by varying the part as little as possible between the two measurement systems.

A Renishaw touch trigger probe was used with a stylus tip which was 25 mm in length with a 2 mm diameter ruby ball tip. This stylus tip was the longest to which I had access, and a long tip was desirable so that the tip could reach the part surface at the base of the reference mirror mount without a problem.

The program Micromasure IV, from Brown & Sharpe, was used to control the CMM during the measurement. The program allowed the user to define the x - y plane, the x and y axes, the scanning density in x and y , and the four corners of the quadrilateral shaped scanning region. I chose to scan over a 110 mm by 110 mm region which was approximately centered on the part. I defined the measurement interval to be 1 mm along both the x and y axes. These parameters provided a 111 point by 111 point measurement, for a total of 12321 data points. The CMM completed the measurement in approximately eight hours.

5.4 Laser Speckle Measurements

5.4.1 Power Distribution Across the Collimated Laser Beam

One of the first experiments that needed to be done was one which determined the power distribution across the laser beam at the point where the collimated beam strikes the target. This information was valuable in interpreting data from laser speckle experiments. In order to measure the power across the beam, I positioned a power meter in the path of the beam at the vertices of a one inch grid, writing down the power reading at each sample point. This would provide 100 data points across the beam, which is good enough to understand the shape of the beam and the intensity distribution across the beam.

5.4.2 Laser Speckle Experimental Trials

To determine the usefulness of the laser-speckle technique as a manufacturing measurement sensor, I decided to test the laser speckle system

with the same sheet metal part under some variations which might occur in a real manufacturing environment.

Up until the time of this work, the Laser Speckle Laboratory at Lincoln Laboratory had tested targets which were usually coated with a diffuse white paint, protected from wind currents with a foam turbulence tent, and protected from vibrations on a vibration isolation table. The sheet metal part was measured by the laser speckle technique under the following conditions:

- coated with a diffuse white paint with a turbulence tent
- coated with a very light coat of diffuse white paint with a turbulence tent
- without any coating with a turbulence tent
- coated with oil with a turbulence tent
- half coated with a diffuse white paint and half without any coating, with a turbulence tent
- coated with a diffuse white paint with a 16 inch diameter oscillating fan blowing across the part and laser beam path
- coated with a diffuse white paint without a turbulence tent and with the laboratory air circulation turned on

A 256 by 256 pixel region was used to image the speckle pattern for each experiment. Assuming a field of view of 110 mm by 110 mm, this would provide for a cross range resolution of 430 μm . Also, 128 frequency steps were taken for all experiments except one, which took 256. According to Equation 4.4, for a step size of 1.8 GHz for 128 steps, this would provide a range resolution of 650.6 μm .

These variations amounted to eight total experiments, one each under the seven aforementioned conditions, and one extra experiment with 256 frequency steps instead of 128.

5.4.3 Determination of Optimal Reference Mirror

In order to separate the target image from the autocorrelation function discussed in Section 4.2, it is necessary to use a reference plane or point. This reference also serves as the $z = 0$ plane for the target. To provide adequate separation of the target image from the autocorrelation function, the reference

must be located at least as far away from any part of the target as the range extent of the target. To provide this reference, I epoxied an aluminum cylinder to the top of the sheet metal part. I had an aluminum sleeve made which would slide over the mirror base, leaving a small section of the mirror exposed through an aperture of 5 mm in the top of the sleeve. The sleeve was painted black to help prevent light from reflecting off of it. The mirror and its mounting mechanism can be seen in Figure 5.4.

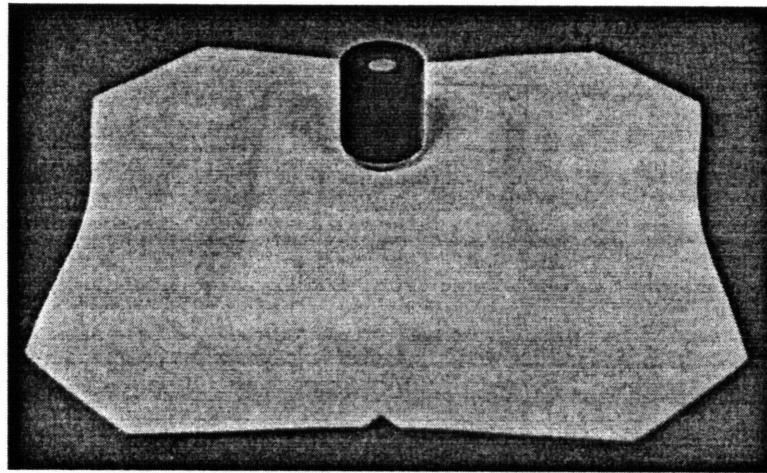


Figure 5.4: Coated Sheet Metal Part with Reference Mirror

It is necessary that the correct focal length reference mirror be chosen for an experiment. If the mirror is too flat, then the amplitude of the light reflected off of it into the detector may be of greater magnitude than the light reflected from the part. If the mirror is too concave or convex, then the light reflected off of it may not make it all the way back to the detector. It is necessary to balance the light returned from the reference mirror with the light returned from the part to make maximum use of the range of brightness values of the CCD array. The light returned from the reference mirror can be adjusted by replacing the mirror with one of longer or shorter focal length.

To determine which mirror was optimal, I placed a mirror on the sheet metal part, took a picture of the speckle pattern reflected back, at a single frequency, and took the two dimensional Fourier transform of the speckle pattern. From this Fourier transform, it can be determined if the reflected light

levels are appropriate. A good mirror will produce a fairly recognizable picture of the target. After testing eight mirrors in this manner, I decided that the best one was a convex mirror, 11 mm thick, 15 mm in diameter, and with a focal length of 0.25 m. The two dimensional Fourier transform from this mirror is shown below in Figure 5.6

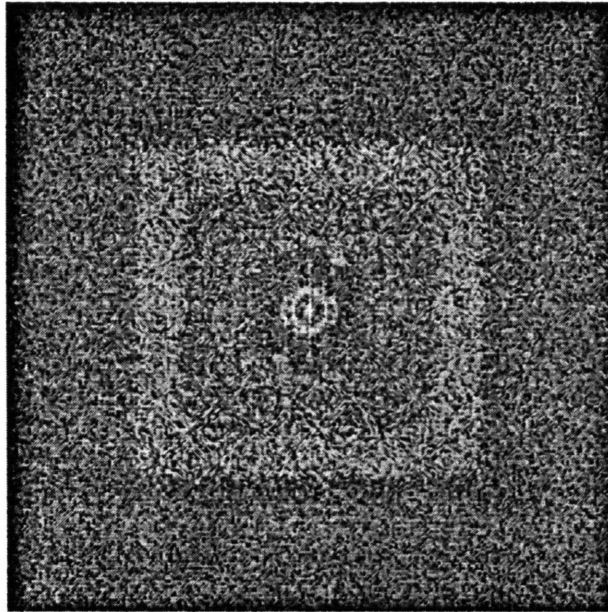


Figure 5.5: Two Dimensional FFT of Coated Part, $R = 0.25$ m

5.5 New Focus Laser Calibration and Characterization

It will eventually be necessary to reduce the physical size of the components of the laser speckle measurement system in order to incorporate the technique into a sensor. Using an external cavity tunable diode laser instead of the Ti:sapphire would help reduce the size and weight of the system tremendously. In order to investigate this possibility, it is necessary to determine the relationship between the laser wavelength and the position of the PM500 linear actuator which is used to tune the wavelength.

The aforementioned relationship was mapped out with the help of a Burleigh Wavemeter, pictured below in Figure 5.6, and several programs which I wrote in the Labview programming environment on an Apple Macintosh

Quadra 950. The computer recorded all of the data and controlled the tuning of the laser for the calibration experiments. The New Focus laser was aimed at the aperture on the right side of the Wavemeter, allowing the wavelength to be determined. The position of the PM500 linear or rotary actuator was recorded, as well as the wavelength of the laser at that position. The actuator was then stepped at a fixed interval, and the next data point was taken. In this manner, the entire lasing region of the New Focus laser was calibrated. Results and analysis of the New Focus laser calibration experiments are presented in Appendix B.



Figure 5.6: Burleigh Wavemeter

6

Results and Discussion

6.1 Presentation of CMM Data

The coordinate measuring machine measured the sheet metal part in about eight hours. The 12321 three-dimensional data points are plotted below in Figure 6.1.

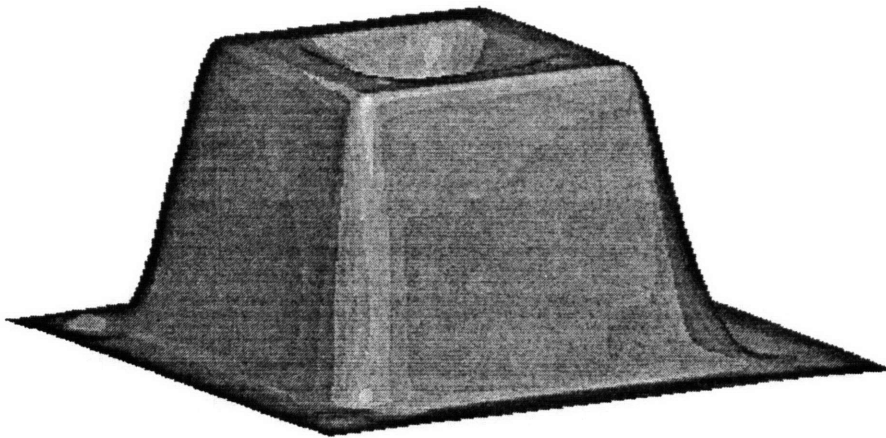


Figure 6.1: CMM Measurement of Sheet Metal Part

6.2 Power Distribution Across the Collimated Laser Beam

Figure 6.2 below shows the results of the experiment I performed in order to determine the power distribution across the Ti:sapphire laser beam at the point when it strikes a target. Notice how the beam is elliptical, and its major axis is at an angle to the horizontal.

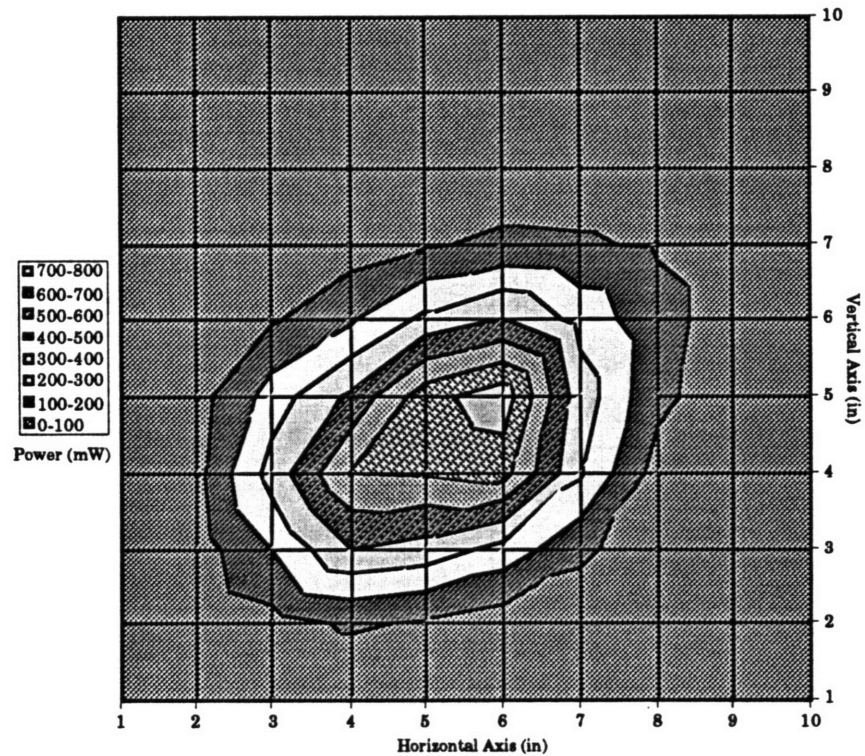


Figure 6.2: Power Distribution of Ti:sapphire Beam

6.3 Presentation of Laser Speckle Data Sets

Figures 6.3 through 6.10 present three-dimensional plots generated from the eight laser speckle experiments. The first experiment to be performed was under ideal ambient and part surface conditions. This consisted of the part being mounted on a vibration isolation table with the laser beam path surrounded by foam walls to prevent air turbulence. Also, the measurement was taken in a dark room, and the part was coated with a diffuse white paint.

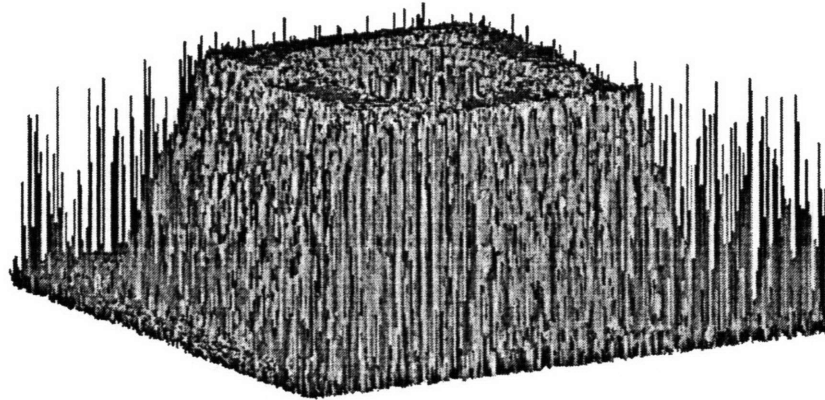
The coat of paint was less than 10 μm thick, but none of the sheet metal surface could be seen through the paint. Also, using Equation 4.3, a 1.9 GHz frequency step was chosen, in order to provide for maximum resolution for the number of steps taken.

The unfiltered data from this experiment is shown below in Figure 6.3 (a). A lot of noise can be seen in the lower ranges of the part, while the higher ranges display less noise. The large amount of noise is most likely due to the large frequency step taken. Strict use of equation 4.3 led me to choose as large of a frequency step as possible because range resolution is directly related to step size. However, as discussed in Section 4.2, the part must be sampled at frequency steps close enough together in order to unambiguously image the the entire range extent and prevent wrapping. The highest frequencies are due to the interference between the ranges of the part which are furthest apart. Since all ranges are determined relative to the reference mirror, the parts of the target farthest away from the reference mirror can cause noise if the frequency step is not large enough.

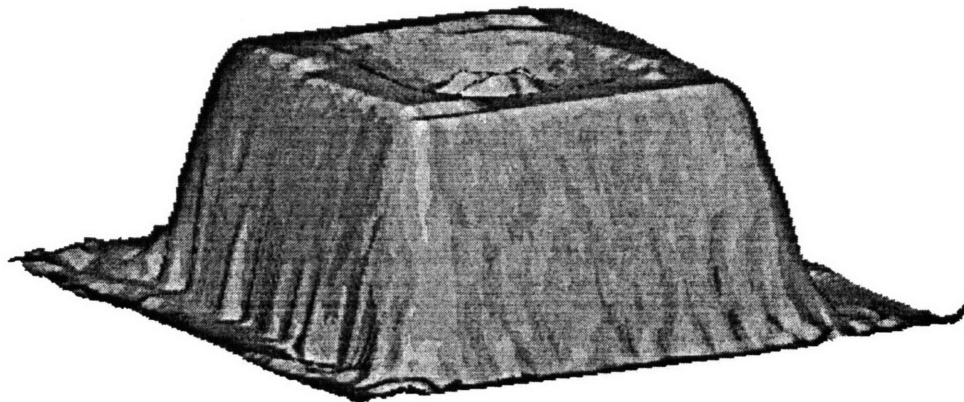
Figure 6.3 (b) shows a filtered image of the same part from Figure 6.3 (a). A median filter with a neighborhood of seven pixels was used in order to eliminate the high spatial frequency noise which is abundant in Figure 6.3 (a) without rounding the edges. After the median filter was applied, a mean filter with a neighborhood of seven pixels was used to help smooth out the lower spatial frequency ripples in sheet metal surface. This image resembles the original target, but there are still many ripples present in the part surface. For this work, I called this filtering level “moderate filtering”

Figure 6.3 (c) shows a more heavily filtered image of the part from Figure 6.3 (a). As in Figure 6.3 (b), a median filter was used, followed by a mean filter. This time, however, a neighborhood of 15 pixels was used for both the median and mean filters. I found that the use of approximately equal neighborhood sizes for the median and mean filters allowed for the best combination of elimination of high frequency noise and low frequency ripples with a minimal amount of edge and corner rounding. For this work, I called this filtering level “heavy filtering”. This amount of filtering produced an image which closely

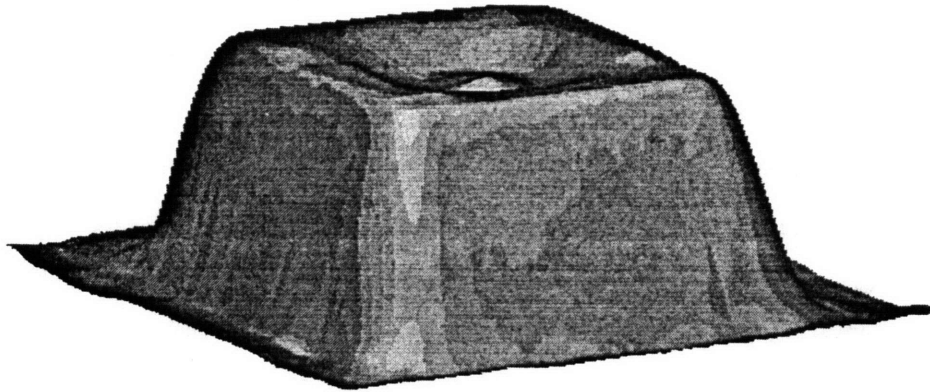
resembles the actual target as well as the image obtained from the CMM shown in Figure 6.1.



(a) no filtering



(b) moderate filtering



(c) heavy filtering

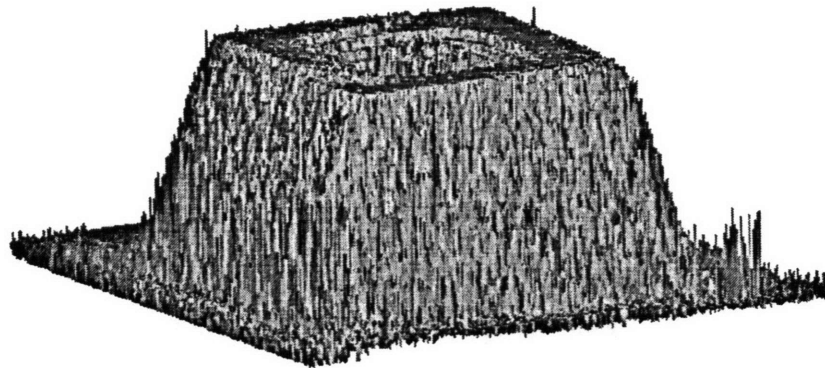
Figure 6.3: Diffuse White Paint, 128 Frames

Figure 6.4 shows images obtained from an experiment which was conducted under the same ambient and part surface conditions as the experiment of Figure 6.3. However, there are two critical differences. 256 frames of data were taken instead of 128, which allows for twice the range resolution, and the laser frequency step size was changed to a more conservative 1.8 GHz, which I had hoped would provide a less noisy image.

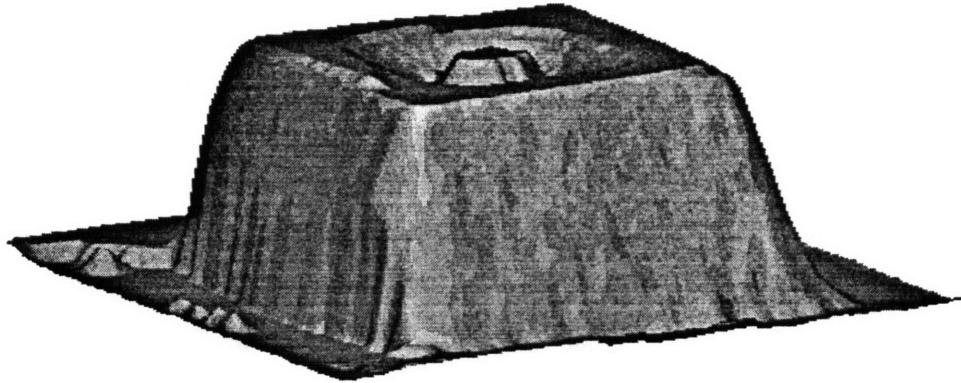
It can be seen in Figure 6.4 (a), that the smaller step size made a large difference in the amount of high-frequency noise present in the unfiltered image. However, the cleaner signal makes one problem more evident. Part of the left side of the target seems to be cut off. The slope changes abruptly about halfway down that side. This behavior can be seen more easily in the “moderately filtered” image shown in Figure 6.4 (b). Upon closer examination, the image in Figure 6.3 also shows this slope drop off on the left side. The most likely explanation for this behavior is the elliptical shaped beam. It can be seen in Figure 6.2 that the rear left side of the part may not be covered well by the beam. If a good light return is not received from that part of the target, surfaces which are not oriented normal to the beam may be missed. Hence, the slope of the target in that area is greater because the return from the

areas normal to the surface in that area are returning more light. Unfortunately, due to the limited power output of the laser I used for this work, this problem of low power at the left and rear of the part persisted in varying degrees through all of the experiments I performed.

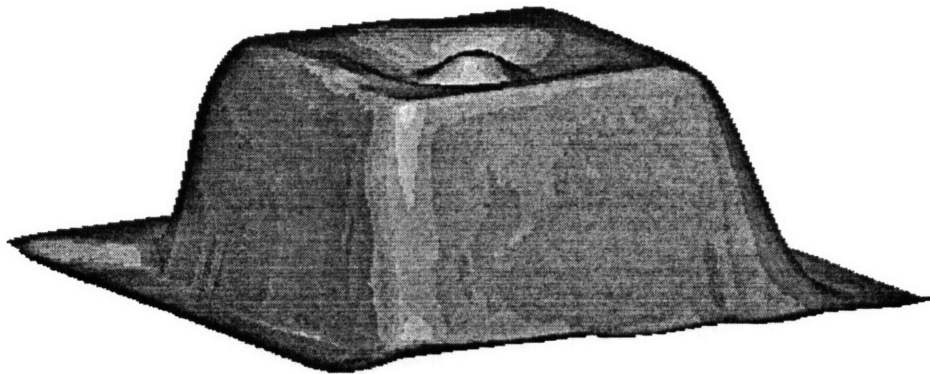
Further filtering of the image, shown in Figure 6.4 (c), helped to reduce the slope from dropping off as quickly on the left side of the part. This image even more closely resembles the actual part than the image in Figure 6.3 (c) because of the higher range resolution. However, closer examination of Figures 6.3 and 6.4 reveals another problem. The part is tilted in a different direction in Figure 6.4 than it is in Figure 6.3. This is most easily seen in Figures 6.3 (b) and 6.4 (b). I was perplexed by this revelation. I designed a kinematic mounting fixture (see Appendix A) to prevent just this problem. The most likely reason for this behavior is that the components of the system are adjusted slightly between runs to allow the laser beam to strike the part approximately centered on the part. Small changes in alignment may contribute to a slight tilting of the image. There may be other reasons for the tilting, but further research is needed to understand them. This problem also persists throughout the experiments. Although image quality is not degraded, quantitative comparison of data points becomes more difficult.



(a) no filtering



(b) moderate filtering



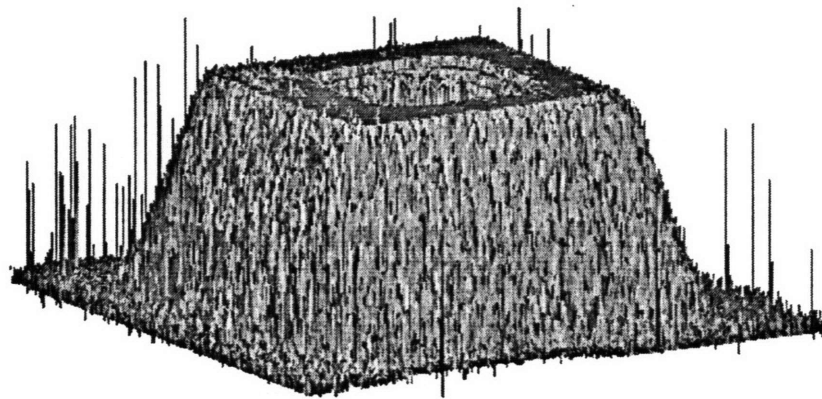
(c) heavy filtering

Figure 6.4: Diffuse White Paint, 256 Frames

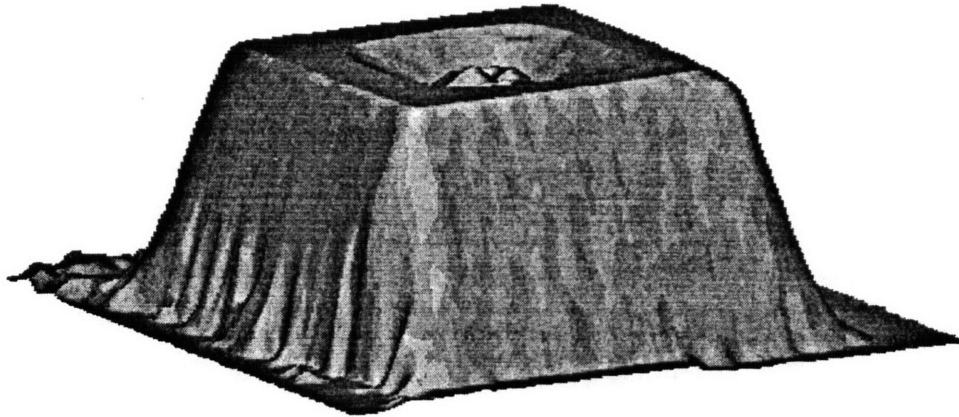
Figure 6.5 presents images obtained from an experiment which was slightly varied from the previous two. The ambient conditions used were the same, but the part was coated with a single spray of the white diffuse paint instead of a full coat. The sheet metal surface could easily be seen through the

paint, but just enough paint was applied to cut down on the reflectivity of the bare sheet metal surface. Figure 6.5 (a) shows the resulting unfiltered image. It can be seen that there is less high frequency noise than in Figure 6.3 (a), but there is more than in Figure 6.4 (a). This could be expected as a result of increased reflection of light from the surfaces normal to the laser beam because of the thinner coat, resulting in a slight glare, increasing the noise level across the target.

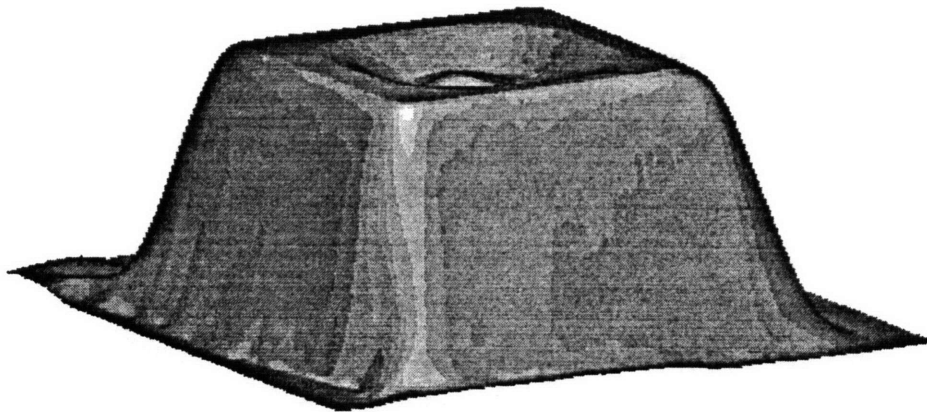
Moderate filtering of the image produced Figure 6.5 (b). This image is visually nicer than the previous two moderately filtered images because the reference mirror happens to be oriented almost precisely along the axis of the beam. However, the left side is still affected by the limited beam power in a similar manner as seen in Figures 6.3 and 6.4. The heavily filtered image in Figure 6.5 (c) is very similar to the actual part. The filtering helped clean up the left side of the part. In my opinion, this was the nicest image I obtained during the eight experiments, so I used it for quantitative comparison to the CMM data, which is discussed below in Section 6.4.



(a) no filtering



(b) moderate filtering



(c) heavy filtering

Figure 6.5: Light Coat of Diffuse White Paint, 128 Frames

In the next experiment, the ambient conditions were held constant, but the surface finish was changed once again. Figure 6.6 shows images produced by measurements of the bare sheet metal part. The effect can clearly be seen in the unfiltered image of Figure 6.6 (a). As might have been expected, the bare metal surfaces normal to the beam returned large amounts of light relative to

the surfaces not normal to the beam. The normal surfaces produce a glare which overpowers the return from the other surfaces. Notice that the noise level is highest on surfaces not normal to the laser beam. In fact, the image seems to only show two range levels — those of the two normal surfaces of the part.

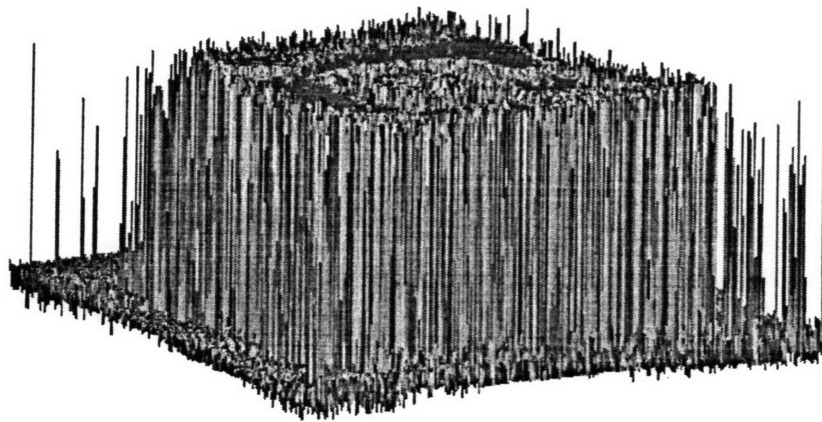
Figure 6.6 (b) further confirms this behavior. Notice how the side walls of the part slope down almost vertically, much more steep than those in Figures 6.3 - 6.5. This, along with the behavior along the left side of the part in the previous images, helps confirm the behavior which results when little light is returned from part of the target relative to the rest of the target. The areas returning more light produce a glare and work to prevent the obtaining of range information from the areas which are not as reflective.

Fortunately, there is a way around this problem in the case of a highly reflective part. There is still information held in the three-dimensional Fourier transform, but it is not being extracted properly by simply searching for the range level which returns the most light. Figure 6.6 (c) shows the result of a filtering method I tried which incorporates some prior knowledge of the shape of the part. Using the nice image from Figure 6.5 (c), I searched for the range which returns the most light, but only within plus or minus three range positions from the part information from Figure 6.5 (c). Since the range resolution when taking 128 frames at a step size of 1.8 GHz is about 650 μm , plus or minus 3 range steps gives us a range of about 4 mm inside which we look for the part surface. This helps a great deal over most of the surface of the part, because we know that the part surface is not going to vary that much from trial to trial. In this way, we can avoid the sections of the Fourier transform which are dominated by the glare from the normal surfaces.

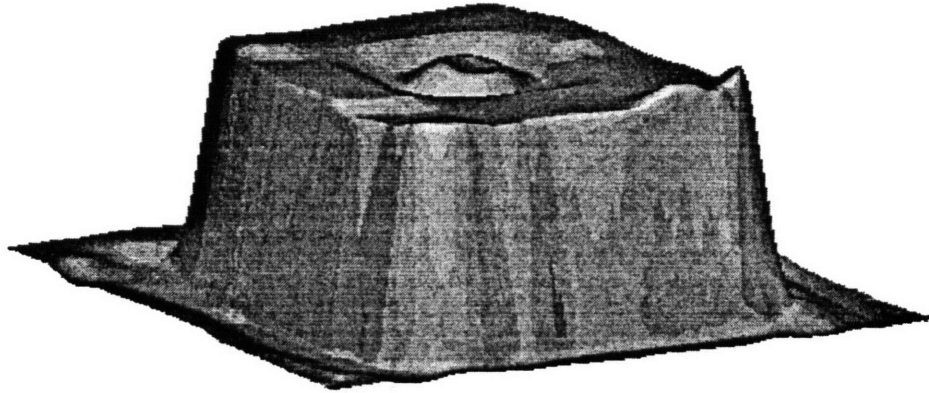
One problem with this filtering method, however, is that when we are within a few millimeters of the normal surfaces, the glare from those surfaces once again dominates the region in which we are looking for the surface. A careful perusal of Figure 6.6 (c) reveals that the slope of the side walls of the part increases at points near the top and bottom of the walls where the glare dominates. In the center of the wall, however, this is not a problem, and the

slope in these areas more closely matches that of the actual part. In this work, I called this filtering scheme “special filtering”.

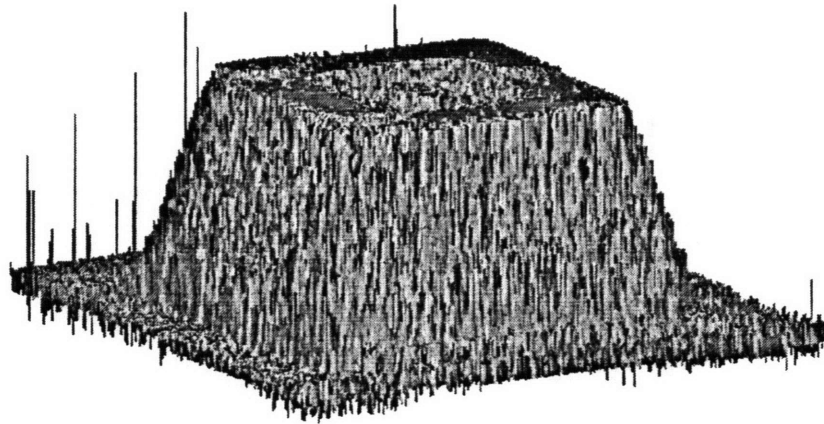
Figure 6.6 (d) is surprisingly clean. Although the “special filtering” scheme does not perform well at the areas of the side walls near the normal surfaces, heavy filtering takes care of those areas. Since the normal surfaces and the middle regions of the walls in Figure 6.6 (c) are similar to the actual part, the slopes of the other surfaces are blended between the slope of the walls and the normal surfaces. Since this sheet metal part has smoothly varying surface slopes, the resulting image is very similar to the actual part. In this work, I called this filtering scheme “heavy special filtering”, which consisted of first performing “special filtering” and then using a median and mean filter with neighborhoods of 15 pixels each.



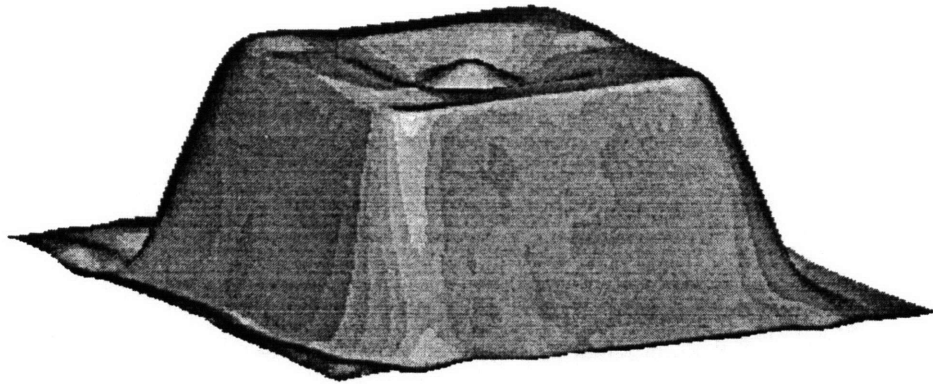
(a) no filtering



(b) heavy filtering



(c) special filtering

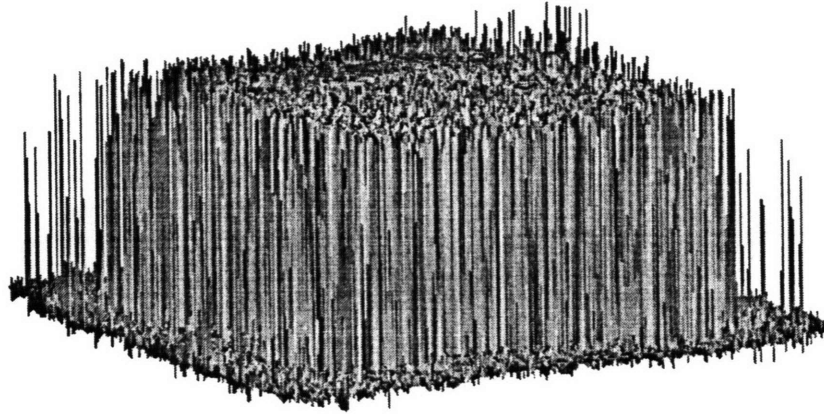


(d) heavy special filtering

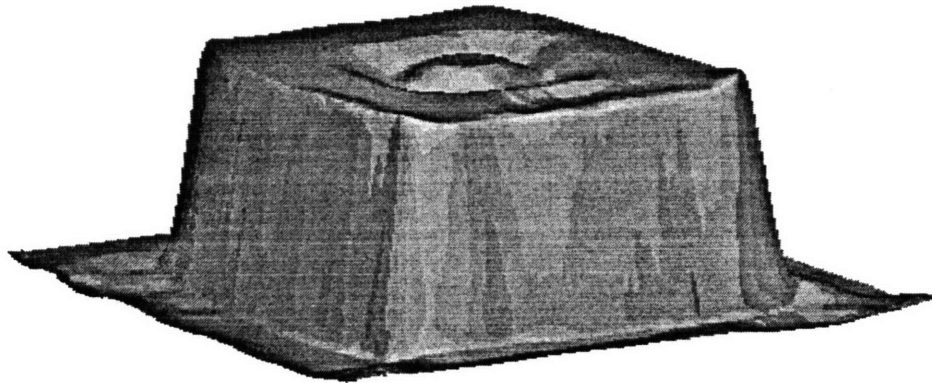
Figure 6.6: No Coating, 128 Frames

Images produced from the next experiment are shown below in Figure 6.7. In this experiment, the ambient conditions were once again constant, but the surface was coated with only a machining oil. The data from this experiment produced results similar to those in Figure 6.6. The addition of a liquid medium to an already reflective surface served to even further increase the effects of the glare. Figure 6.7 (a) looks even more noisy than its counterpart in Figure 6.6 (a), and the slope of the walls in Figure 6.7 (b) is even greater than that in Figure 6.6 (b), indicating a stronger light return from the surfaces normal to the beam relative to the other surfaces than that resulting from a bare sheet metal surface alone.

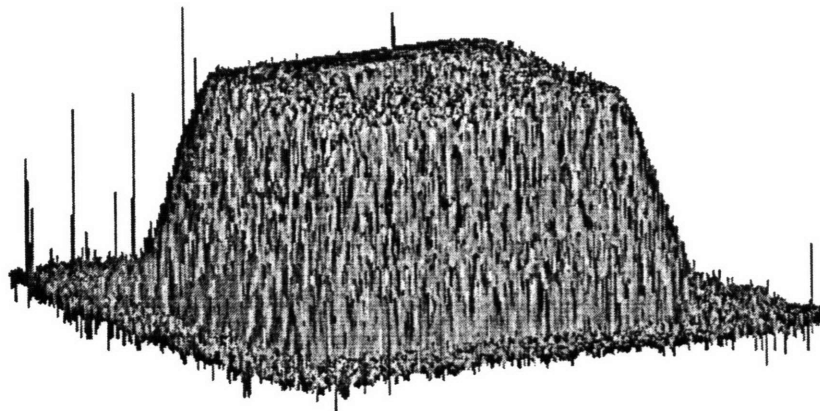
Once again, however, “special filtering” manages to extract most of the range information from the three-dimensional Fourier transform. Although the image in Figure 6.7 (c) has more high frequency noise on its normal surfaces than the image in Figure 6.6 (c), the “heavy special filtering” manages to produce a cleaner image in Figure 6.7 (d) than that which was obtained in Figure 6.6 (d). Part of the reason for this, however, could be that the coordinate axes of the image were aligned more along the axis of the laser beam in Figure 6.7 than in Figure 6.6.



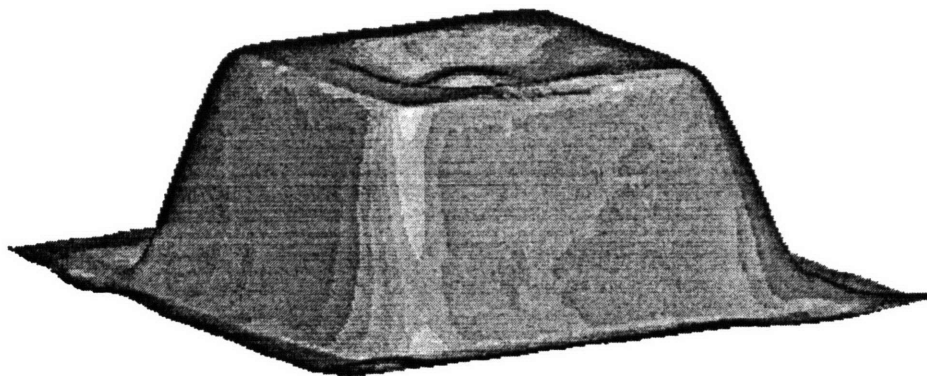
(a) no filtering



(b) heavy filtering



(c) special filtering



(d) heavy special filtering

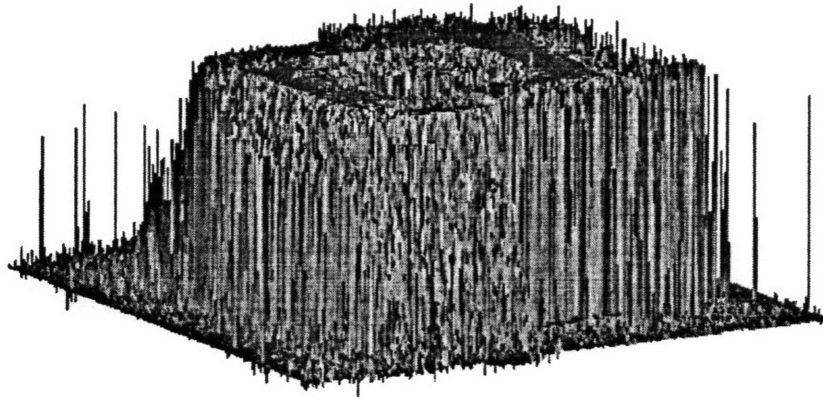
Figure 6.7: Coated with Machining Oil, 128 Frames

The next experiment was done to determine the ability of the laser speckle technique to measure a part with a heterogeneous surface finish. The images in Figure 6.7 were obtained from an experiment done once again with the same ambient conditions but this time, the left half of the part was fully coated with diffuse white paint. As might be expected, this produced results which were a

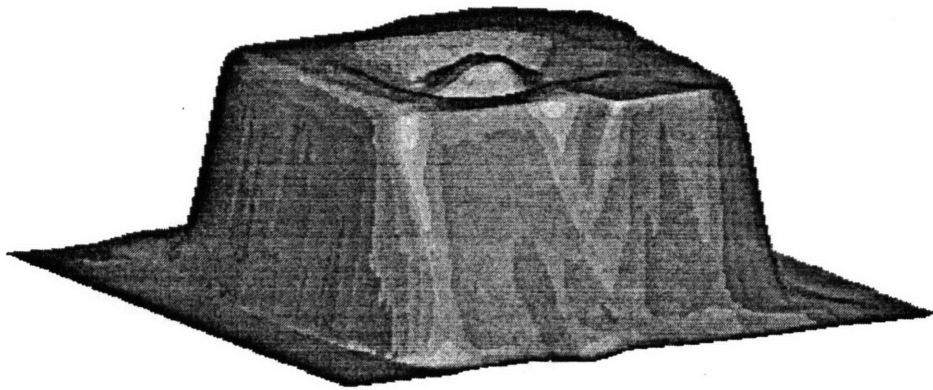
combination of those obtained in Figures 6.4 and 6.6. As can be seen from the unfiltered image in Figure 6.8 (a), the left side of the image shows less high frequency noise than the right. However, instead of being as clean as the unfiltered image in Figure 6.4 (a), the left side of Figure 6.8 (a) is more noisy, most likely because of the large amount of light returned from the uncoated side of the part. Since there is comparatively less light returning from the left side of the part, a higher noise level could be expected. The right side of the image looks very similar to the unfiltered image in Figure 6.6 (a) for the same reasons discussed earlier.

The contrast between the two sides is further highlighted in the heavily filtered image in Figure 6.8 (b). The difference in the slope of the front wall of the part is abrupt at the center. It is also interesting to note that the left wall of the part is of very high slope, most likely because relatively little light was returned from the left wall relative to the right side of the part.

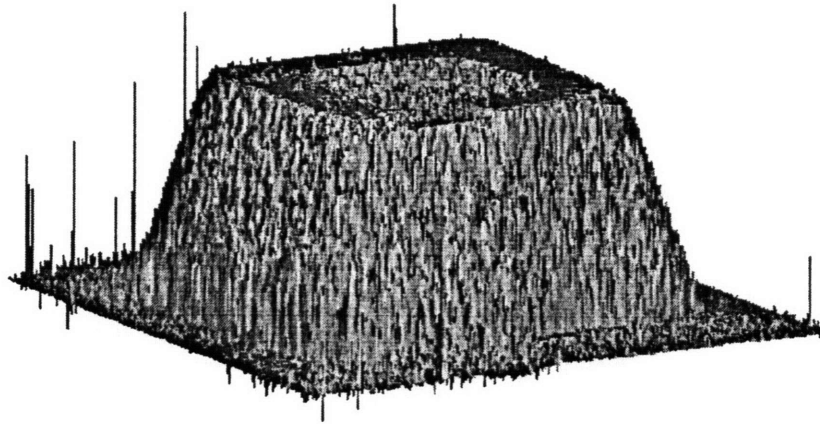
As before, "special filtering" manages to extract more range information from the Fourier transform. The image in Figure 6.8 (c) is not unlike the other unfiltered images shown above. Also, the image in Figure 6.8 (d) looks very clean. However, notice that the front edge of the top of the left side of the part is depressed a bit. I can not fully explain the reason for this. It is most likely a result of the different levels of light returned from the left and right side of the part.



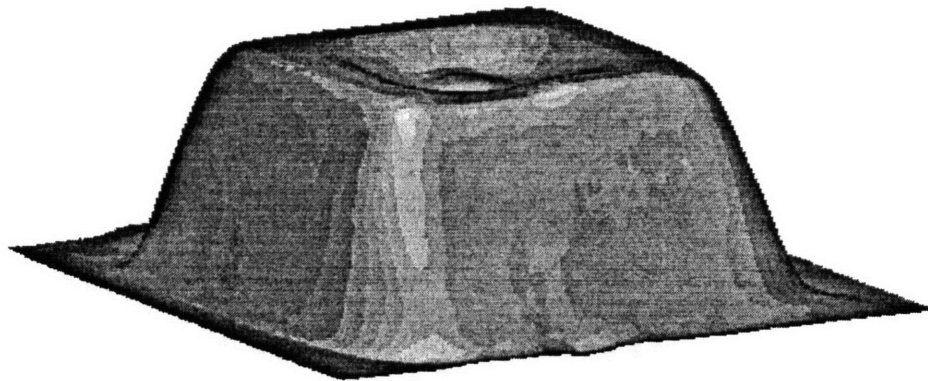
(a) no filtering



(b) heavy filtering



(c) special filtering



(d) heavy special filtering

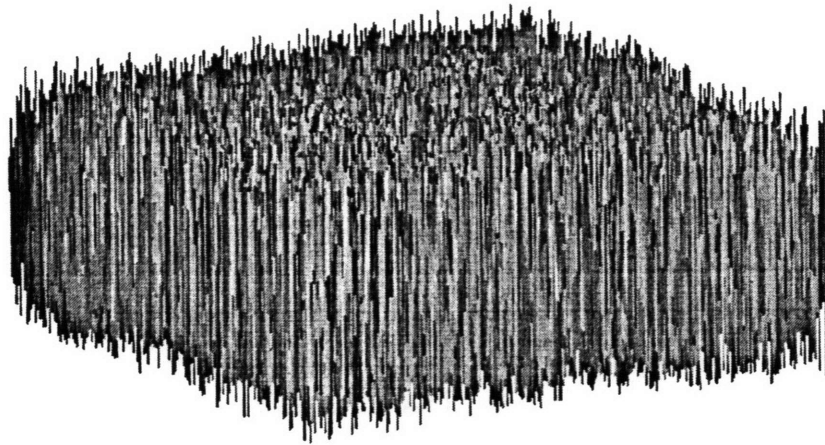
Figure 6.8: Half Coated with Diffuse White Paint, 128 Frames

The experiment shown in Figure 6.9 was done using a part coated with diffuse white paint, but under adverse ambient conditions. The foam walls which I used to protect the system from air turbulence were taken down, and a 16 inch diameter oscillating fan was aimed at the system. The utter mess seen in Figure 6.9 (a) is the unfiltered data which resulted. The experiment

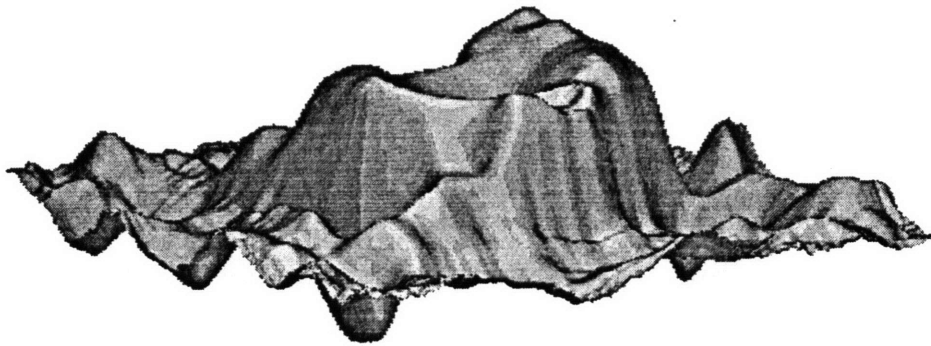
may look like a lost cause, but some range data must be present in the Fourier transform, as is evident from the filtered image in Figure 6.9 (b). Although the image is a terrible one, the range rises in the center and drops towards the edges, so there is still hope of recovering some information.

Once again, I tried “special filtering”. The resulting image shown in Figure 6.9 (c), has the general shape of the target, but the noise level is too high to claim that much range information was salvaged. Looking at Figure 6.9 (d), which is much cleaner, one can see large low-frequency surface variations on the top of the part. Since the image is being compared with the nice image from Figure 6.5 (c) to a tolerance of plus or minus 2 mm, passing complete noise through the “special filter” would produce something that looked remotely like the part. I must conclude that either too much air turbulence badly effects the ability of the laser speckle system to take data or that the range data is still held in the three-dimensional Fourier transform and must be extracted by other means. I believe that the latter is true. With sufficiently intelligent image processing, it should be possible to extract range information. If the information can not be extracted even by complex filtering means alone, one possible solution is to simultaneously record a reference image which is close enough to the target to be affected by the same wind currents. The effects of the wind currents could then be subtracted out of the Fourier transform, leaving data which can be processed to yield clean range data.

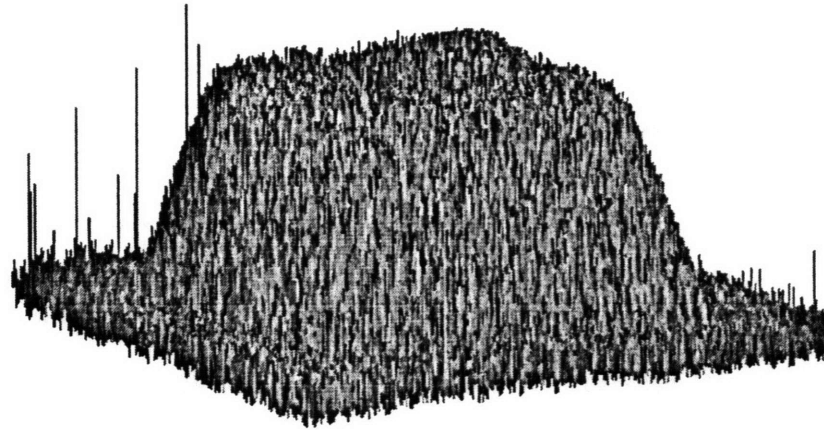
Part of the reason why the image in Figure 6.9 is of such poor quality may be due the laser frequency step size. This experiment was done right after the experiment shown in Figure 6.3, and both experiments used the same 1.9 GHz step size. Since the large step size seemed to contribute to the amount of noise in Figure 6.3 (a), it seems natural to assume that it also contributed to the noise in Figure 6.9.



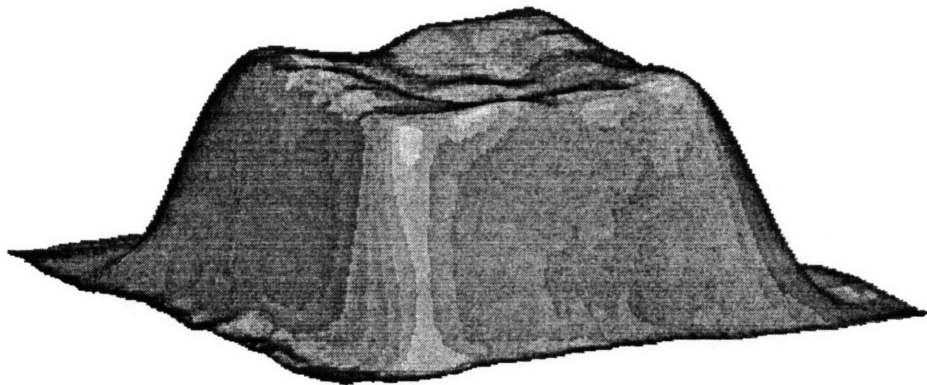
(a) no filtering



(b) heavy filtering



(c) special filtering



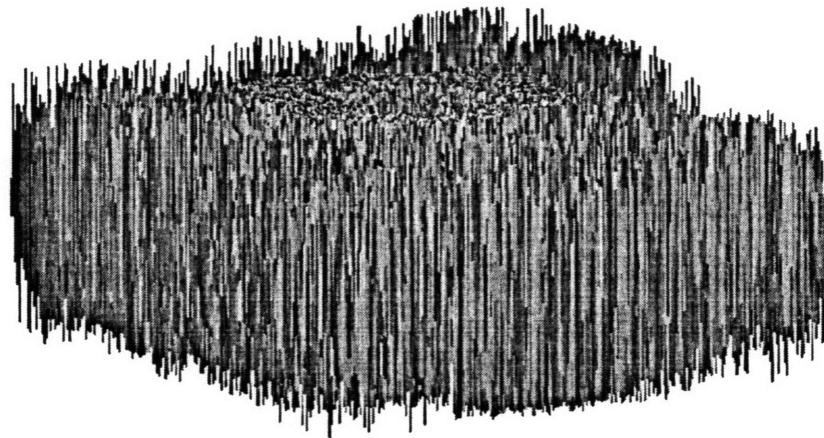
(d) heavy special filtering

Figure 6.9: Diffuse White Paint, Oscillating Fan, 128 Frames

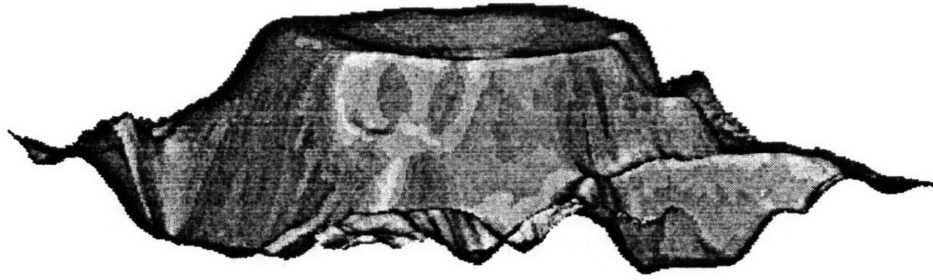
The last experiment I performed was also a test of the laser speckle technique's robustness to adverse ambient conditions. The experiment was performed on a part which was fully coated with diffuse white paint, and the foam turbulence tent was removed, but instead of using an oscillating fan, the air circulation system in the lab was left on, which produced a slight breeze

through the system. The unfiltered image is shown below in Figure 6.10 (a). There is a marked improvement from the image in Figure 6.9 (a), but there is still a large amount of high frequency noise. The image in Figure 6.10 (b) also shown improvement over Figure 6.9 (b), but the image still bears only vague resemblance to the target.

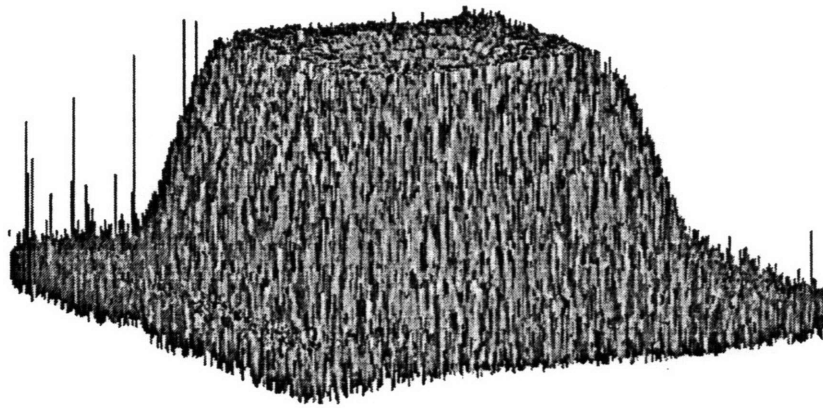
The addition of “special filtering” produces an image much cleaner than that in Figure 6.9 (c), and “heavy special filtering” produces a pretty good image. There is much less low frequency surface variation in Figure 6.10 (d) than in Figure 6.9 (d), but there is a depression at the front right corner of the part which I can not explain. It seems that a lower amount of air turbulence and a smaller frequency step preserves much of the range information from a laser speckle experiment, but the part still does not exactly resemble the target. However, the results of this experiment seem to indicate that there is a way to extract range information from a system operating under turbulent conditions.



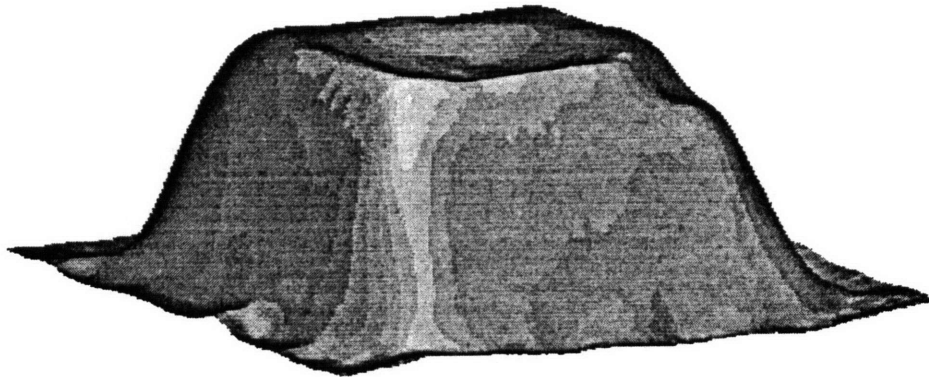
(a) no filtering



(b) heavy filtering



(c) special filtering



(d) heavy special filtering

Figure 6.10: Diffuse White Paint, Air Circulation On, 128 Frames

6.4 Comparison of CMM Data to Laser Speckle Data

Because of the varying quality of the images shown in the previous section, it would be difficult to appropriately quantify the accuracy of all of the measurements. For this work, I chose what I felt was the image which most closely resembled the target to use as the representative of the laser speckle technique in a comparison to an image created from measuring the same part with a coordinate measuring machine. I chose the image from Figure 6.5 (c), which was of a part lightly coated with white diffuse paint.

The first step in obtaining a quantitative comparison between the methods was to get both images in the same scale. Since the software which the CMM used created a data file with the information already in millimeters while laser speckle does not, it is necessary to scale the height of the laser speckle image. Fortunately, this is an easy task. Since the unfiltered height measurements of a target in laser speckle are limited to discrete range values a fixed distance apart, one simply needs to multiply the number of the range plane a particular x,y point is in by the range resolution of the experimental run. This range resolution can be determined via Equation 4.4. Once this is

done, both the laser speckle data set and the CMM set should be shifted such that the smallest value in each matrix is zero.

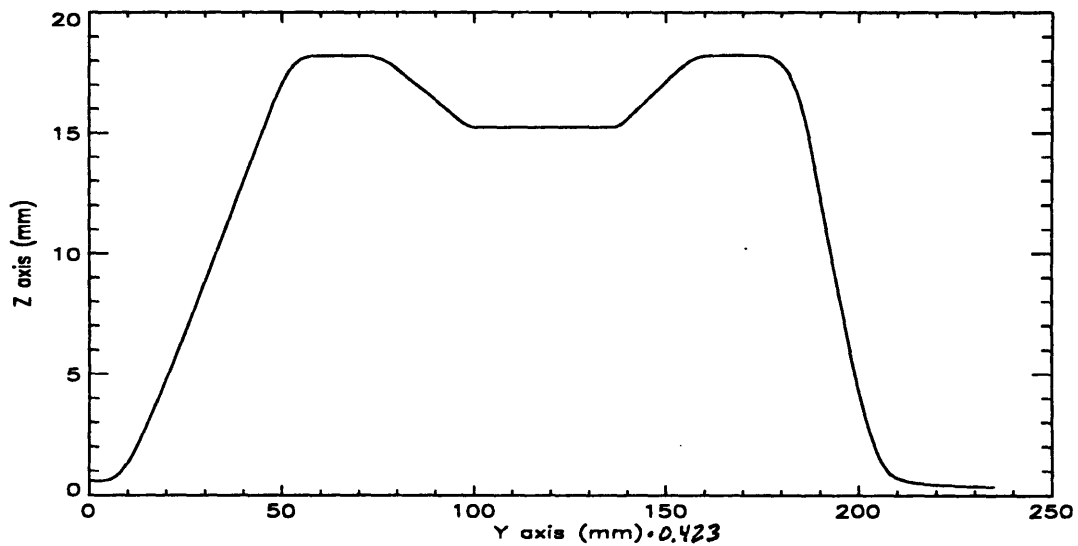
Once that was done, the x and y axis scales need to be resolved. The easiest way to do this was to scale the CMM data. Since the CMM data is smoother and more accurate than the laser-speckle data, less errors in interpolation were likely. To do that, however, a scaling constant is needed. To obtain this constant, I took a slice along the center of the y - z plane of each sample set and measured the width of the part at three heights, divided the width from one set by the width from the other at each height, and averaged the results. The reason I chose the x - z plane to slice with was that the left side of the laser speckle set was expected to have higher error because of the weakness of the beam in that area. By cutting through the middle of the part along the y - z plane, I completely avoided the left edge of the part.

The CMM part was scaled using a bilinear interpolation algorithm from PV Wave, a mathematical package, on a Sun Sparcstation 2. The scaling constant used was 2.37, and the CMM data set was scaled from one with 111 by 111 points to one with 261 by 261 points. The only problem with this is that each pixel is now horizontally separated by 423 μm instead of the convenient 1 mm spacing of the CMM.

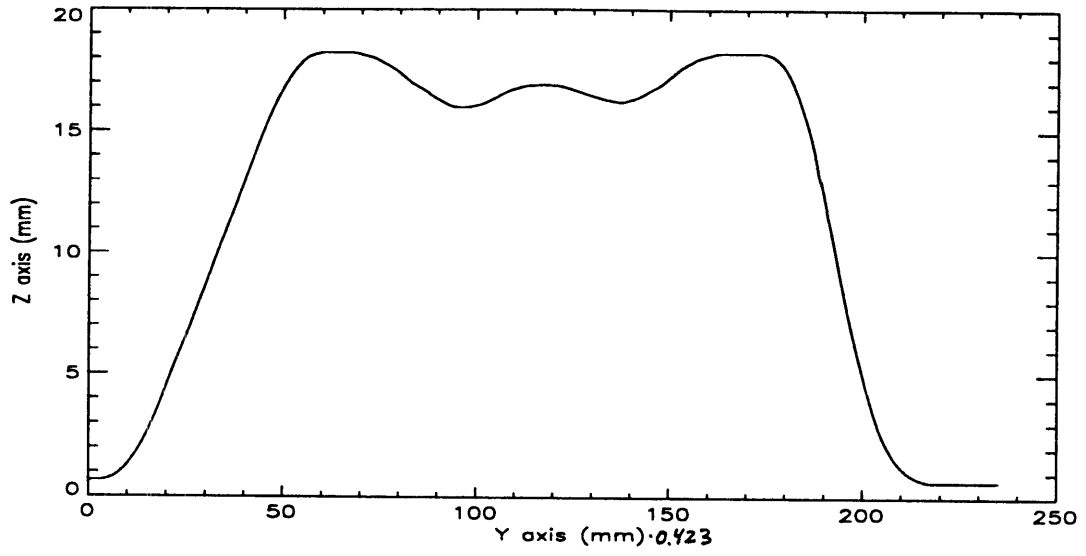
After the x - y scaling was done, I did some x - y and z fine tuning by translation of the CMM data set, and I was able to obtain approximate mating of one y - z cross section of the center of each sample. A comparison of these cross sections is shown below in Figure 6.11. Figure 6.11 (a) shows a cross section of the CMM data set, Figure 6.11 (b) shows a cross section of the laser speckle data set, and Figure 6.11 (c) shows these two plots overlaid on each other. The match is visually impressive, except for the center section, where the laser speckle system was not able to take measurements because of the presence of the reference mirror.

Figure 6.11 (d) presents an error plot of the difference between the cross sections of the laser speckle and the CMM data sets. Notice that the error is highest on the back wall of the part, which has the highest slope and therefore would be expected to return the least amount of light. Also notice that the

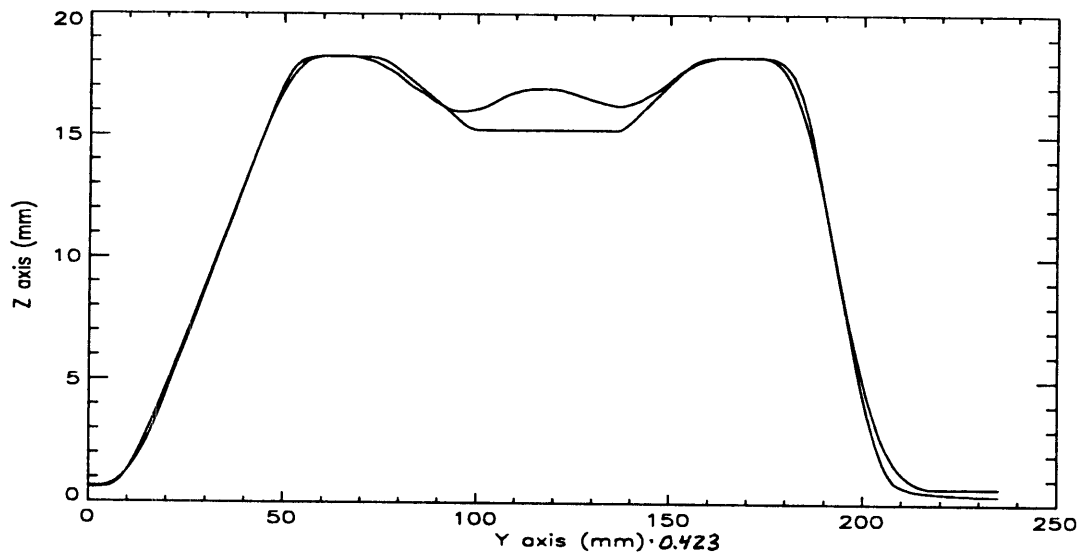
areas of largest error are at the edges of the surfaces, where the filtering algorithm excessively smoothed the surface, rounding the edges. Discounting the center section, the largest and smallest errors between the cross sections were $808 \mu\text{m}$ and $-628 \mu\text{m}$, for a peak to peak difference of $1436 \mu\text{m}$, which can be translated vertically to become target $\pm 718 \mu\text{m}$, only slightly larger than the range resolution of the experiment, $651 \mu\text{m}$. With better filtering and smoothing algorithms, the accuracy could exceed the range resolution. Figures 6.11 (e) and (f) present the left and right side of plot 6.11 (d), omitting the center section for better resolution and easier interpretation of the magnitude of the error.



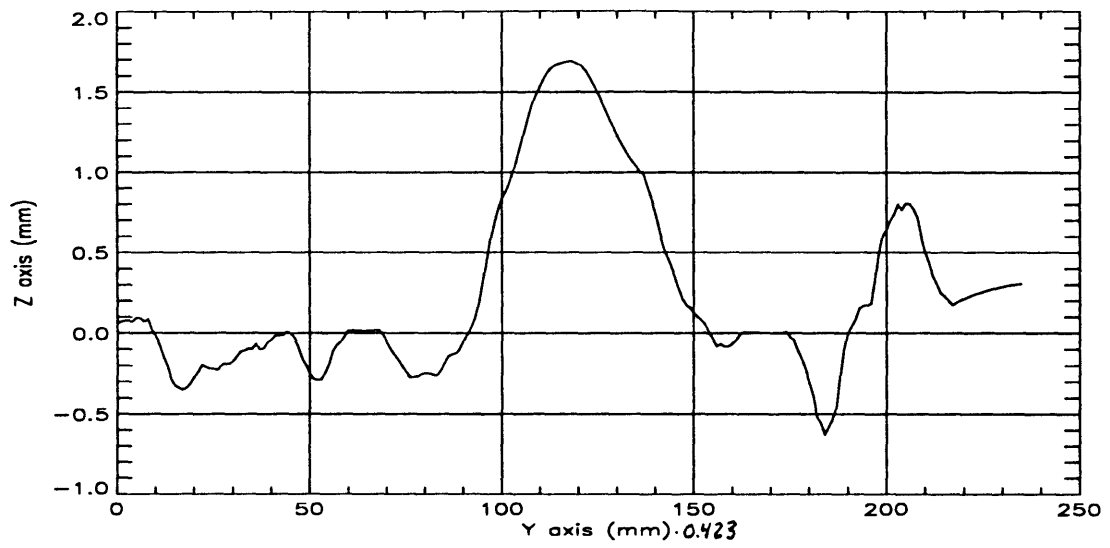
(a) CMM Measurement



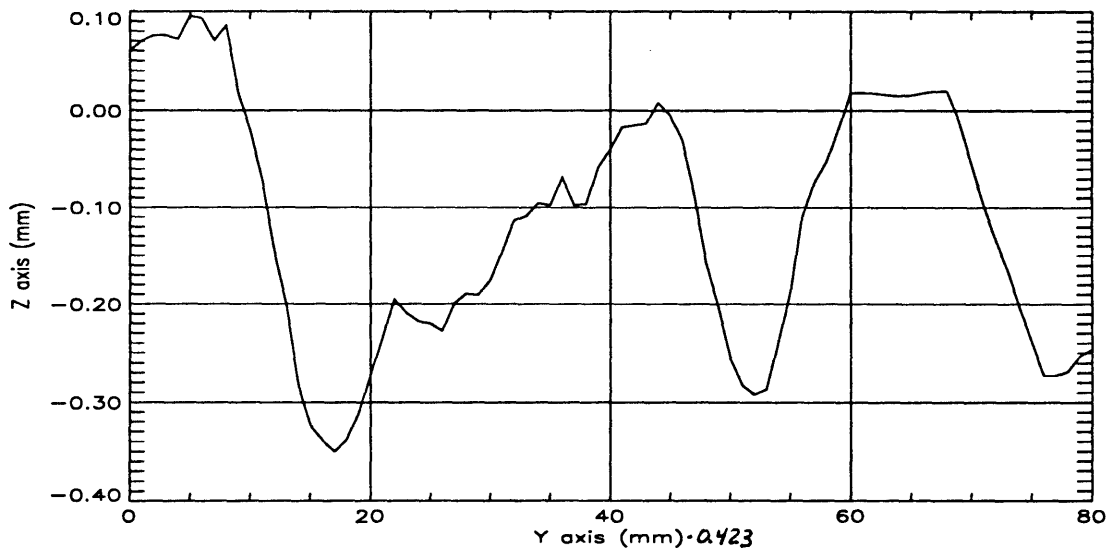
(b) Laser Speckle Measurement



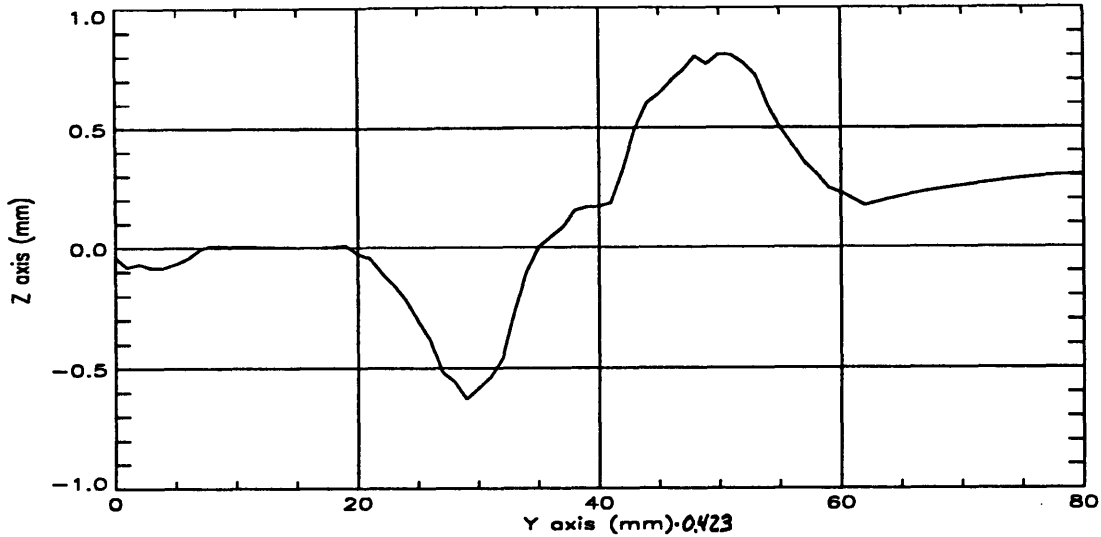
(c) Both Techniques



(d) Error Plot



(e) Left Side of Error Plot



(f) Right Side of Error Plot

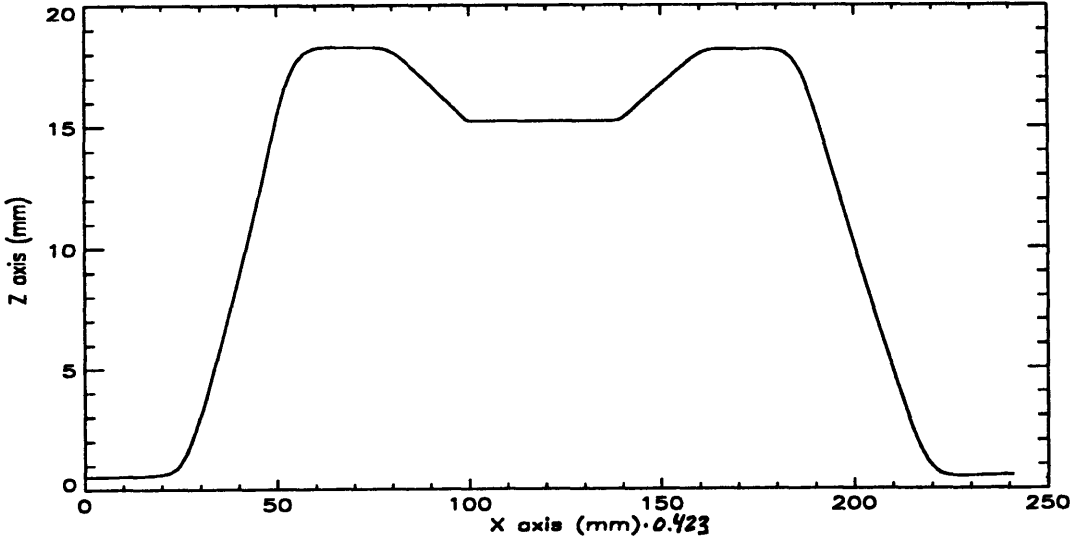
Figure 6.11: Comparison: Y-Z Slice Through Part

Once the scaling issues were resolved, it was an easy extension to compare a x - z slice through the center of each of the two data sets used for comparison. The slices still needed to be translated horizontally to mate, but that is not difficult. A comparison of these x - z slices are shown below in Figure 6.12. Figure 6.12 (a) shows a cross section of the CMM data set, Figure 6.12 (b) shows a cross section of the laser speckle data set, and Figure 6.12 (c) shows these two plots overlaid on each other. This time, the mating is not as impressive, but that might have been expected. Of course the mating in the center will not be accurate because of the reference mirror, but the mating of the left side is worse. The reason for this would most likely be explained by the problem with not enough light being returned from the left wall of the part because of the limited beam power.

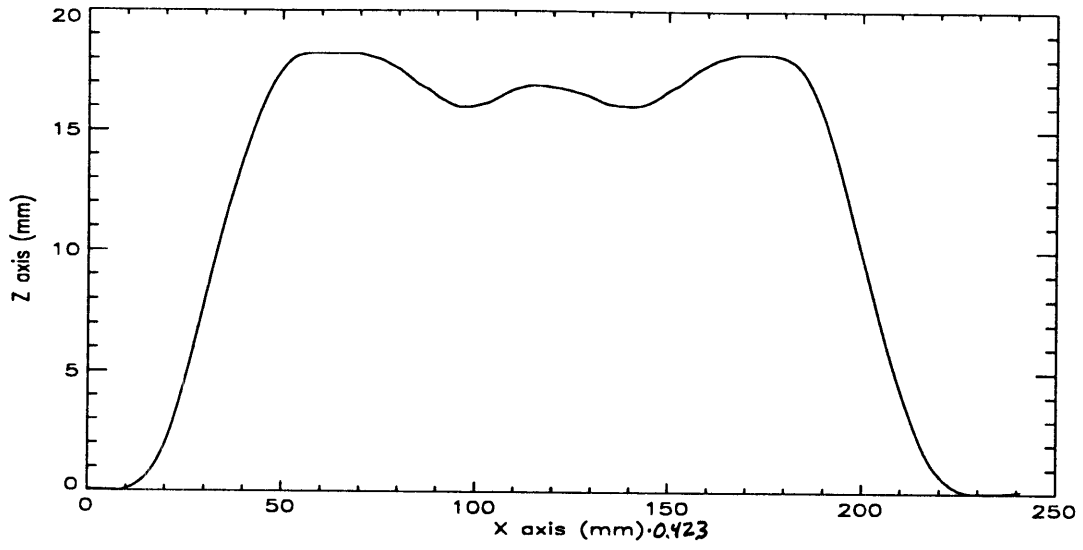
Experimentally, we observed in the previous section that a relatively small light return from certain areas of a part may result in the extension of surfaces normal to the beam and the increase in slope of the walls which are not returning enough light. This is the most likely explanation for the stretching of the laser speckle slice in the x - z plane. The relatively greater light reflected back from the top surface could cause a slight glare, pushing the edge

of the surface further out. Although the slope of the left wall looks approximately the same in both slices, approximately equal slopes may be expected since the laser speckle slice we are comparing has been heavily filtered, which would help decrease the slope of the wall.

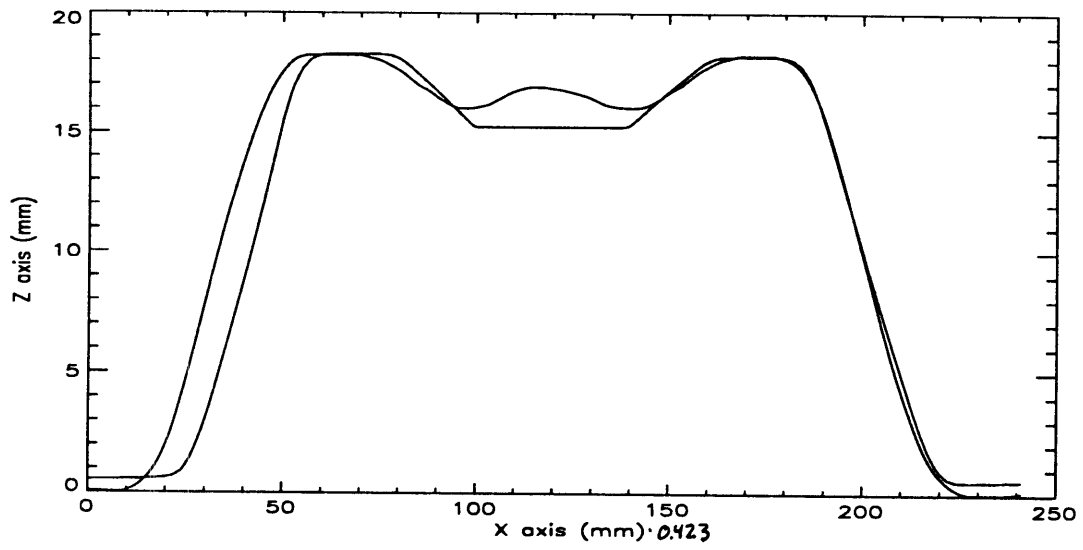
Figure 6.12 (d) presents an error plot of the difference between the two cross sections. Of course the error is highest on the left side, where a lateral shift of the location of the part wall by a millimeter or two can cause an error of a maximum of 5.26 mm. In contrast, the error on the right side of the part is quite small indeed. The largest and smallest errors between the cross section there were 226 μm and -723 μm , for a peak to peak difference of 949 μm , which can be translated vertically to become target $\pm 475 \mu\text{m}$, which falls safely inside the range resolution of the experiment, 651 μm . The problem with the left side could probably be fixed easily with a stronger laser or one with better beam quality. Figures 6.12 (e) and (f) present the left and right side of plot 6.12 (d), omitting the center section for better resolution and easier interpretation of the magnitude of the error



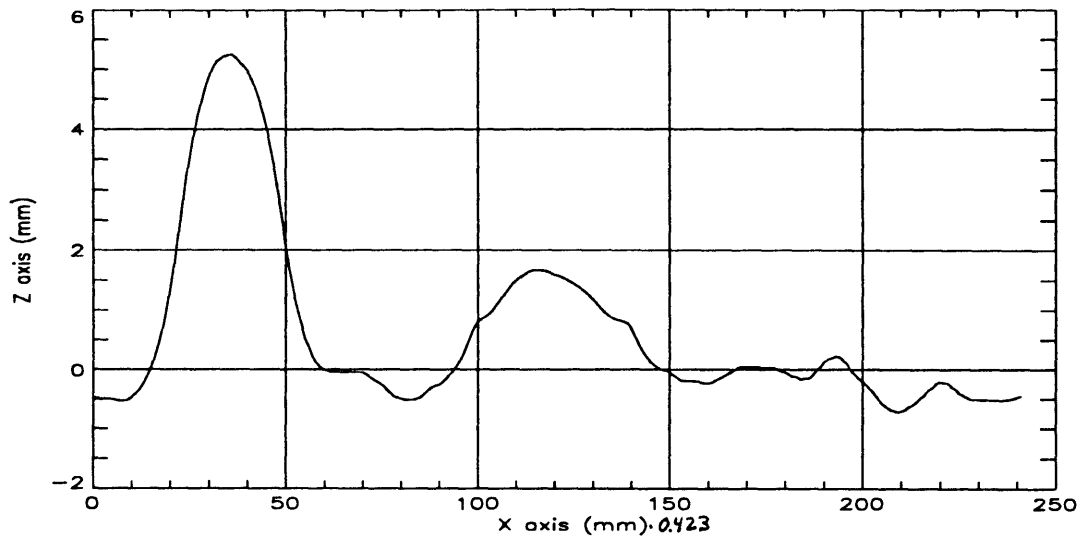
(a) CMM Measurement



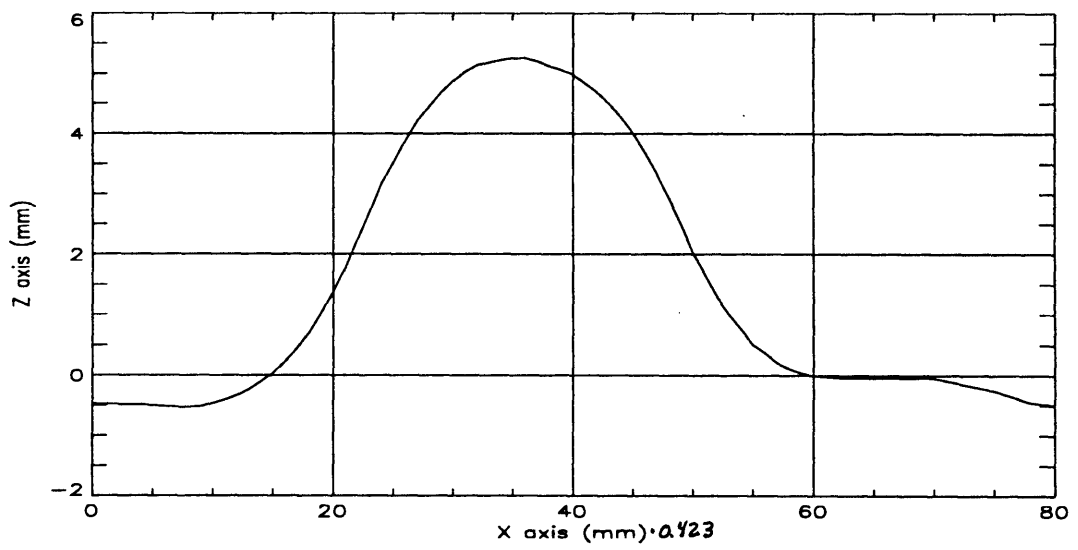
(b) Laser Speckle Measurement



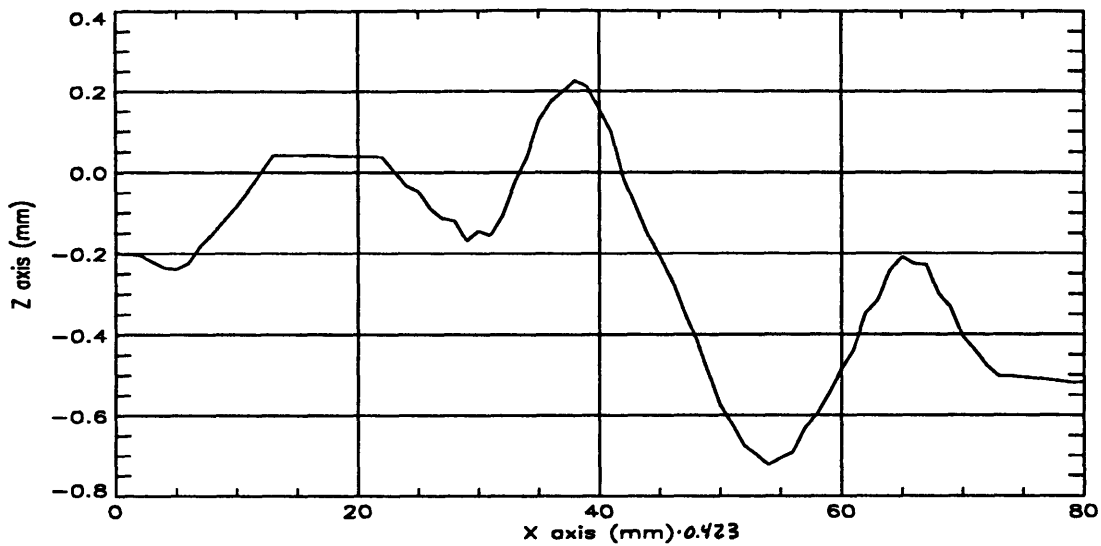
(c) Both Techniques



(d) Error Plot



(e) Left Side of Error Plot

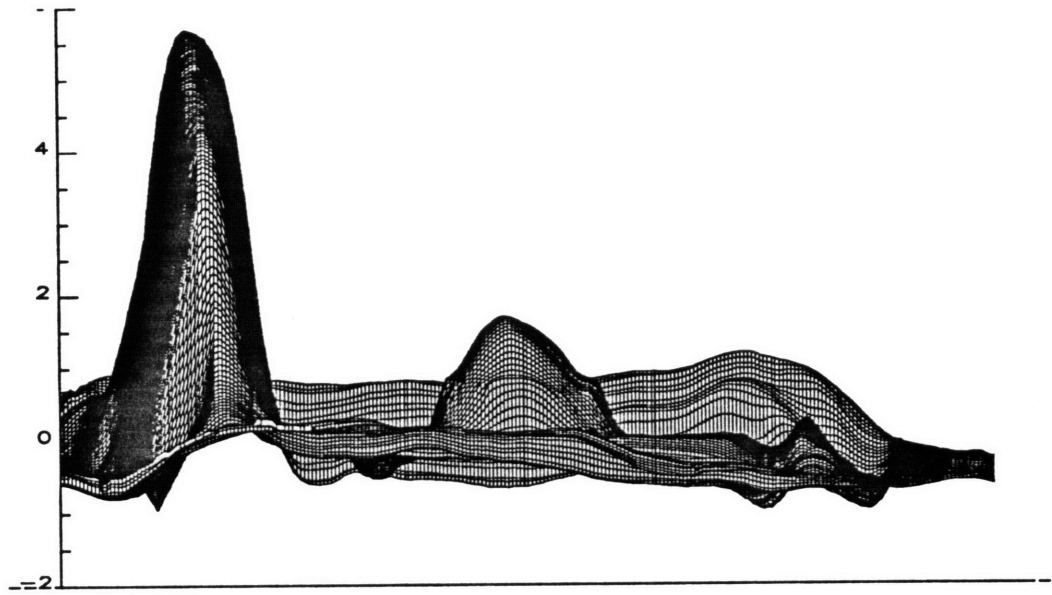


(f) Right Side of Error Plot

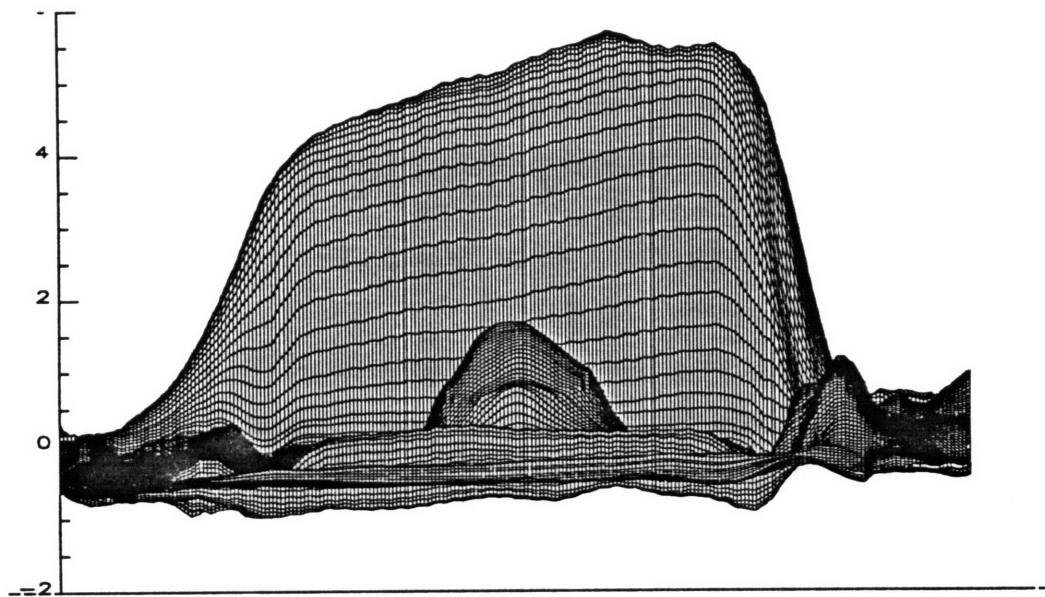
Figure 6.12: Comparison: X-Z Slice Through Part

The next step was to create an error map for the whole surface of the part. Several error maps are presented in Figure 6.13. Figure 6.13 (a) is seen along the y axis, with the x and z axes framing the Figure. As we saw above in the cross sectional slices, the error is large on the left side and small on the right. The maximum error on the left is 5.69 mm, and the maximum and minimum errors on the right side are 1185 μm and -978 μm , for a peak to peak error of 2.16 mm, and a translated accuracy of 1.08 mm, larger than the range resolution, but not very bad. Figure 6.13 (b) displays the same error map, but it is seen along the x axis, with the y and z axes framing the Figure.

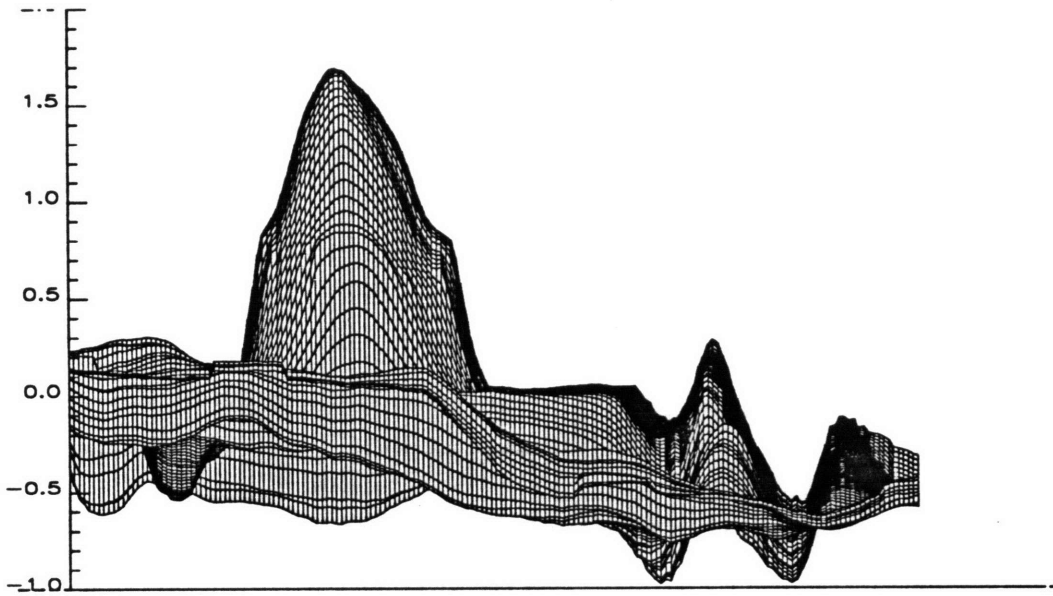
Figures 6.13 (c) and (d) display similar information, but I removed the left quarter of the part and the back quarter of the part, where the errors are high for specific reasons. Over the rest of the part, excluding the center of course, the maximum and minimum errors are 304 μm and -978 μm , for a peak to peak error of 1282 μm , and a translated accuracy of 641 μm , which is just less than the range resolution of 651 μm . Figure 6.13 (c) is seen along the y axis, with the x and z axes framing the Figure, while Figure 6.13 (d) shows the same information seen along the x axis.



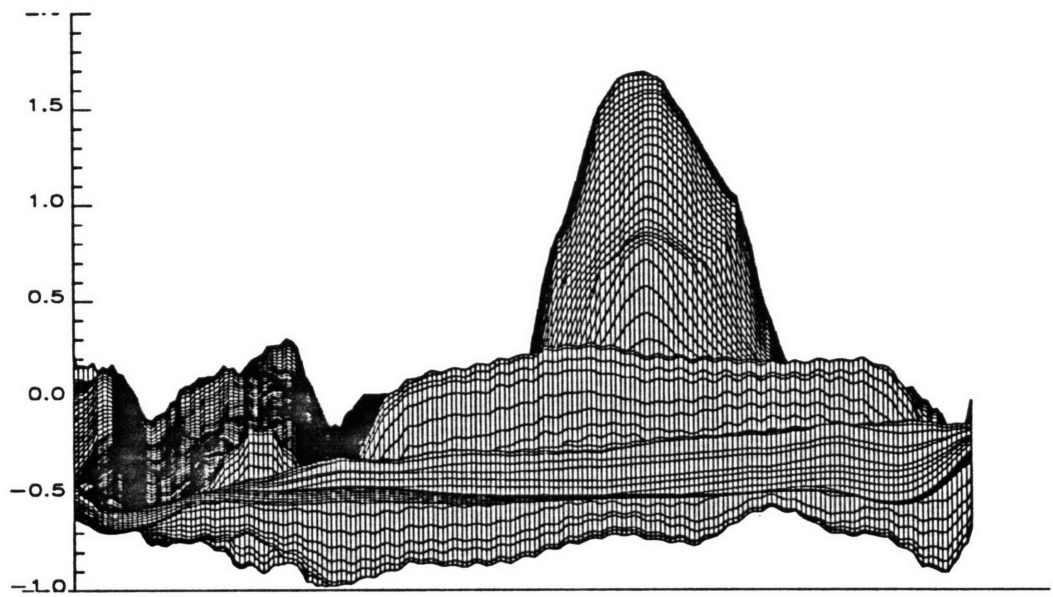
(a) Error Map From Y Direction



(b) Error Map From X Direction



(c) Part of Error Map From Y Direction



(d) Part of Error Map From X Direction

Figure 6.13: Whole Target Error Mapping

7

Conclusions and Recommendations

7.1 Review of Results: CMM vs. Laser Speckle

While the range resolution of the laser speckle wavelength decorrelation technique is theoretically limited only by the tunable range of the laser and the ability to tune in equal steps, there are several things which limit the practical accuracy of the technique today.

Qualitatively, the best images were obtained by coating the surface of the target with a diffuse white paint. A white paint was used because of its reflective characteristics, and a diffuse paint was used to help prevent excessive return from one spot of the target, most likely one normal to the axis of the laser. Also, image clarity was improved by keeping the system isolated from air currents. Although nice images were able to be extracted using various filtering techniques, more research still needs to be done in this area to allow the accuracy of measurements taken of highly reflective surface finishes or under hostile ambient conditions to approach that of those taken under ideal conditions.

Quantitatively, when compared to a CMM measurement as a standard, the laser speckle system was capable of a range accuracy of $\pm 1082 \mu\text{m}$ (0.0426 in) for a range resolution of $651 \mu\text{m}$ (0.0256 in). This was the maximum error range over most of the surface of a 100 mm by 100 mm (4 in

by 4 in) section of a sheet metal part, sampled in approximately a 423 μm (0.0167 in) grid spacing.

7.2 Laser Speckle: Where is it Headed?

Although the technique is being researched [2,73,74], no one has yet made commercially available a three-dimensional imaging sensor based on the laser speckle wavelength decorrelation technique. Shirley [75] has obtained a range RMS error of 0.6 μm measuring a flat surface. Laser speckle has the potential of becoming a very powerful technique.

It would seem that the laser speckle technique would be most useful in measurement of large targets. Range resolution is not dependent upon the distance from the sensor to the part, so there is a great potential for use in measuring large objects, where the main competition is slow, bulky CMMs or digital theodolites. Also, a laser speckle system would not get more expensive measuring big parts, while the cost of most other commercially available systems rises exponentially with part size. The automobile industry seems like a good possible place to start.

However, to take advantage of this potential niche market or others, much research still needs to be done. The most important of this work is in the area of image processing. Currently, a clean image can be obtained for a part only after much time is spent trying different filtering schemes tailored for the specific part which was measured. In order to be used in a practical manufacturing capacity, software needs to be written which can automate the image processing based on information which the camera receives, not on the expert judgment of a researcher. A lot of work needs to be done devising algorithms for extracting information out of measurements taken under poor ambient conditions or of parts with reflective surface finishes. Also, in order to speed up the time it takes to process images, greater computing speed is needed. Mermelstein [78] has developed a parallel processing computer which should greatly reduce the time necessary to perform three-dimensional Fourier transforms for laser speckle measurements.

Another important area of future research deals with upgrading the experimental system itself. Using the Ti:sapphire laser, parts currently take about an hour to measure. Even then, only parts which are smaller than 100 mm in each dimension can be measured using the version of the laser speckle technique tested in this work. A more powerful laser is needed, as well as one which can tune more quickly, without the use of a wavemeter. The New Focus external cavity tunable diode laser is a potential candidate, but work needs to be done to determine whether or not it is necessary to take consistently spaced laser frequency steps to obtain the required accuracy.

Also, it is currently necessary to place a reference mirror on or near a part in order to obtain a measurement. It is possible to avoid the use of a reference mirror near the part by using a beam splitter to pick off part of the beam to take measurements of the reference mirror, but a large beam splitter was not available for this work. Once the need for a reference mirror near the part is eliminated, speckle will become a much more flexible system.

In addition, other variations of the laser speckle wavelength decorrelation technique described by Shirley [75] are being researched. The possibilities seem endless with enough research and development of new laser speckle ideas.

7.3 Metrology Solution for Flexible Sheet Metal Forming

The primary needs for a three-dimensional metrology system for sheet metal forming are an accuracy of 25 μm or less, almost real time measurement speed, and robustness to various surfaces and ambient conditions.

The fundamental technologies on which most metrology products are based can be grouped into eight main categories:

- mechanical contact
- stereo disparity
- point laser triangulation
- moiré interferometry

- range from focus
- Fresnel diffraction
- holographic interferometry
- laser radar

Machines which use mechanical contact, mostly coordinate measuring machines, are widely used for three-dimensional manufacturing metrology. CMMs are capable of sub-micron range and cross-range accuracy. Although measurement times are very slow, the combination of high accuracy, ease of use, and robustness to part surface finishes and ambient conditions keep CMMs in heavy use in American industry. However, CMMs are not necessarily the best choice for sheet metal measurement.

Stereo disparity is mainly used for robot guidance and other applications where micron level accuracy is not required. The problems associated with correspondence, matching pixels in one view to those in the other, are great enough to make the technique a relatively poor one for accurate three-dimensional manufacturing measurement. This can be inferred from the paucity of commercially available products for three-dimensional manufacturing metrology which rely on this technique.

The most widely commercially available non-contact three dimensional metrology method is point laser triangulation. Sensors which use this technique can achieve sub micron range resolution and a data collection rate of 10,000 points per second. A sensor using the autosynchronized scanning method seems ideal for use in sheet metal manufacturing. The major drawback of point laser triangulation devices is the occlusion problem. The laser must be able to reflect into the detector, so very steep walls are sometimes a problem when they block the path to the detector.

Moiré interferometry is in moderate use in industry. The technique is most useful when measuring smooth parts without sharp changes in slope. Although moiré methods can achieve a range accuracy of a few microns, the ambiguity interval inherent with moiré limits its use to smoothly varying surfaces. Moiré interferometry can be an excellent technique for use in a system which adheres to the slope and field of view restrictions. Another thing

which limits use of the technique is that processing must be done to the images taken to determine range values. This causes the measurement speed to be slow. Medar's Cadeyes system can analyze data in about 15 seconds, which is much better than a CMM, but not real time. However, as computing power increases, moiré systems will approach real time data processing.

Range-from-focus systems may be good in low accuracy and speed applications, but its disadvantages make it a poor choice for three-dimensional manufacturing metrology. The systems can achieve an accuracy on the order of one millimeter, which is not good enough for sheet metal forming. The main thing which limits the range accuracy is the ability of a computer controlled algorithm to determine which ranges are in focus and which are not. As these algorithms improve, so will the potential use of rang- from-focus systems.

Systems based on Fresnel diffraction are not widely used. The main disadvantage to the use of diffraction is that the range accuracy depends on the ability to determine the level of brightness contrast between different areas of the target. This limits the range accuracy of current systems to about 100 μm . Also, images taken using this technique need processing before range values are obtained. Therefore, real time imaging is difficult, but it will be come easier once computing speed increases.

Holographic interferometry is capable of sub-nanometer resolution, but the small fringe spacing limits the depth of field to about 100 μm . In addition, holographic interferometry can only be used on smooth surfaces. This limits use of the technique to surfaces which have no sharp slopes or abrupt surface height changes of more than a few microns. Thus, holographic interferometry is not useful for creating range maps of sheet metal parts. The technique is used mostly to detect small differences in range in parts under pressure or stress. It can also be used to determine the surface roughness of a part.

Some laser radar systems show promise for use in manufacturing metrology. Pulse laser radar is not a good candidate for measuring sheet metal because the range accuracy is limited to a few cm. The reason for this is that light moves very fast relative to current ways to measure time. Even if a time

difference of 100 picoseconds is achieved, that still only allows for a range resolution of a few cm.

Amplitude modulated continuous wavelength (AM CW) laser radar is much more practical for manufacturing metrology. A range accuracy of a few microns is possible, and by scanning the laser in two dimensions with mirrors, a data acquisition rate of 30,000 points per second is possible. The main disadvantage of this technique is that there is a limit to the depth of field because of the inherent ambiguity interval. However, the ambiguity interval only limits the sensor to a depth of field of a few meters for a range accuracy of a few microns. This is acceptable for many sheet metal manufacturing applications. Unfortunately, I could only find one company, Perceptron, who has such a device currently available, although several are performing research in the area.

Frequency modulated continuous wavelength (FM CW) laser radar is also potentially practical for manufacturing use. A range accuracy of 50 μm has been reported over a depth of field of 2.5 m. I could not find any commercially available products which use the technique, but several are researching the method.

Laser speckle wavelength decorrelation is capable of sub-micron range accuracy, and unlike AM CW laser radar, the depth of field is not limited to a few meters. The range resolution of laser speckle measurements is only dependent upon the range extent of the object to be measured and the tuning range of the laser used. However, with current technology a single 256 by 256 pixel measurement takes an hour to record and even more time to complete the image processing. Once the main drawbacks of measurement and image processing time, portability, and poor accuracy under adverse ambient conditions are solved, laser speckle could provide the best combination of speed and accuracy of any commercially available technique.

In the short term, scanning laser triangulation sensors from companies such as Hyscan give the best combination of speed and accuracy. Such a sensor can measure a part at a range accuracy 25 μm at a speed of 10,000 points per second. Almost as good would be a system based on amplitude

modulation continuous wavelength laser radar. Perceptron's Lasar sensor can also meet the 25 μm accuracy and 10,000 points per second speed. However, few companies have such systems available, and even the Lasar is still currently under development. In the long term, advances in computer power and laser design will make a system such as laser speckle the best combination of speed and accuracy. Laser speckle is not limited in field of view, and it has no moving parts — thus scanning is not necessary. Without the need for scanning, there are few limits to the speed of data collection given enough computer power. However, a laser speckle system will probably not be able to measure 10,000 points per second at a 25 μm range accuracy for at least another five years.

Bibliography

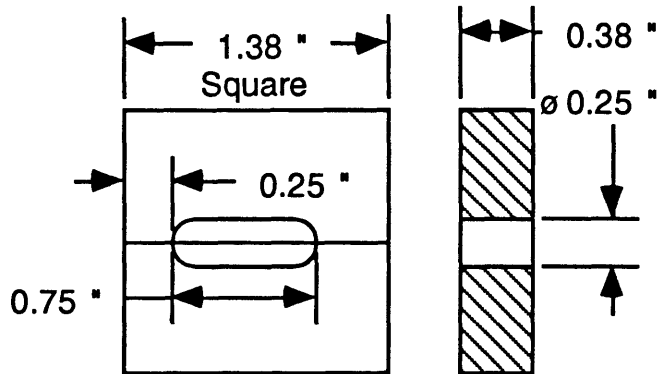
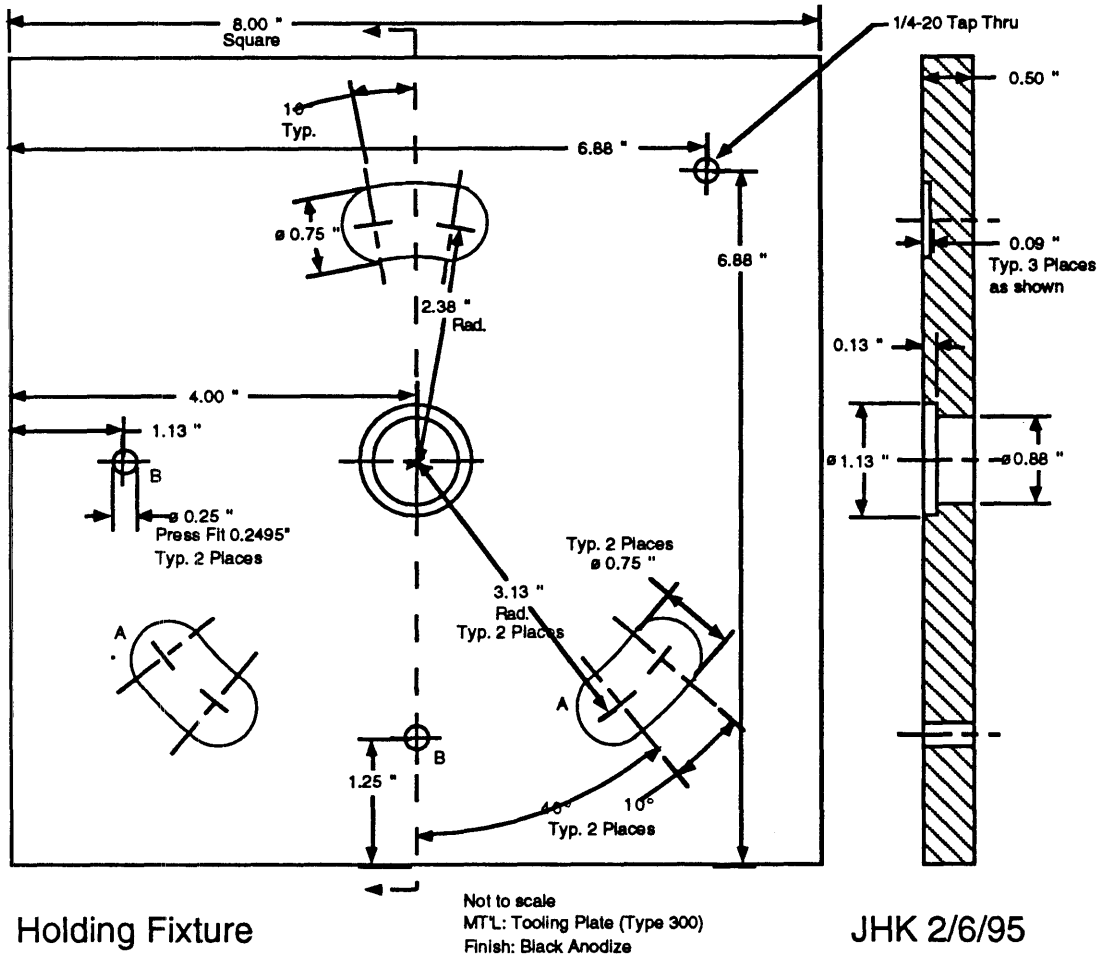
- [1] Hardt, David E., Boyce, Mary C., Ousterhout, Karl B., Karafillis, Apostolos, and Eigen, Gary M., "A CAD-Driven Flexible Forming System for Three-Dimensional Sheet Metal Parts", SAE Technical Paper Series, Sheet Metal and Stamping Symposium, Detroit, Michigan, Vol. SP-944, (March 1993) pp. 69-76.
- [2] Shirley, Lyle G. et. al., "Advanced Techniques for Target Discrimination Using Laser Speckle", The Lincoln Laboratory Journal, Vol. 5, No. 3, (1992), pp. 367-440.
- [3] Ousterhout, Karl B., "Real-Time Control of a 3D Sheet Forming Process", Ph.D. Thesis, Massachusetts Institute of Technology, (1991).
- [4] Renishaw Metrology Limited, Gloucestershire, UK, United States Patent No. 5,040,306, (1991).
- [5] Mathia, T., Zahouani, H., Rousseau, J., and LeBosse, J.C., "Functional Significance of Different Techniques for Surface Morphology Measurements", Int. J. Mach. Tools Manufact., Vol. 35, No. 2, (1995), pp. 195-202.
- [6] Stout, K.J., and Blunt, L., "Nanometres to micrometres: three-dimensional surface measurement in bio-engineering", Surface and Coatings Technology, Vol. 71, No. 2, (1995), pp. 69-81.
- [7] Sherrington, I., and Smith, E.H., "Modern Measurement Techniques in Surface Metrology: Part 1; Stylus Instruments, Electron Microscopy and Non-Optical Comparators", Wear, Vol 1225, (1988), pp. 271-288.
- [8] Sherrington, I., and Smith, E.H., "A quantitative study of the influence of stylus shape and load on the fidelity of data recorded by stylus instruments", Proc. 2Nd National Conf. On Production Research, Edinburgh, September 1986, pp. 762-783.
- [9] Thomas, T.R., "Some Examples of the Versatility of Stylus Instruments", Mech. Mater. Electr., Vol. 337, (1978), pp. 17-25.
- [10] Sayles, R.S., and Thomas, T.R., "Mapping a small area of surface", J. Phys. E., Vol. 9, (1976), pp. 855-861.
- [11] Renishaw Metrology Limited, Gloucestershire, UK, United States Patent No. 5,353,514, (1994).
- [12] Renishaw Metrology Limited, Gloucestershire, UK, United States Patent No. 5,058,433, (1991).
- [13] MicroVal PFx User's Manual, Brown & Sharpe Mfg. Co., North Kingstown, RI, 1991.
- [14] Slocum, Alexander H., Precision Machine Design, Prentice Hall, Inc., Englewood Cliffs, NJ, 1992.
- [15] Tiziani, H.J., "High resolution optical surface topography measurements", Proceedings of SPIE - The International Society for Optical Engineering, Vol. 2252, (1993), pp. 23-32.
- [16] Cromwell, Robert L., "Sensors and processors enable robots to see and understand", Laser Focus World, (Mar. 1993), pp. 67-81.
- [17] Besl, Paul J., "Active Optical Range Imaging Sensors", in Sanz, Jorge L.C., ed., Advances in Machine Vision, Springer-Verlag, New York, Chapter 1, (1989), pp. 1-63.

- [18] Nitzan, David, "Three-Dimensional Vision Structure for Robot Applications", IEEE Transactions on Pattern Analysis and Machine Intelligence, Vol. 10, No. 3, (1988), pp. 291-309.
- [19] Bieman, Leonard H., "Survey of design considerations for 3-D imaging systems", Proceedings of SPIE - The International Society for Optical Engineering, Vol. 1005, (1988), pp. 138-144.
- [20] Wagner, John F., "Sensors for Dimensional Measurement", Vision, (1987), pp.13.1-13.18.
- [21] Strand, T.C., "Optical three-dimensional sensing for machine vision", Optical Engineering, Vol. 24, No. 1, (1985), pp. 33-40.
- [22] Murray, Lawrence A., and Chu, Cuong, "Laser Gauging Goes Three-Dimensional", Lasers & Applications, (Aug. 1984), pp. 83-87.
- [23] McFarland, William D., and McLaren, Robert W., "Problems in three-dimensional imaging", Proceedings of SPIE - The International Society for Optical Engineering, Vol. 449, (1983), pp. 148-157.
- [24] Jarvis, R.A., "A Perspective on Range Finding Techniques for Computer Vision", IEEE Transactions on Pattern Analysis and Machine Intelligence, Vol. PAMI-5, No. 2, (1983)
- [25] Riggs, A.J., and Sampson, R.E., "3-D Range Imaging Sensors", Environmental Research Institute of Michigan, pp.109-114.
- [26] Grimson, W. Eric L., "Computational Experiments with a Feature Based Stereo Algorithm", IEEE Transactions on Pattern Analysis and Machine Intelligence, Vol. PAMI-7, No. 1, (1985), pp. 17-34.
- [27] Baker, H.H., "Edge based stereo correlation", Proc. ARPA Image Understanding Workshop, Univ. Maryland, (Apr. 1980).
- [28] Moravec, H.P., "Visual mapping by a robot rover," Proc. 6Th Int. Joint Conf. Artificial Intell., (1979), pp. 598-620.
- [29] Dremel, W., Häusler, G., and Maul, M., "Triangulation with large dynamical range", Proceedings of SPIE - The International Society for Optical Engineering, Vol. 665, (1986), pp. 182-187.
- [30] Zeiss, Product literature, Santa Monica, CA, (1994).
- [31] Cubic Precision, Electro-Optical Division of Cubic Corporation, Product literature, Teterboro, NJ, (1994).
- [32] Brunson Instrument Company, Product literature, Kansas City, MO, (1994).
- [33] Percrptron, Inc., Product literature, Farmington Hills, MI, (1994).
- [34] Measurement Technologies, Inc., Product literature, Santa Monica, CA, (1994).
- [35] Medar, Product literature, Farmington Hills, MI, (1994).
- [36] Canadian Patents and Development Limited, Ottawa, Canada, United States Patent No. 4,627,734, (1986).
- [37] Rioux, Marc, "Laser range finder based on synchronized scanners", Applied Optics, Vol. 23, No. 21, (1984), pp.3837-3844.
- [38] Hymarc Ltd., Product literature, Ottawa, Canada, (1994).
- [39] Medar, Product literature, Farmington Hills, MI, (1994).
- [40] Araki, Kazuo, Sato, Yukio, and Parthasarathy, Srinivasan, "High Speed Rangefinder", Proceedings of SPIE - The International Society for Optical Engineering, Vol. 850, (1987), pp. 184-188.

- [41] United Scanning Technologies, Product literature, Vancouver, British Columbia, Canada, (1994).
- [42] Intelligent Automation Systems, Product literature, Cambridge, MA, (1994).
- [43] Modular Vision Systems, Product literature, Montréal, Québec, Canada, (1994).
- [44] Phase Shift Technology, Product literature, Tucson, AZ, (1994).
- [45] Electro-Optical Information Systems, Product literature, Santa Monica, CA, (1994).
- [46] Halioua, M., and Srinivasan, V., "Method and apparatus for surface profilometry", New York Institute of Technology, Old Westbury, NY, U.S. Patent No. 4,641,972, (1987).
- [47] Medar, Inc., Product literature, Farmington Hills, MI, (1994).
- [48] View Engineering, Inc., Product literature, Simi Valley, CA, (1994).
- [49] Harding, K., Michniewicz, and Boehnlein, A., "Small Angle Moire Contouring", Proceedings of SPIE - The International Society for Optical Engineering, Vol. 850, (1987), pp. 166-173.
- [50] Bieman, Leonard H., Harding, Kevin G., and Boehnlein, Albert, "Absolute measurement using field shifted moire", Proceedings of SPIE - The International Society for Optical Engineering, Vol. 1614, (1991), pp. 259-264.
- [51] Jarvis, R.A., "Focus optimisation criteria for computer image processing," Microscope, Vol. 24, No. 2, (1976), pp. 163-180.
- [52] Rioux, M., and Blais, F., "Compact 3-D camera for robotic applications", J. Opt. Soc. Amer., Vol. A3, No. 9, (1986), pp.1518-1521.
- [53] MicroVu, Product literature, Windsor, CA, (1994).
- [54] Ram Optical Instrumentation, Inc., Product literature, Huntington Beach, CA, (1994).
- [55] Leger, James R., and Snyder, Michael A., "Real-time depth measurement and display using Fresnel diffraction and white-light processing", Applied Optics, Vol. 23, No. 10, (1984), pp. 1655-1670.
- [56] Winthrop, J.T., and Worthington, C.R., "Theory of Fresnel images I. Plane periodic objects in monochromatic light", J. Opt. Soc. Amer., Vol. 55, No. 4, (1965), pp. 373-381.
- [57] Chavel, P., and Strand, T.C., "Range measurement using Talbot diffraction imaging of gratings", Applied Optics, Vol. 23, No. 6, (1984), pp. 862-871.
- [58] Lübbers, Hubertus A., Mrosik, Jan Michael, and Stojanoff, Christo G., "Development, analysis and performance tests of a chirped laser radar with optoelectronic signal demodulation", Proceedings of SPIE - The International Society for Optical Engineering, Vol. 2271, (1994), pp. 124-133
- [59] Nitzan, D., Brian, A.E., and Duda, R.O., "The measurement and use of registered reflectance and range data in scene analysis", Proc. IEEE, Vol. 65, No. 2, (1977), pp. 206-220.
- [60] Fornoff, Peter, "3D Robot Guidance with the Perceptron Laser System", Proceedings of SPIE - The International Society for Optical Engineering, Vol. 2271, (1994), pp. 214-217.
- [61] Perceptron, Product information, Farmington Hills, MI, (1995).

- [62] Skolnick, M.I., Introduction to radar systems, McGraw-Hill, New York, 1962.
- [63] Hersman, M., Goodwin, F., Kenyon, S., and Slotwinski, A., "Coherent laser radar application to 3D vision and metrology", Proc. Vision '87 Conf., Detroit, MI, (June 1987), pp. 3.1-3.12.
- [64] Leith, E., and Upatnieks, J., "Reconstructed wavefronts and communication theory", J. Opt. Soc. Amer., Vol. 54, (1962), pp. 1123-1130.
- [65] Vest, C.M., Holographic interferometry, Wiley, New York, 1979.
- [66] Schulman, W., and Dubas, M., Holographic interferometry, Springer-Verlag, Berlin, Germany, 1979.
- [67] Calufield, H.J., Handbook of Optical Holography, Academic Press, New York, 1979.
- [68] Robinson, David W., and Reid, Graeme T., Eds., Interferogram Analysis, Institute of Physics Publishing, Bristol, UK, 1993.
- [69] Hariharan, P., Optical Holography, Cambridge University Press, Cambridge, UK, 1984.
- [70] Marron, Joseph C., and Schroeder, Kirk S., "Holographic laser radar", Optics Letters, Vol. 18, No. 5, (1993), pp. 385-387.
- [71] Zygo Corporation, Product Literature, Middlefield, CT, (1994).
- [72] Wyko Corporation, Product Literature, Tucson, AZ, (1994).
- [73] Marron, Joseph C., and Schroeder, Kirk S., "Three-Dimensional lensless imaging using laser frequency diversity", Applied Optics, Vol. 31, No. 2, (1992), pp. 255-262.
- [74] Takeda, Mitsuo, and Yamamoto, Hirokazu, "Fourier-transform speckle profilometry: three-dimensional shape measurements of diffuse objects with large height steps and / or spatially isolated surfaces", Applied Optics, Vol. 33, No. 34, (1994), pp. 7829-7837.
- [75] Shirley, Lyle L., "Laser Radar Applications and 3D Imaging", Chapter 8 of Tunable Laser Applications, Duarte, F., ed., 1995.
- [76] Gonzalez, Rafael C., and Wintz, Paul, Digital Image Processing, Addison-Wesley Publishing Company, Reading, Massachusetts, 1987.
- [77] Walcyk, Daniel, Ph.D. Thesis, Massachusetts Institute of Technology, (1995).
- [78] Mermelstein, Michael, "A Large-Scale Three-Dimensional Imaging System Based on Laser Speckle", Master of Science Thesis, Massachusetts Institute of Technology, (1995).

Appendix A: Mounting Fixture and Clamping Piece



Not to scale
M'TL: 6061-T6 Al
Finish: Black Anodize
Clamp JHK 2/6/95

Appendix B: New Focus Laser Calibration Data

As discussed in Section 5.5, experiments were done to determine the relationship between the position of the rotary linear actuator which tunes the New Focus external cavity diode laser and the frequency of the laser. This relationship appears to be linear over a large range, but it is actually quadratic. Thus, the most benefit can be gained by looking at the *deviation from linearity* of the position vs. frequency relationship. To do this, I calculated a linear fit to the data and subtracted it from the actual data points. The residuals are plotted below in Figure B.1.

Not only is a quadratic relationship clearly evident, but Figure 6.14 also reveals a main sinusoidal component and other smaller sinusoidal terms. I found the principal sinusoidal component to be due to the periodic slippage between the rotary actuator and the hex hole to which it is coupled. However, even after using a linear actuator to tune the laser frequency, the smaller sinusoidal components would not vanish. These components are most likely due to the fact that the anti-reflective coating used in the laser diode to allow for the external cavity is not perfect. After many trials, I determined that the laser could only be repeatably located to about 3 GHz. This may or may not prevent the laser from being incorporated into a portable laser speckle sensor. Further research on the effect of the consistency of the laser frequency step size on the accuracy of the measurements is needed.

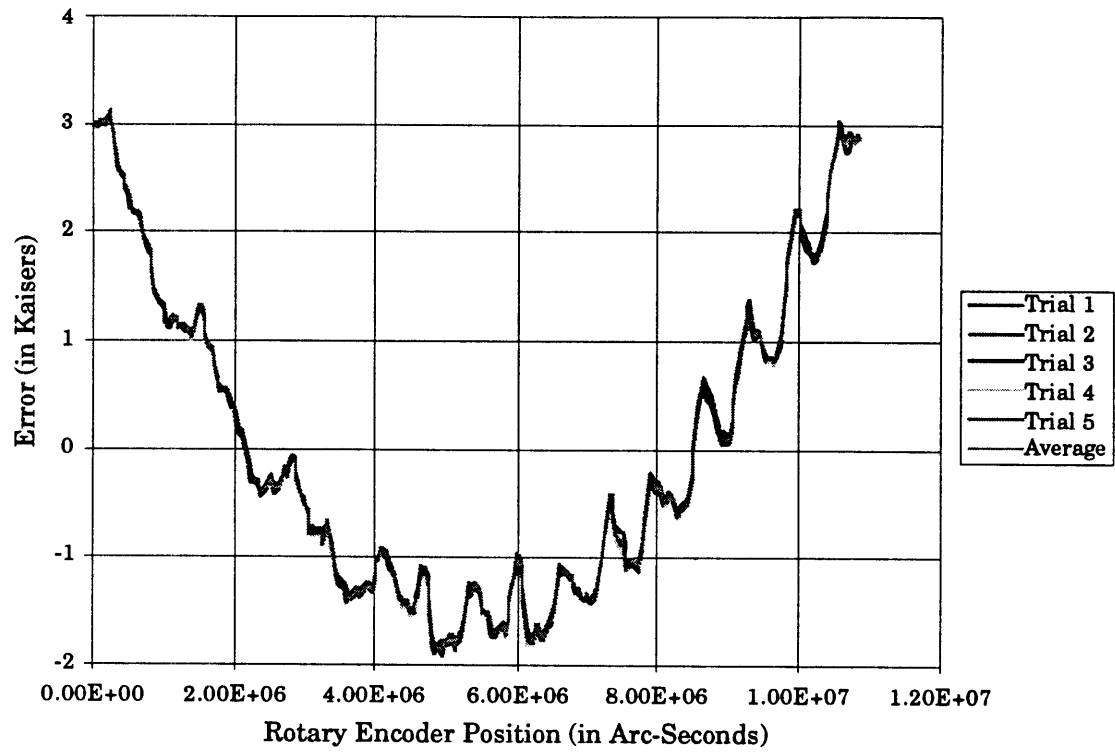


Figure B.1: Deviation of Average Frequency From Linear Fit